AN ADAPTIVE LAGRANGIAN METHOD FOR COMPUTING 1-D REACTING FLOWS

AND

THE THEORY OF RIEMANN INVARIANT MANIFOLDS FOR THE COMPRESSIBLE EULER EQUATIONS

Thesis by
Tasso Lappas

In Partial Fulfillment of the Requirements
for the Degree of
Doctor of Philosophy

California Institute of Technology
Pasadena, California

1993
(Submitted September 16, 1992)

To my parents

Acknowledgements

I would like to thank my advisor Anthony Leonard for his support and understanding during my years as a graduate student. I am especially grateful for the freedom he allowed me in pursuing my research goals and for his patience. I am also grateful to Professor Paul Dimotakis for our many fruitful discussions. His ability to see important points that I had overlooked was indispensable.

I would also like to thank the members of the GALCIT community, especially the members of my research group whose insightful comments and suggestions were very helpful. In particular, the discussions with G.B. Whitham, H.G. Hornung, H.W. Liepmann and A. Roshko are greatly appreciated. Professor J.K. Knowles has also served as an inspiration to me. His mathematical, yet practical, approach to solving physical problems helped me a great deal in my research.

I would like to thank my advisor's secretary Connie Rodriguez as well as all the secretaries and staff in GALCIT, who have been very helpful in so many ways.

This work was sponsored by the Air Force Office of Scientific Research Grants No. 88-0155 and No. 90-0304, whose support is gratefully acknowledged.

Last, but not least, I would like to thank my parents for their support throughout the years, and my grandfather, who has served as an inspiration to me in more ways than one.

Abstract

In the first part of this thesis, a method for computing one-dimensional, unsteady compressible flows, with and without chemical reactions, is presented. This work has focused on accurate computation of the discontinuous waves that arise in such flows. The main feature of the method is the use of an adaptive Lagrangian grid. This allows the computation of discontinuous waves and their interactions with the accuracy of front-tracking algorithms. This is done without the use of additional grid points representing shocks, in contrast to conventional, front-tracking schemes. The Lagrangian character of the present scheme also allows contact discontinuities to be captured easily. The algorithm avoids interpolation across discontinuities in a natural and efficient way. The method has been used on a variety of reacting and non-reacting flows in order to test its ability to compute complicated wave interactions accurately and in a robust way.

In the second part of this thesis, a new approach is presented for computing multidimensional flows of an inviscid gas. The goal is to use the knowledge of the one-dimensional, characteristic problem for gas dynamics to compute genuinely multidimensional flows in a mathematically consistent way. A family of spacetime manifolds is found on which an equivalent 1-D problem holds. These manifolds are referred to as Riemann Invariant Manifolds. Their geometry depends on the local, spatial gradients of the flow, and they provide locally a convenient system of coordinate surfaces for spacetime. In the case of zero entropy gradients, functions analogous to the Riemann invariants of 1-D gas dynamics can be introduced. These generalized Riemann Invariants are constant on the Riemann Invariant Manifolds. The equations of motion are integrable on these manifolds, and the problem of computing the solution becomes that of determining the geometry of these manifolds locally in spacetime.

The geometry of these manifolds is examined, and in particular, their relation to the characteristic surfaces. It turns out that they can be space-like or time-like, depending on the flow gradients. An important parameter is introduced, which plays the role of a Mach number for the wave fronts that these manifolds represent. Finally, the issue of determining the solution at points in spacetime, using information that propagates along space-like surfaces is discussed. The question of whether

it is possible to use information outside the domain of dependence of a point in spacetime to determine the solution is discussed in relation to the existence and uniqueness theorems, which introduce the concept of domain of dependence.

This theory can be viewed as an extension of the method of characteristics to multidimensional, unsteady flows. There are many ways of using the theory to develop practical, numerical schemes. It is shown how it is possible to correct a conventional, second-order Godunov scheme for multidimensional effects, using this theory. A family of second-order, conservative Godunov schemes is derived, using the theory of Riemann Invariant Manifolds, for the case of two-dimensional flow. The extension to three dimensions is straightforward. One of these schemes is used to compute two standard test cases and a two-dimensional, inviscid, shear layer.

Table of Contents

List of Figures

CHAPTER 1
One-Dimensional Reacting and Non-Reacting Flows

Several methods for computing unsteady, inviscid, compressible flows have appeared in the literature in recent years. The emphasis has been on the ability of these numerical schemes to compute developing, discontinuity waves and their interactions accurately.

High-resolution, shock-capturing methods for hyperbolic conservation laws are one category of such methods that have been used successfully in recent years. A basic feature of these methods is that a conservative formulation is used that allows for shocks and their interactions to be captured automatically without special effort. This is characteristic of all older shock-capturing methods such as the Lax-Wendroff scheme (1960), the MacCormack scheme (1969) and the original Godunov scheme (1959). In all such methods, waves of discontinuity of the solution are represented as steep fronts, *i.e.*, smeared over a finite number of computational cells. A second and more important feature of recent, high-resolution schemes is the special effort that is made to achieve higher-order, spatial and temporal accuracy so as to represent discontinuities as accurately as possible, *i.e.*, to reduce the smearing effect that is typical of all shock-capturing methods. Such schemes are the TVD schemes, described by Harten (1983,1984), the various MUSCL-type schemes, such as the one introduced by van Leer (1979) and the PPM scheme (Piecewise Parabolic Method) by Colella and Woodward (1984). A comparative study of some of these schemes for real gases is given in a review article by Montagné, *et al.* (1989). The basic, high-resolution, shock-capturing methods have been developed for nonlinear, scalar, hyperbolic conservation laws. It is for this case that there exists a sound mathematical theory. For nonlinear, hyperbolic systems of equations in one space variable, the theory is not as clear and the numerical methods used for these systems apply the same techniques formally as in the scalar case, but with the additional use of exact or approximate Riemann solvers. A classical Riemann problem is solved locally at each computational cell boundary in order to compute the various flux terms required. This is the essential ingredient of the original Godunov scheme, and

it is present in most successful, high-resolution schemes. The various flux-vector, splitting techniques, described by Steger and Warming (1981) and van Leer (1982), have essentially incorporated in them an approximate Riemann solver. Finally, their extension to more than one space dimension is usually done by treating each spatial dimension separately.

Another category of numerical schemes that have been used is that of the shock-fitting or front-tracking methods. Although they have not been used as extensively as the shock-capturing methods, they have been quite successful in one-dimensional problems. A good review of these methods, as well as of many shock-capturing methods, is given by Moretti (1987). These schemes are typically based on a non-conservative formulation and an effort is made to detect and identify the various discontinuities and to compute their interactions explicitly. This is usually accomplished by introducing additional computational elements representing such waves and using the Rankine-Hugoniot jump conditions. This technique leads to complex programming logic. Identifying the waves and computing their interactions accurately is crucial for obtaining a meaningful and stable solution. For flows with complicated wave interactions, such schemes may not be as robust as the shock-capturing schemes, even in one space dimension.

The research presented in this paper is part of a greater effort which aims to combine the characteristics of the above two categories of numerical schemes and to develop a method that will share the advantages and eliminate most of the disadvantages of both. This has been accomplished in the case of one-dimensional flow by the scheme presented in this paper. The increased accuracy, which is provided in the computation of complicated wave interactions, has made this scheme especially valuable for the computation of reacting gas flows where detonation waves are present.

The scheme is based on a conservative, shock-capturing Godunov-type scheme, very much like van Leer's MUSCL scheme (1979). The new feature, introduced here, is an adaptive Lagrangian grid that increases the accuracy with which discontinuities and their interactions are computed. Without introducing additional computational elements, *i.e.*, refining the grid, or special computational elements to represent these waves, the shocks and contact discontinuities are computed as true discontinuities, without the smearing effect typical of shock-capturing methods. This makes the scheme different from adaptive mesh-refinement schemes (*e.g.*, see Berger and Oliger

1984), which smear discontinuities, although on a much finer local grid. The basic, conservative, shock-capturing capabilities of the scheme are not diminished. The scheme is endowed with the capability of tracking various fronts and, thus, the shock-capturing and the front-tracking ideas are combined properly. It is important to note that the adaptive grid strategy, to a certain degree, is independent of the particular solver. Any Godunov-type scheme may be used. The Riemann solver is the link that provides the information about local wave interactions needed for the adaptive procedure.

It was deemed interesting to try this scheme on 1-D flows of reacting gases in light of the increased accuracy and robustness with which detonation waves and their interactions could be computed. The interest in such flows is evident by the number of papers appearing in the literature. For example, numerical calculations, with increased accuracy, of the one-dimensional instability of plane-detonation waves may be of great interest in confirming existing theories that are based on linear-stability analysis (*e.g.*, see Lee and Stewart, 1990). The present scheme is able to reduce the error caused by the numerical smearing of the leading shock of the detonation wave. This error may be very important in the development of detonation instability.

The computer code developed is also able to compute one-dimensional, cylindrically and spherically symmetric flows, as well as plane flows with area change. It is thus possible to compute explosions and implosions and to study the effect of curvature on detonation wave speed and stability. Most of the results presented are basically validation runs and calculations demonstrating the abilities of the method and the potential use for specific 1-D problems of interest. All results shown are for a perfect gas. The difficulty of incorporating a general equation of state is the same as in most schemes and independent of the main feature of the present scheme, *i.e.*, the adaptive Lagrangian-grid strategy.

1.1 Numerical Method

1.1.1 Mathematical formulation

The inviscid flow of a reacting mixture of calorically perfect gases is considered. The assumption of a simplified reacting mixture is made, according to which there are two species present at any time, the reactant and the product. The reactant is converted to the product by a one-step, irreversible, exothermic chemical reaction. This assumption is made in order to compare with the many theoretical and numerical results that are available in the literature for this case. The chemical-reaction rate is given by the standard Arrhenius law

$$\dot{z} \;=\; -Kz\,T^{\alpha}\exp\left(-E/R_gT\right)\;, \tag{1.1a}$$

where z is the mass fraction of unburnt gas, K is a positive constant, which essentially gives a time scale, E is the activation energy of the chemical reaction, R_g is the gas constant, T is the absolute temperature and α is also a constant. The simplified Arrhenius model, where the reaction rate is a step function depending on the temperature, has also been used. For the simplified model the rate is given by

$$\dot{z} \;=\; -KzH\left(T-T_c\right)\;, \tag{1.1b}$$

where

$$H(x)=\begin{cases}1, & x\;>\;0\;,\\ 0, & x\;\leq\;0\;,\end{cases} \tag{1.2}$$

and T_c is a given critical temperature.

The problem under consideration is a special case of the general problem of solving numerically the nonlinear hyperbolic system of the form

$$\frac{\partial U}{\partial t}+\frac{\partial F(U)}{\partial x}=G(U)\;, \tag{1.3}$$

where U is the appropriate solution vector. As usual, x denotes the Eulerian space variable. If the Lagrangian formulation is used, a system of exactly the same form is obtained. The space variable x, then, is replaced by a Lagrangian space variable and the flux vector $F(U)$ is changed appropriately. For non-reacting flow, $G(U)=0$. Most numerical methods use Eq. (1.3) as their starting point, and using a finite volume discretization, obtain the scheme of the following general form

$$U_j^{n+1} \;=\; U_j^n-\frac{\Delta t}{\Delta x}\left(\hat{F}_{j+1/2}-\hat{F}_{j-1/2}\right)+\Delta t\,\hat{G}_j\;, \tag{1.4}$$

giving the solution, in an average sense, in the j^{th} cell at the time level $n+1$. The numerical flux terms $\hat{F}$ are computed at the boundaries of each cell. An important feature of every numerical method is the calculation of these flux terms in a way that guarantees stability and high-order accuracy.

A slightly different approach will be taken in deriving the present scheme. Eventually, it will be of the general form given in Eq. (1.4). It is useful to formulate the problem by writing the conservation laws in integral form for an arbitrary control volume $V(t)$, whose bounding surface $S(t)$ moves with a velocity $\mathbf{u}_\mathrm{b}$ (Reynolds' Transport Theorem). These equations will be applied to each computational volume of the discrete numerical scheme. This is done so that the conservation equations and their discrete counterparts are written in a way that is independent of the Eulerian or Lagrangian formulation that will be adopted eventually. Moreover, it is easier to see from these equations how the idea for the adaptive nature of the grid is motivated. The conservation equations in integral form are

$$\frac{d}{dt}\int_{V(t)} \rho \, dV + \int_{S(t)} \rho \, (\mathbf{u}-\mathbf{u}_\mathrm{b})\cdot d\mathbf{S} \;=\; 0 \,, \tag{1.5}$$

$$\frac{d}{dt}\int_{V(t)} \rho\mathbf{u} \, dV + \int_{S(t)} \rho\mathbf{u} \, (\mathbf{u}-\mathbf{u}_\mathrm{b})\cdot d\mathbf{S} + \int_{S(t)} p \, d\mathbf{S} \;=\; 0 \,, \tag{1.6}$$

$$\frac{d}{dt}\int_{V(t)} \rho e_\mathrm{t} \, dV + \int_{S(t)} \rho e_\mathrm{t} \, (\mathbf{u}-\mathbf{u}_\mathrm{b})\cdot d\mathbf{S} + \int_{S(t)} p\mathbf{u}\cdot d\mathbf{S} \;=\; 0 \,, \tag{1.7}$$

$$\frac{d}{dt}\int_{V(t)} \rho z \, dV + \int_{S(t)} \rho z \, (\mathbf{u}-\mathbf{u}_\mathrm{b})\cdot d\mathbf{S} - \int_{V(t)} \dot{z} \, \rho \, dV \;=\; 0 \,. \tag{1.8}$$

These are written for an arbitrary control volume $V(t)$, whose bounding surface $S(t)$ has a velocity $\mathbf{u}_\mathrm{b}$. In the above equations, e_t is the total specific energy, which includes the chemical energy; *i.e.*,

$$e_\mathrm{t} = e + \frac{1}{2}u^2 + q_0 z \,, \tag{1.9}$$

where e is the specific internal energy, q_0 is the heat release of the chemical reaction, and $u = |\mathbf{u}|$ is the magnitude of the fluid velocity. The perfect gas assumption is also made; *i.e.*,

$$p = (\gamma - 1)\,\rho e \,. \tag{1.10}$$

Since the boundaries of the computational cells will be moving, it is useful to consider the flow map

$$\mathbf{x} = \mathbf{X}\,(\boldsymbol{\xi}, t) \;, \tag{1.11}$$

which gives the position of the fluid particle that was initially ($t = 0$) at the position $\boldsymbol{\xi}$. Thus, $\boldsymbol{\xi}$ is a convenient Lagrangian marker for the fluid particles in the flow. If the Lagrangian approach is taken, the local boundary velocity is equal to the local fluid velocity; *i.e.*, $\mathbf{u}_b = \mathbf{u}$ in Eqs. (1.5)–(1.8).

1.1.2 Spatial and temporal discretization

Consider now the case of one-dimensional flow. A finite volume formulation is used; *i.e.*, space is discretized by a set of computational cells as shown in Fig. 1.1. The conservation equations are now written for the j^{th} cell of the computational grid

$$\frac{dm_j}{dt} + (\rho \Delta u_b)_{j+1/2} - (\rho \Delta u_b)_{j-1/2} = 0 , \tag{1.12}$$

$$\frac{d}{dt}(m_j u_j) + (\rho u \Delta u_b)_{j+1/2} - (\rho u \Delta u_b)_{j-1/2} + p_{j+1/2} - p_{j-1/2} = 0 , \tag{1.13}$$

$$\frac{d}{dt}(m_j e_{tj}) + (\rho e_t \Delta u_b)_{j+1/2} - (\rho e_t \Delta u_b)_{j-1/2} + (up)_{j+1/2} - (up)_{j-1/2} = 0 , \tag{1.14}$$

$$\frac{d}{dt}(m_j z_j) + (\rho z \Delta u_b)_{j+1/2} - (\rho z \Delta u_b)_{j-1/2} - \dot{z}_j m_j = 0 , \tag{1.15}$$

where

$$\begin{aligned} \Delta u_b &\equiv u - u_b , \\ m_j &\equiv \int_{x_{j-1/2}}^{x_{j+1/2}} \rho dx , \\ m_j u_j &\equiv \int_{x_{j-1/2}}^{x_{j+1/2}} \rho u dx , \\ m_j e_{tj} &\equiv \int_{x_{j-1/2}}^{x_{j+1/2}} \rho \left(e + \frac{1}{2}u^2 + q_0 z \right) dx , \\ m_j z_j &\equiv \int_{x_{j-1/2}}^{x_{j+1/2}} \rho z dx . \end{aligned} \tag{1.16}$$

Average values of all quantities in the j^{th} cell are denoted by the subscript j, and values of various quantities at the two boundaries of the cell are denoted by the subscripts $j \pm 1/2$. Note that average values are mass-averaged values. By defining

$$\begin{aligned} F_m &\equiv \rho \Delta u_b , \\ F_u &\equiv \rho u \Delta u_b + p , \\ F_e &\equiv \rho e_t \Delta u_b + p u , \\ F_z &\equiv \rho z \Delta u_b , \end{aligned} \tag{1.17}$$

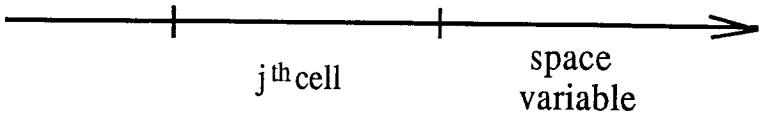

FIG.1.1 Finite-volume discretization in one space dimension. The space variable can be the Eulerian x or the Lagrangian ξ. The boundaries of the j^{th} cell are denoted by the subscripts $j \pm 1/2$.

the equations of motion can be written in the more familiar form

$$\begin{aligned}
\frac{dm_j}{dt} + (F_m)_{j+1/2} - (F_m)_{j-1/2} &= 0 \,, \\
\frac{d}{dt}(m_j u_j) + (F_u)_{j+1/2} - (F_u)_{j-1/2} &= 0 \,, \\
\frac{d}{dt}(m_j e_{tj}) + (F_e)_{j+1/2} - (F_e)_{j-1/2} &= 0 \,, \\
\frac{d}{dt}(m_j z_j) + (F_z)_{j+1/2} - (F_z)_{j-1/2} &= m_j \dot{z}_j \,.
\end{aligned} \tag{1.18}$$

Note the extra degree of freedom provided in the flux terms by the as yet unspecified term Δu_b. The motion of the cell boundaries is determined by

$$\frac{dx_{j\pm1/2}}{dt} = (u_b)_{j\pm1/2} \,, \tag{1.19}$$

and the average density in each cell is given by

$$\rho_j = \frac{m_j}{x_{j+1/2} - x_{j-1/2}} \,. \tag{1.20}$$

The equation of state (1.10) provides the means for computing the average pressure in the j^{th} cell,

$$p_j = (\gamma_j - 1)\,\rho_j \left(e_{tj} - q_0 z_j - \frac{1}{2} u_j^2 \right) \,. \tag{1.21}$$

The exact integral conservation laws have been written for each computational cell. Eqs. (1.18) will now be integrated explicitly in time. The basis for the method is a conservative, Godunov-type scheme similar to the MUSCL scheme introduced by van Leer (1979). The procedure followed in solving these equations is similar to that used in most methods, which are higher-order extensions of the original

Godunov scheme. At every time instant, average values of the solution are known in each computational cell. Linear variations of the primitive variables, *i.e.*, density ρ, pressure p and velocity u, are assumed in each cell. A Riemann problem is then set up locally at each cell interface. The solution to this problem gives the velocity, pressure and density needed to compute the flux terms (1.17). The different feature in the present scheme is that the Lagrangian formulation is used instead of the Eulerian and that an adaptive grid is used.

So far, the fact that the Lagrangian formulation is being used has not appeared explicitly in the description of the method. It is now that this choice is made and all quantities are considered as functions of time t and the Lagrangian space coordinate ξ. The interpolation procedure is carried out in ξ-space, and assuming linear variation, the generic quantity q varies as

$$q(\xi) \;=\; q_j + (q_\xi)_j \;(\xi - \xi_j) \;, \tag{1.22}$$

in the j^{th} cell, where q_j is the mass-averaged value in the cell, ξ_j is the center of the cell (in Lagrangian space), and $(q_\xi)_j$ is the slope of q in this cell, which is assumed to be constant. Note that discontinuities of these quantities are allowed at the cell interfaces, as shown in Fig. 1.2.

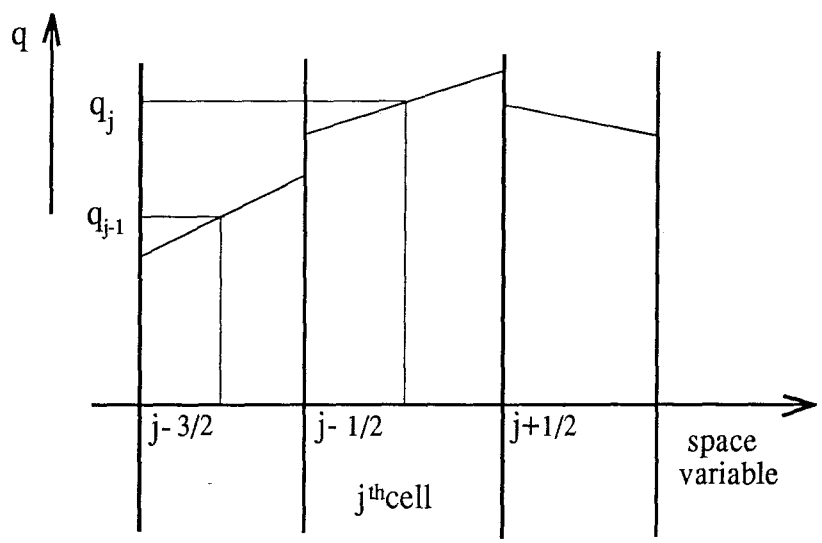

FIG.1.2 Linear variation of the generic quantity q in the j^{th} cell. In general, q is discontinuous at the cell interfaces.

The slopes are chosen using the slope limiter given by van Leer (1984), but the adaptive nature of the grid, which will be described next, makes the choice of limiter less important than in the typical higher-order, Godunov-type schemes. In fact, the adaptive grid allows more freedom in choosing the interpolation scheme, because additional information on the location of the various waves is always available at each time instant. The slope $(q_\xi)_j$ is computed, following van Leer (1984), by

$$(q_\xi)_j \;=\; \text{ave}\left(q_\xi^- \;,\; q_\xi^+\right) \;, \tag{1.23}$$

where

$$q_\xi^- \;=\; \frac{q_j - q_{j-1}}{\xi_j - \xi_{j-1}} \quad , \quad q_\xi^+ \;=\; \frac{q_{j+1} - q_j}{\xi_{j+1} - \xi_j} \;, \tag{1.24}$$

$$\text{ave}\,(x,y) \;\equiv\; \frac{x+y}{2}\left[1 - \frac{(x-y)^2}{x^2+y^2+c^2}\right] \;, \tag{1.25}$$

and c^2 is a small constant ($c^2 \ll 1$).

At each cell interface, two constant states q^- and q^+ are required to be used as the initial condition for the Riemann problem. There are many ways of doing this. One way is to specify for the $j+1/2$ interface

$$\begin{aligned} q^-_{j+1/2} \;&=\; q_j + (q_\xi)_j\left(\xi_{j+1/2} - \xi_j\right) \;, \\ q^+_{j+1/2} \;&=\; q_{j+1} + (q_\xi)_{j+1}\left(\xi_{j+1/2} - \xi_{j+1}\right) \;, \end{aligned} \tag{1.26}$$

i.e., the values of q on either side of the interface, as given by Eq. (1.22). Using these states does not ensure second-order accuracy in time. The method used in the present scheme is shown in Fig. 1.3. The domain of dependence of $\xi \;=\; \xi_{j+1/2}$ over the time interval Δt is estimated by the characteristics at the time level t. In the Lagrangian formulation of the problem the characteristic speeds are given by

$$c_\pm \;=\; \pm\frac{\rho}{\rho_0}a \;, \tag{1.27}$$

where ρ_0 is the initial density ($t \;=\; 0$) and a is the speed of sound. The constant states $q^\pm$ are then determined as the averages of Eq. (1.22) over the domains $\Delta\xi^\pm$. See Fig. 1.3. These domains correspond to the full timestep Δt. This is equivalent to tracing the characteristics back from the time $t+\Delta t/2$ and using the linear profile (1.22). This ensures second-order accuracy in time.

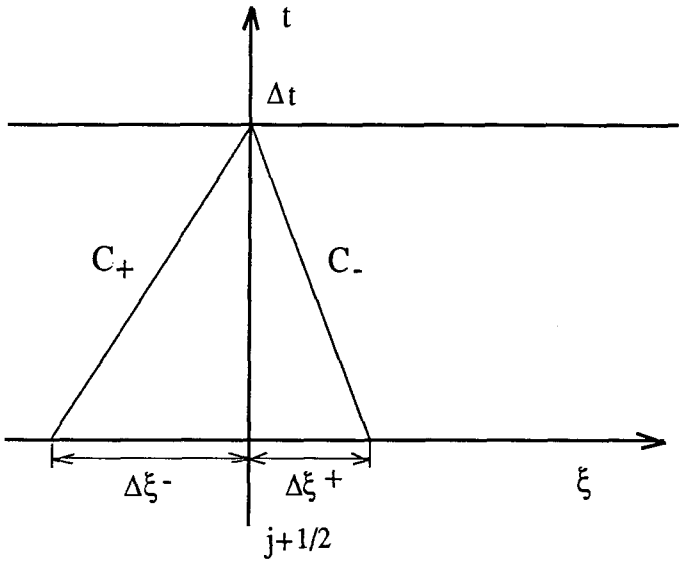

FIG.1.3 The constant states $q^{\pm}$, which are to be used as the initial condition for the Riemann problem at the interface $j+1/2$, are obtained by averaging the linear interpolant over the domains of dependence $\Delta\xi^{\pm}$. These domains correspond to the full timestep Δt.

The discrete scheme, giving the solution at the time level $n+1$ from the solution at the previous time level n, can now be written as

$$
\begin{aligned}
(m_j)^{n+1} &= (m_j)^n - \Delta t \left[\left(\hat{F}_m\right)_{j+1/2} - \left(\hat{F}_m\right)_{j-1/2} \right] , \\
(m_j u_j)^{n+1} &= (m_j u_j)^n - \Delta t \left[\left(\hat{F}_u\right)_{j+1/2} - \left(\hat{F}_u\right)_{j-1/2} \right] , \\
(m_j e_{tj})^{n+1} &= (m_j e_{tj})^n - \Delta t \left[\left(\hat{F}_e\right)_{j+1/2} - \left(\hat{F}_e\right)_{j-1/2} \right] , \\
(m_j z_j)^{n+1} &= (m_j z_j)^n - \Delta t \left[\left(\hat{F}_z\right)_{j+1/2} - \left(\hat{F}_z\right)_{j-1/2} \right] + \Delta t \, (m_j \dot{z}_j)^n , \\
x^{n+1}_{j\pm 1/2} &= x^n_{j\pm 1/2} + \Delta t \, (u_b)_{j\pm 1/2} ,
\end{aligned}
\tag{1.28}
$$

where the numerical fluxes $\hat{F}_m$, $\hat{F}_u$, $\hat{F}_e$ and $\hat{F}_z$ are given by Eqs. (1.17), using the solution of the Riemann problem. The average boundary velocity u_b for each interface is still unspecified, but for the majority of interfaces $u_b = u$, and the last of Eqs. (1.28) is second-order accurate in time. The source term in the species equation is shown in Eqs. (1.28) as being evaluated at time level n. It is better to integrate the source term in a "split" manner, *i.e.*, integrate the first four equations in (1.28) without the source term and use this intermediate state to estimate the

term $m_j \dot{z}_j$. This splitting has been implemented in the present scheme.

The stability requirement on the timestep is that of a MUSCL scheme in the Lagrangian formulation. No additional stability problems arise because of the adaptive grid strategy presented in the next section.

1.1.3 Adaptive Grid

The motivation for the adaptive grid comes from the definition of the flux terms, as given by Eqs. (1.17). The term Δu_b, or equivalently, the velocity of the cell boundary u_b, is unspecified. The idea is to specify it at each cell interface, so that all important discontinuity waves coincide with cell boundaries, at every discrete time level. The solution of the Riemann problem at a given interface provides all the information needed to identify all the important waves emanating from this interface, as well as their strengths and speeds. This information is enough to specify Δu_b. Since all important waves coincide with cell boundaries, it is guaranteed that at subsequent time instants, the evolution of these waves will be determined properly by the solution of the local Riemann problems. In the numerical experiments carried out, shock-waves computed by the local Riemann solvers were considered important enough to track if the shock Mach number was greater than 1.01, and contact discontinuities were considered important if the ratio of the densities on either side was greater than 1.05. These parameters are quite conservative. One may want to track only the very strong shock-waves in the flow.

The grid is, basically, Lagrangian; *i.e.*, most cell boundaries move with the local fluid velocity, and hence $\Delta u_b = 0$. It is easy to see that the same ideas on the adaptivity of the grid can be used on a grid that is primarily Eulerian. The same equations can be applied directly.

An example of this adaptive procedure is shown in Fig. 1.4. A strong shock-wave moving to the right is computed by the Riemann solver at the interface $i-1/2$ at time t. The decision is made to assign a velocity to the adjacent cell boundary $i+1/2$, so that at time $t+\Delta t$ the shock coincides with the interface $i+1/2$. Another possibility would be to have the interface $i-1/2$ move with the shock. The decision is made depending on which interface would be required to move a shorter distance in Lagrangian space. The shock speeds are assumed constant over the time interval

Δt. It is obvious that the local expansion waves can be tracked in the same way. This was not implemented in the present scheme, simply to reduce the complexity of the programming.

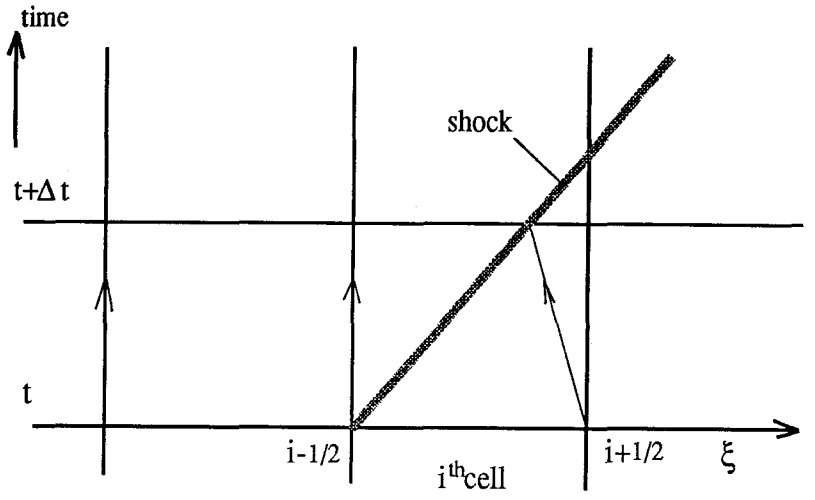

FIG.1.4 The appropriate velocity is assigned to the cell interface $i+1/2$ in order to intercept the shock at the subsequent, discrete time level.

It is evident from this example that a relation between the velocities in real space and the velocities in Lagrangian space is needed to update the Lagrangian grid. Consider the motion of a cell boundary given by the trajectory $x = x_b(t)$. This boundary is moving with a velocity $u_b = \dot{x}_b(t)$, which, in general, is different from that of the fluid u. This motion corresponds to a motion in ξ-space given by the trajectory $\xi = \xi_b(t)$ with velocity $v_b = \dot{\xi}_b(t)$. The relation between the two velocities is found with the use of the flow map

$$x = X(\xi, t)\,, \tag{1.29}$$

which is essentially Eq. (1.11), written here for one-dimensional flow. The cell boundary motion is given by

$$x_b(t) = X\left(\xi_b(t), t\right)\,, \tag{1.30}$$

and hence,

$$u_b = \left(\frac{\partial X}{\partial t}\right)_\xi + \dot{\xi}_b(t)\left(\frac{\partial X}{\partial \xi}\right)_t\,, \tag{1.31a}$$

or

$$u_b = u + v_b \left(\frac{\partial X}{\partial \xi}\right)_t . \tag{1.31b}$$

The derivative of the flow map is numerically approximated and assumed constant in each cell; *i.e.*,

$$\left(\frac{\partial X}{\partial \xi}\right)_j \simeq \frac{x_{j+1/2} - x_{j-1/2}}{\xi_{j+1/2} - \xi_{j-1/2}} . \tag{1.32}$$

The velocities of the various waves, which are computed by the Riemann problems, can be translated into velocities in ξ-space by using Eq. (1.31b). The Lagrangian position of each interface is updated by

$$\xi^{n+1}_{j\pm 1/2} = \xi^n_{j\pm 1/2} + \Delta t\,(v_b)_{j\pm 1/2} . \tag{1.33}$$

The solution to the Riemann problem at each interface provides sufficient information for the adaptive strategy. Using the exact Riemann solver at every interface is very costly. To reduce the cost, various criteria were found to identify the cell interfaces where a strong discontinuity is suspected to be present, before solving the Riemann problem. These interfaces are flagged as critical interfaces. The ratio $\Delta\xi^-/\Delta\xi^+$ has proven useful in detecting developing shocks in the flow. Where the flow is smooth, without steep gradients, the above ratio is

$$\frac{\Delta\xi^-}{\Delta\xi^+} \simeq 1 . \tag{1.34}$$

The regions, where this ratio deviates from unity by more than 10%, are considered critical regions. The full, nonlinear Riemann solver is used only in these regions. Everywhere else the simple acoustic approximation to the Riemann problem solution is used. It was found in all the numerical experiments performed that in addition to the above criterion, finding local extrema of the slopes in pressure, density and velocity was very useful in determining these regions. Other criteria may also be used. It is important that the criteria be conservative enough, so that no critical regions are missed, but they are not crucial in detecting discontinuities. The detection of important discontinuities is ultimately done by examining the solutions to the local Riemann problems.

No more than two adjacent critical interfaces are allowed at any given time. In the smooth compression regions, the interfaces at the maxima of the pressure gradients are considered critical. The pressure gradients are estimated, using simple, finite differences. If the Riemann solver at these locations computes sufficiently strong discontinuities, then they are tracked. The critical interfaces, which carry these waves, are treated the same way at the next time level, along with other possible critical interfaces that may be detected. When there are two adjacent critical interfaces, the two Riemann problems are solved simultaneously. At this point it is decided if collisions will occur within the timestep Δt. There are six waves resulting from the two Riemann problems, and there are four cell interfaces available to do the tracking. The strongest waves are tracked and the others are ignored. This procedure has proven to be very robust in handling all possible wave interactions.

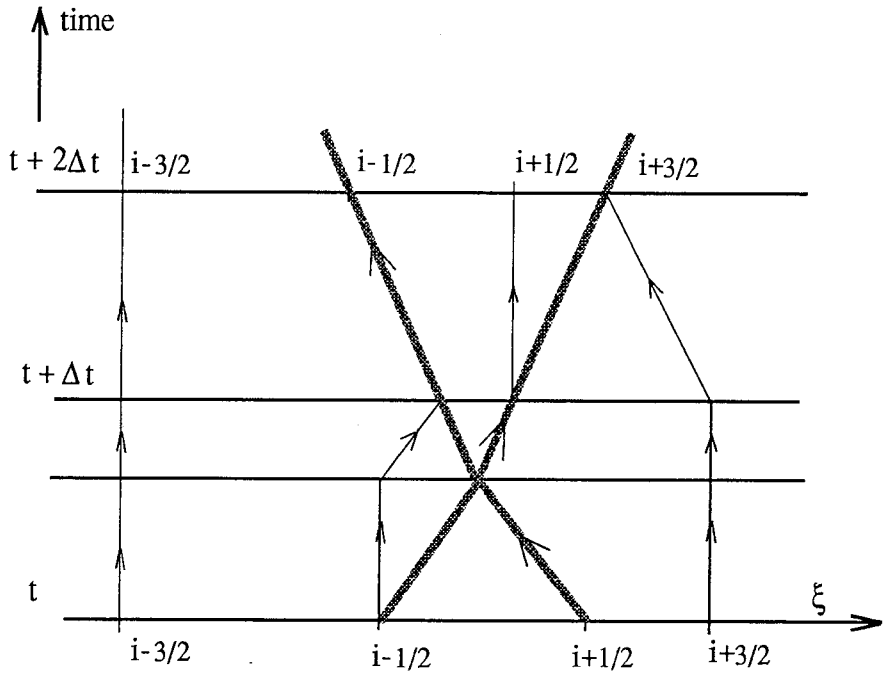

FIG.1.5 The typical collision of two shocks is shown. The timestep is adjusted locally so that the collision point coincides with the cell interface $i + 1/2$ at the intermediate timestep.

Collisions and reflections from walls can be treated in a straightforward way using this adaptive grid. A typical collision case is shown in Fig. 1.5. At time t, two strong shock-waves at the interfaces $i-1/2$ and $i+1/2$, are moving at each other with speeds that allow for a collision before time $t+\Delta t$. The Riemann problems at the interfaces $i-1/2$ and $i+1/2$ are solved at time t, simultaneously. The solution indicates that there will be a collision within the time interval Δt. The timestep is adjusted locally, *i.e.*, only for the three cells $i-1$, i and $i+1$, so that at the intermediate time instant, the collision point coincides with the cell boundary $i+1/2$. The Riemann solver at this interface, at the intermediate time instant, will compute the two shock-waves emerging from the collision, and the adjacent cell boundaries will be able to track them in the same way at subsequent times. The fluxes at the interfaces $i-3/2$ and $i+3/2$ are held constant for the whole timestep Δt. This leads to a robust way of handling wave interactions, without loss of accuracy.

1.2 Riemann Solver

The Riemann solver is an important ingredient of the numerical scheme. It provides the means for computing the velocity and the pressure at the cell interfaces and thus, the various flux terms required. It also gives valuable information about the local waves emanating from each cell interface. As explained in the previous section, the Lagrangian grid adapts in such a way that important discontinuities and collision points coincide with cell boundaries at each time instant. It is, therefore, necessary to be able to identify the waves emanating from these critical cell boundaries at subsequent times. This is what the Riemann solver accomplishes. A variety of exact and approximate Riemann solvers have appeared in the literature in recent years. In all these solvers the focus is on computing the velocity and pressure of the contact discontinuity, which appears after the breakup of the initial discontinuity of the Riemann problem. In the present scheme it is crucial to identify the exact wave pattern as well. This information is used to assign the appropriate velocities to adjacent cell boundaries so that all important waves are tracked, and to adjust the timestep locally so that collisions are computed accurately. Moreover, the fluxes at an interface need to be computed along the ray $\dot{\xi}(t) = v_b$. See Eq. (1.31b). Most interfaces are Lagrangian and hence, $v_b = 0$.

1.2.1 Non-reacting, perfect gas

Consider the case of the Riemann problem for inviscid flow of a perfect gas without chemical reactions. The initial condition at time $t = 0$ consists of two constant states denoted by the subscripts r and l. Note that it is possible to have two different perfect gases on either side of the $\xi = 0$ location, as indicated by the different specific heat ratios, *i.e.*, γ_r and γ_l. See Fig. 1.6. The space variable ξ is the Lagrangian space coordinate. At time $t = 0^+$ the general wave pattern shown in Fig. 1.7 will develop.

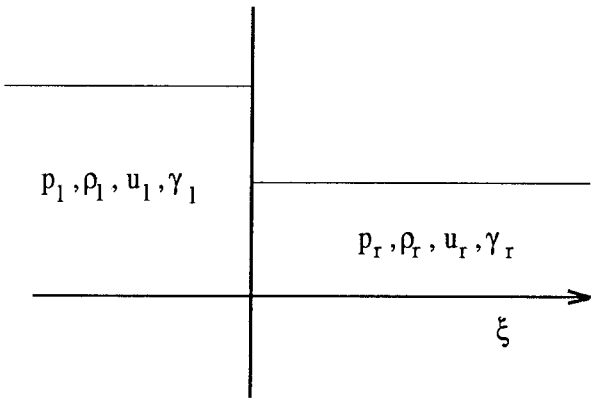

FIG.1.6 Initial condition for the Riemann problem. The variable ξ is the Lagrangian space coordinate.

There is a wave moving to the right (positive ξ) denoted by R, a wave moving to the left(negative ξ) denoted by L and a contact discontinuity C, which remains at $\xi = 0$ for all time, *i.e.*, moves with the local fluid velocity. The waves R and L are either shocks or expansion waves, depending on the initial condition. Across the contact discontinuity C, the pressure p_f and velocity u_f are continuous, but the density has a jump discontinuity at $\xi = 0$ for all time. The density is ρ_{fl} for $\xi < 0$ and ρ_{fr} for $\xi > 0$. It is known that the solution to this initial value problem exists and is unique for arbitrary initial conditions. Moreover, the solution is self-similar, and the shock-waves propagate with a constant velocity and strength. That is why they are represented by straight lines in the (ξ, t) diagram.

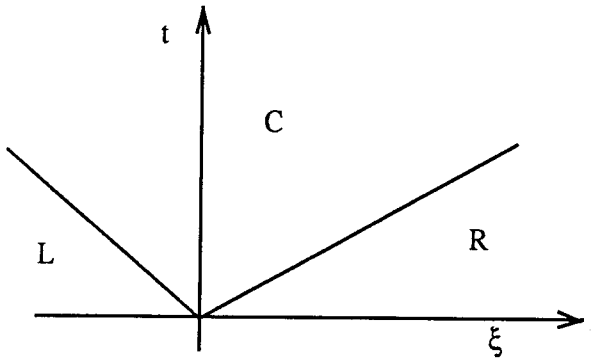

FIG.1.7 General wave pattern resulting from the breakup of the original discontinuity of the Riemann problem. C is a contact discontinuity. L and R can be either shocks or expansion waves.

There are four wave patterns possible for this problem. The solution will be found for each of these wave patterns for the special case of a perfect gas.

(i) L-shock, R-shock

Across the shock R the following relationship holds:

$$r \equiv \frac{u_f - u_r}{a_r} = \frac{2}{\gamma_r + 1}\left(M_r - \frac{1}{M_r}\right) . \tag{1.35}$$

M_r is the shock Mach number defined by

$$M_r \equiv \frac{U_r - u_r}{a_r} , \tag{1.36}$$

where U_r is the shock velocity and $a_r = \sqrt{\gamma_r p_r/\rho_r}$ is the speed of sound in the undisturbed region r. Similarly, for the shock L,

$$\frac{u_l - u_f}{a_l} = \frac{2}{\gamma_l + 1}\left(M_l - \frac{1}{M_l}\right) , \tag{1.37}$$

where M_l is the shock Mach number for L. Equations (1.35) and (1.37) can be solved for the shock Mach numbers to give

$$M_r = \frac{\gamma_r + 1}{4} r + \sqrt{\left(\frac{\gamma_r + 1}{4}\right)^2 r^2 + 1} , \tag{1.38}$$

$$M_l = \frac{\gamma_l+1}{4}\frac{u_l-u_f}{a_l} + \sqrt{\left(\frac{\gamma_l+1}{4}\right)^2\left(\frac{u_l-u_f}{a_l}\right)^2+1}\,. \tag{1.39}$$

The pressure ratios across the two shocks are given by the following equations:

$$\frac{p_f}{p_r} = 1+\frac{2\gamma_r}{\gamma_r+1}\left(M_r^2-1\right)\,, \tag{1.40}$$

$$\frac{p_f}{p_l} = 1+\frac{2\gamma_l}{\gamma_l+1}\left(M_l^2-1\right)\,. \tag{1.41}$$

From Eqs. (1.38)–(1.41) one obtains a single equation for the unknown r,

$$\begin{aligned} G(r) \equiv\ & 1-\frac{p_l}{p_r}+\gamma_r\frac{\gamma_r+1}{4}r^2+\gamma_r r\sqrt{\left(\frac{\gamma_r+1}{4}\right)^2 r^2+1} \\ & -\frac{p_l}{p_r}\gamma_l\frac{\gamma_l+1}{4}\left(\frac{u_l-u_r}{a_l}-\frac{a_r}{a_l}r\right)^2 \\ & -\frac{p_l}{p_r}\gamma_l\left(\frac{u_l-u_r}{a_l}-\frac{a_r}{a_l}r\right)\sqrt{\left(\frac{\gamma_l+1}{4}\right)^2\left(\frac{u_l-u_r}{a_l}-\frac{a_r}{a_l}r\right)^2+1} \;=\; 0\,. \end{aligned} \tag{1.42}$$

This equation is solved numerically using a Newton-Raphson method. Once r is obtained, all other quantities of interest follow from Eqs. (1.35)–(1.41). The densities are determined by

$$\frac{\rho_{fi}}{\rho_i} = \frac{(\gamma_i+1)\,M_i^2}{2+(\gamma_i-1)\,M_i^2}\,, \qquad i = r,l\,. \tag{1.43}$$

It is important to be able to determine whether this wave pattern will develop for a given initial condition. For this solution to be possible, certain compatibility conditions must hold. These are easily found by noticing that in Eqs. (1.35) and (1.37), the shock Mach numbers M_r and M_l must be greater than 1. It then follows that the following compatibility condition must hold:

$$u_r \le u_f \le u_l\,, \tag{1.44}$$

or equivalently,

$$\begin{aligned} & u_r-u_l \le 0\,, \\ & 0 \le r \le \frac{u_l-u_r}{a_r}\,. \end{aligned} \tag{1.45}$$

(ii) L-expansion wave, R-shock

In this case, Eqs. (1.35),(1.36),(1.38) and (1.40), derived previously, still hold for the shock-wave R. In addition to these equations, the following equation gives the pressure ratio across the isentropic expansion wave,

$$\begin{aligned} \frac{p_f}{p_l} &= \left(1+\frac{\gamma_l-1}{2}\frac{u_l-u_f}{a_l}\right)^{2\gamma_l/(\gamma_l-1)} \\ &= \left(1+\frac{\gamma_l-1}{2}\frac{u_l-u_r}{a_l}-\frac{\gamma_l-1}{2}\frac{a_r}{a_l}r\right)^{2\gamma_l/(\gamma_l-1)} , \end{aligned} \tag{1.46}$$

where r is defined in Eq.(1.35). Combining Eqs. (1.38),(1.40) and (1.46), a single equation in r is obtained, as in the previous case,

$$\begin{aligned} F(r) \equiv\ & 1+\gamma_r\frac{\gamma_r+1}{4}r^2+\gamma_r r\sqrt{\left(\frac{\gamma_r+1}{4}\right)^2 r^2+1} \\ & -\frac{p_l}{p_r}\left(1+\frac{\gamma_l-1}{2}\frac{u_l-u_r}{a_l}-\frac{\gamma_l-1}{2}\frac{a_r}{a_l}r\right)^{2\gamma_l/(\gamma_l-1)} = 0 , \end{aligned} \tag{1.47}$$

which is solved numerically. The densities are determined by Eq. (1.43) across the shock and by the isentropic relation

$$\frac{\rho_{fl}}{\rho_l} = \left(\frac{p_{fl}}{p_l}\right)^{1/\gamma} ,$$

across the expansion wave.

The compatibility conditions are found by noticing that across the expansion wave L, $\quad 0 \le p_f/p_l \le 1$, and across the shock R, $\quad p_f/p_r \ge 1$. Using Eqs. (1.40) and (1.46), the following relations are found, after some algebra,

$$\begin{aligned} p_r/p_l &\le 1 , \\ u_r-u_l &< \left(\frac{2}{\gamma_l-1}\right)a_l , \end{aligned} \tag{1.48}$$

and

$$\begin{aligned} \frac{u_l-u_r}{a_r} \le r &< \frac{u_l-u_r}{a_r}+\left(\frac{2}{\gamma_l-1}\right)\frac{a_l}{a_r} \\ 0 &\le r . \end{aligned} \tag{1.49}$$

(iii) L-shock, R-expansion wave

This case is exactly the same as case (ii) with the transformation $\xi \to -\xi$.

(iv) L-expansion wave, R-expansion wave

In this case, there are two expansion waves, and the pressure ratios across them are given by

$$\begin{aligned} \frac{p_f}{p_l} &= \left(1+\frac{\gamma_l-1}{2}\frac{u_l-u_f}{a_l}\right)^{2\gamma_l/(\gamma_l-1)} , \\ \frac{p_f}{p_r} &= \left(1+\frac{\gamma_r-1}{2}\frac{u_f-u_r}{a_r}\right)^{2\gamma_r/(\gamma_r-1)} . \end{aligned} \tag{1.50}$$

From Eqs. (1.50) the following single equation in r is obtained:

$$\begin{aligned} S(r) \equiv & \left(1+\frac{\gamma_r-1}{2}r\right)^{2\gamma_r/(\gamma_r-1)} \\ & -\frac{p_l}{p_r}\left(1+\frac{\gamma_l-1}{2}\frac{u_l-u_r}{a_l}-\frac{\gamma_l-1}{2}\frac{a_r}{a_l}r\right)^{2\gamma_l/(\gamma_l-1)} = 0 , \end{aligned} \tag{1.51}$$

which is solved numerically with the Newton-Raphson method. The compatibility conditions are once again found by noticing that across the expansion waves $0 \le p_f/p_l \le 1$ and $0 \le p_f/p_r \le 1$, which, using Eqs. (1.50), give

$$0 \le u_r - u_l < 2\left(\frac{a_r}{\gamma_r-1}+\frac{a_l}{\gamma_l-1}\right) , \tag{1.52}$$

and

$$\begin{aligned} -\frac{2}{\gamma_r-1} &< r \le 0 , \\ \frac{u_l-u_r}{a_r} &\le r < \frac{u_l-u_r}{a_r}+\left(\frac{2}{\gamma_l-1}\right)\frac{a_l}{a_r} . \end{aligned} \tag{1.53}$$

1.2.2 Acoustic approximation

The solution to the Riemann problem becomes easier to obtain when the initial conditions are such that the waves R and L shown in Fig. 1.7 are so weak that linear-acoustic theory can be used. This happens when the distance, in some sense, between the two constant states r and l is small. The waves R and L can then be treated as acoustic waves with the pressure ratios across them given by the simple relations,

$$p_f = p_r + \sqrt{\gamma_r p_r \rho_r}\,(u_f - u_r) , \tag{1.54a}$$

$$p_f \;=\; p_l - \sqrt{\gamma_l p_l \rho_l}\,(u_f - u_l)\;. \tag{1.54b}$$

Combining Eqs. (1.54a) and (1.54b), one finds

$$u_f = \left(p_l - p_r + \sqrt{\gamma_r p_r \rho_r}\,u_r + \sqrt{\gamma_l p_l \rho_l}\,u_l\right) / \left(\sqrt{\gamma_r p_r \rho_r} + \sqrt{\gamma_l p_l \rho_l}\right)\;. \tag{1.55}$$

The densities behind these waves are given by

$$\rho_{fi} \;=\; \rho_i \left(p_f + \mu_i^2 p_i\right) / \left(p_i + \mu_i^2 p_i\right)\;, \tag{1.56}$$

where

$$\mu_i^2 \;\equiv\; (\gamma_i - 1)\,/\,(\gamma_i + 1)\;, \qquad i \;=\; r, l\,. \tag{1.57}$$

1.2.3 Reacting mixture of calorically perfect gases

So far, the classical Riemann problem for non-reacting, inviscid flow has been considered. The solution to this problem, as mentioned before, is a self-similar solution, *i.e.*, depending on x/t only. For the case of a simple reacting mixture, the nonlinear system of equations that needs to be solved is of the form

$$\frac{\partial U}{\partial t} + \frac{\partial F(U)}{\partial x} = G(U)\,, \tag{1.58}$$

where

$$U \;=\; \begin{pmatrix} \rho \\ \rho u \\ \rho\left(e + \frac{1}{2}\,u^2\right) \\ \rho z \end{pmatrix}\;, \quad F(U) \;=\; \begin{pmatrix} \rho u \\ \rho u^2 + p \\ \rho u\left(e + \frac{1}{2}\,u^2\right) + pu \\ \rho z u \end{pmatrix} \tag{1.59}$$

and

$$G(U) \;=\; \begin{pmatrix} 0 \\ 0 \\ 0 \\ -\rho \dot{z} \end{pmatrix}\;. \tag{1.60}$$

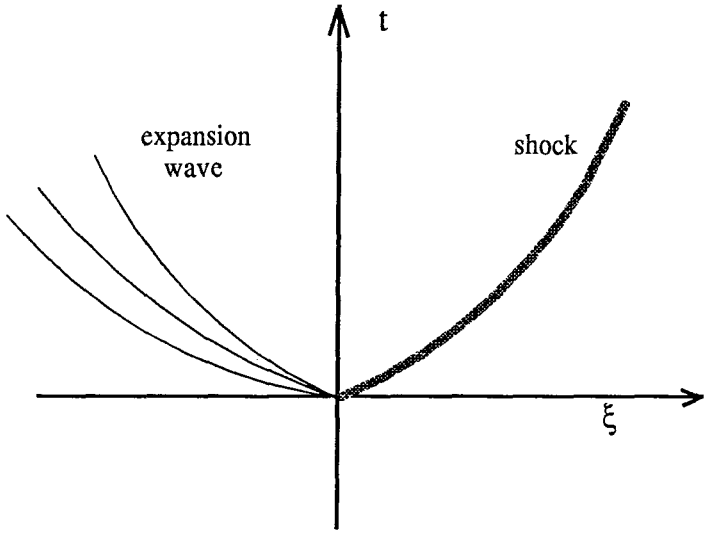

FIG.1.8 This is a typical wave pattern resulting from the breakup of the initial discontinuity of the Riemann problem for the case of a simple reacting mixture. The solution is no longer self-similar.

This is written using the Eulerian formulation, but one obtains a system of exactly the same form, if the Lagrangian formulation is used. The Riemann problem solution, described so far, is for the non-reacting case; *i.e.*, $G(U) = 0$. For the reacting case, jumps in the concentration of unburnt gas z are allowed only across contact discontinuities, but not across shocks. The solution to this problem is more complicated and no longer self-similar. In Fig. 1.8, a typical wave pattern is shown. The shock and expansion waves are curved in the (ξ, t) plane; *i.e.*, they are accelerating. The solution to this generalized Riemann problem has been worked out by Matania Ben-Artzi (1989). It is shown that the solution approaches the solution of the classical Riemann problem for the non-reacting case in the limit $\xi \to 0$ and $t \to 0$. The more complicated, generalized Riemann solver given by Ben-Artzi provides higher-order accuracy over the usual non-reacting solver. Numerical experiments were performed using the present, adaptive Lagrangian scheme with both Riemann solvers. It was found that the simpler solver gave results that were just as good. The acceleration of the various waves was captured numerically quite accurately.

1.3 Numerical Results

A number of test cases were run using this numerical scheme. The cases were chosen primarily to validate the code and to demonstrate its potential for solving 1-D problems with complicated wave interactions. The scheme is particularly useful for computing unsteady reacting flows involving detonation waves and their interactions.

1.3.1 Sod's shock-tube problem

The first case is the classical shock-tube problem. It is an important validation run for the code. The initial conditions used are those proposed by Sod (1978). At time $t = 0$ a diaphragm at the location $x = 0.5$ separates the two constant states

$$\begin{aligned} p_l &= 1.0 \quad \rho_l = 1.0 \quad u_l = 0.0\,, \quad x < 0.5 \\ p_r &= 0.1 \quad \rho_r = 0.125 \; u_r = 0.0\,, \quad x > 0.5\,, \end{aligned} \tag{1.61}$$

for a perfect gas with $\gamma = 1.40$. $N = 150$ computational cells are used in this calculation. In all the results presented, the solutions are given as functions of the Eulerian space variable x, even though the calculation is done in Lagrangian space. The Lagrangian aspect of the scheme is evident by the increased density of computational points in compression regions. The comparison between the numerical solution and the exact solution shown in Fig. 1.9 is excellent. Note that the expansion wave is computed with the accuracy of typical shock-capturing schemes, since no effort is made to track expansion waves. The shock-wave and the contact discontinuity are computed with no smearing.

In order to demonstrate the ability of the scheme to compute complicated wave interactions accurately, the shock-tube problem is carried a step further. Reflecting walls are assumed present at the locations $x = 0$ and $x = 1$. The computation is continued, to see how the multiple reflections of the shock from the walls and its collisions with the contact discontinuity are calculated. In Fig. 1.10, the solution is shown after the first reflection of the shock-wave from the wall at $x = 1$, which occurs at $t = 0.285$. In Fig. 1.11, the reflected shock has collided with the contact discontinuity and a new shock-wave has been generated. The solution at a later time is shown in Figs. 1.12. The computation was carried out until time $t = 7.88$. Many

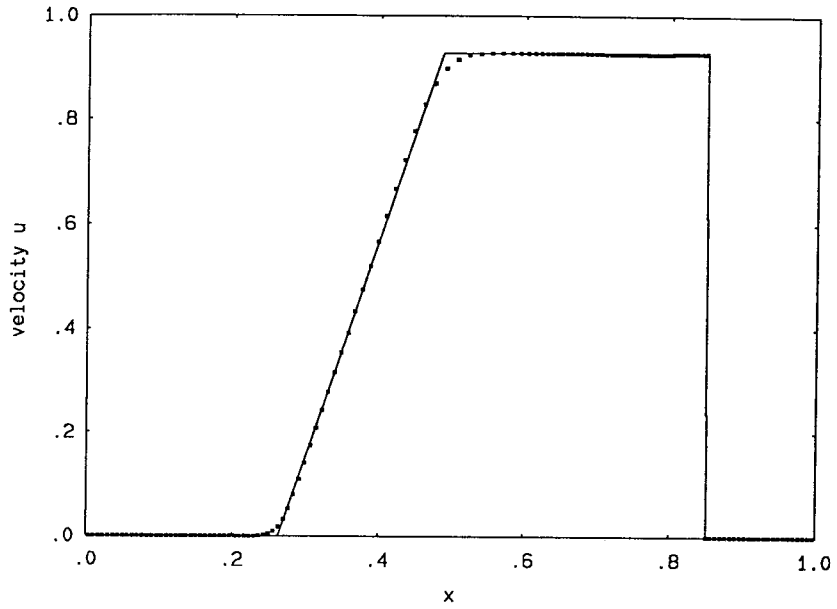

FIG.1.9a Velocity profile at time $t = 0.20$ for Sod's shock-tube problem with $N = 150$ computational cells. The solid line represents the exact solution and the boxes represent the numerical solution.

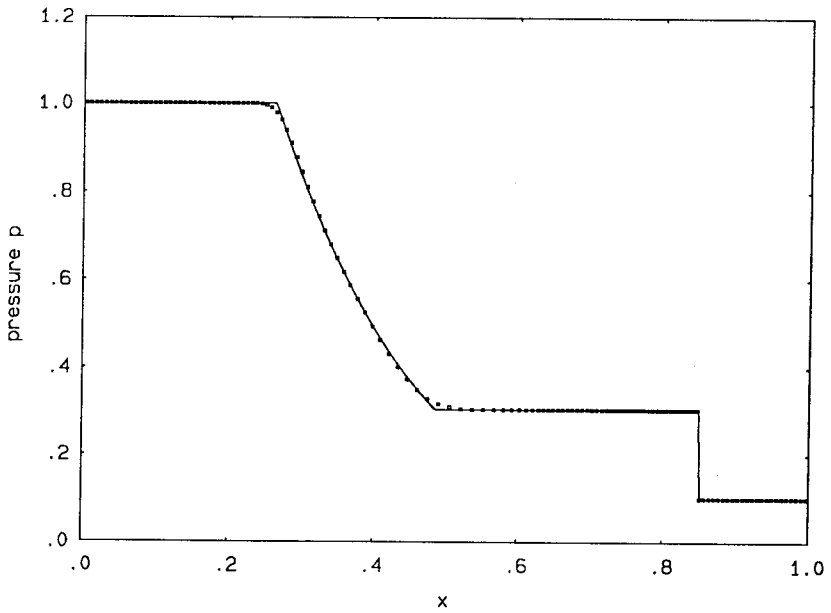

FIG.1.9b Pressure profile at time $t = 0.20$ for Sod's shock-tube problem with $N = 150$ computational cells. The solid line represents the exact solution and the boxes represent the numerical solution.

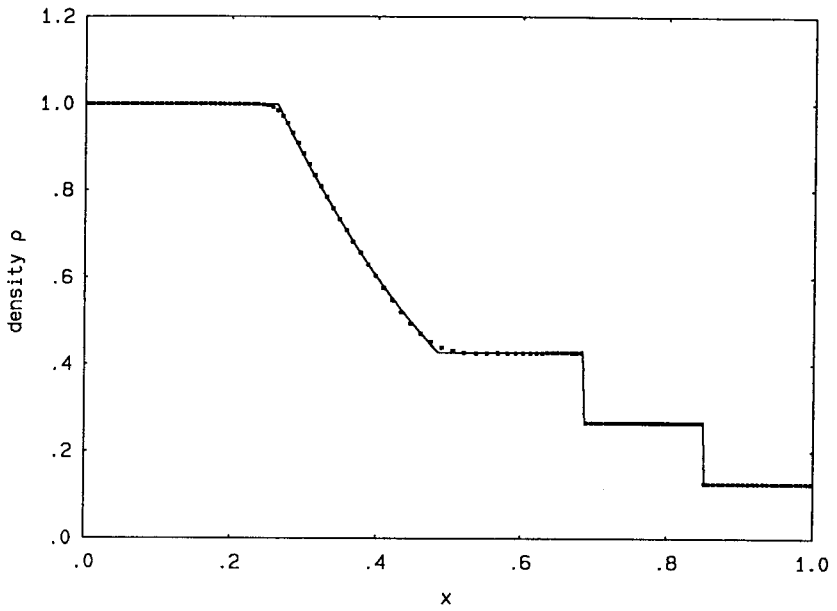

FIG.1.9c Density profile at time $t = 0.20$ for Sod's shock-tube problem with $N = 150$ computational cells. The solid line represents the exact solution and the boxes represent the numerical solution.

reflections of the original shock have occured by this time. In a real experiment viscous effects would have made the process die down much sooner. In Fig. 1.13, the entropy of the system is shown as a function of time. The entropy is defined by

$$s \equiv \ln(p/\rho^{\gamma}) \ . \tag{1.62}$$

As $t \to \infty$, the system approaches the state predicted by thermodynamics, since the scheme is fully conservative. Any scheme that conserves total mass and energy will give the correct final entropy. In this case it is $s = 0.1168$ in the appropriate dimensionless units. This is an important point worth repeating here. The conservative character of the scheme is not compromised by use of the adaptive grid technique.

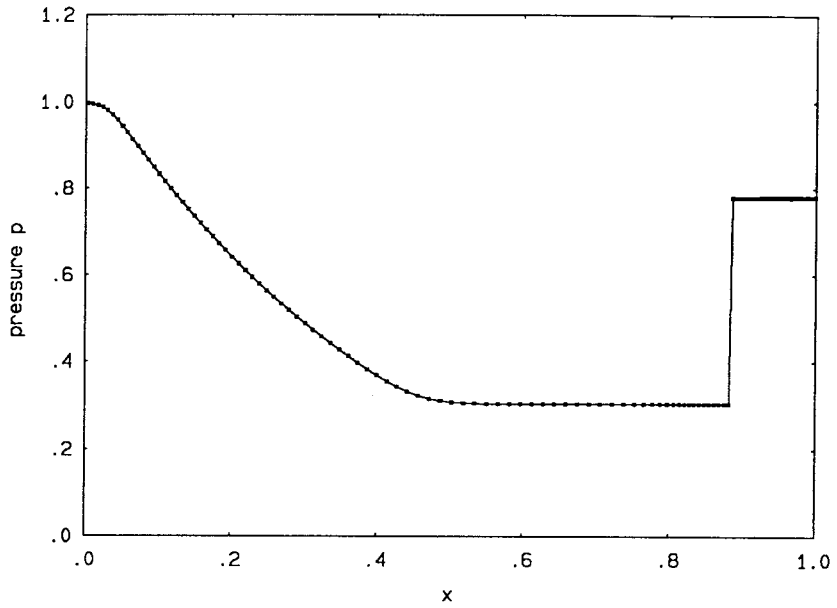

FIG.1.10a Pressure profile at time $t = 0.40$. The shock has reflected from the wall at $x = 1$.

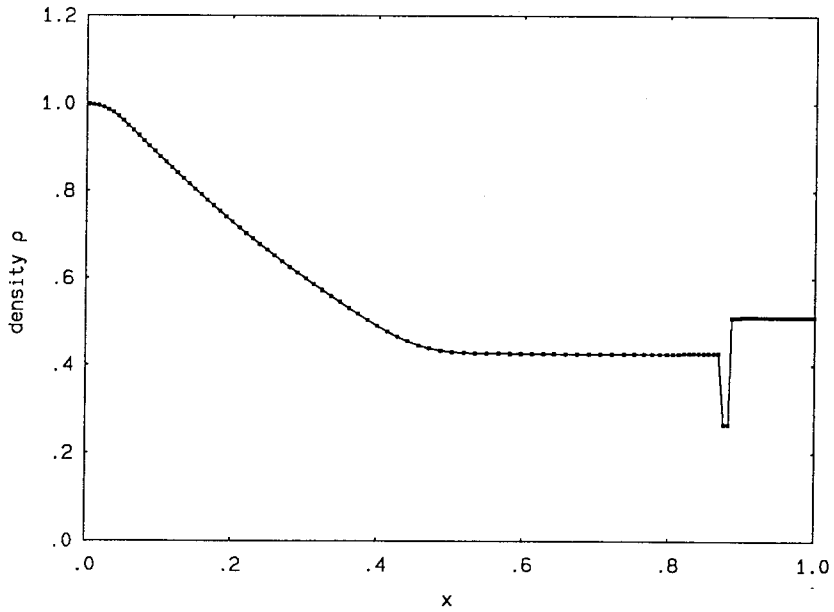

FIG.1.10b Density profile at time $t = 0.40$. The shock has reflected from the wall at $x = 1$.

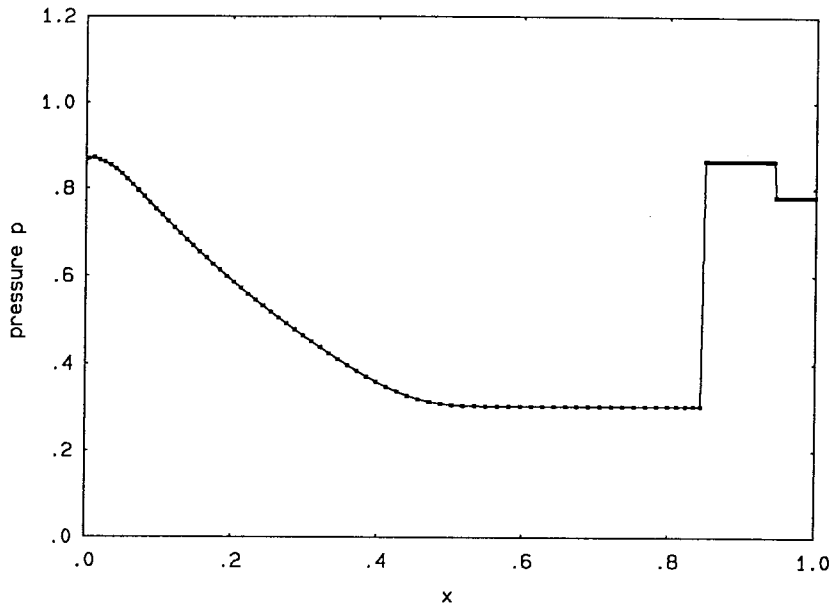

FIG.1.11a Pressure profile at time $t = 0.45$. The reflected shock has collided with the contact discontinuity. A secondary shock has been generated.

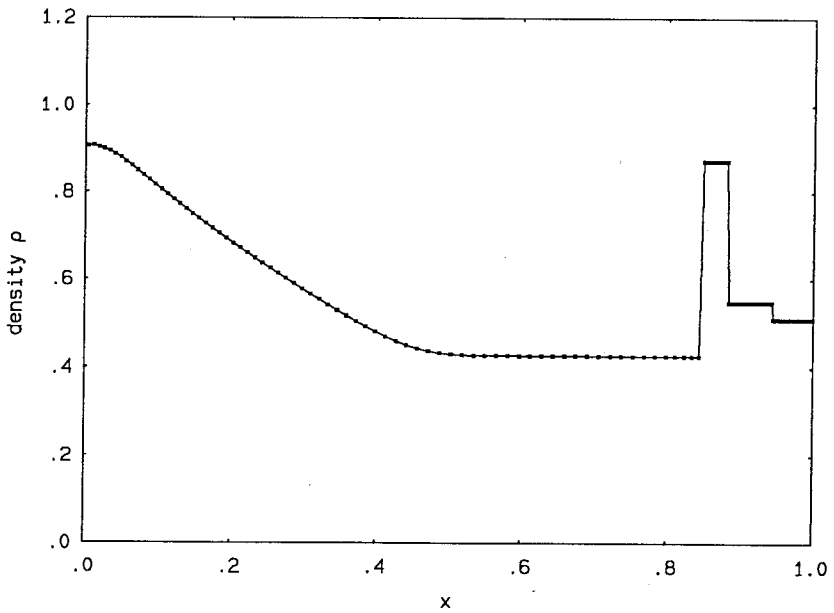

FIG.1.11b Density profile at time $t = 0.45$. The reflected shock has collided with the contact discontinuity. A secondary shock has been generated.

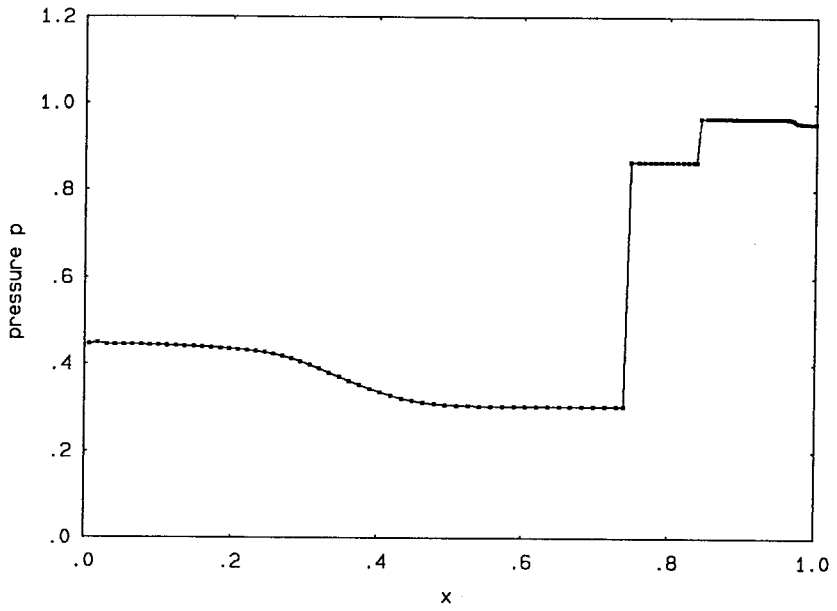

FIG.1.12a Pressure profile at time $t = 0.61$. An acoustic wave has been generated from the collision of the secondary shock with the contact discontinuity.

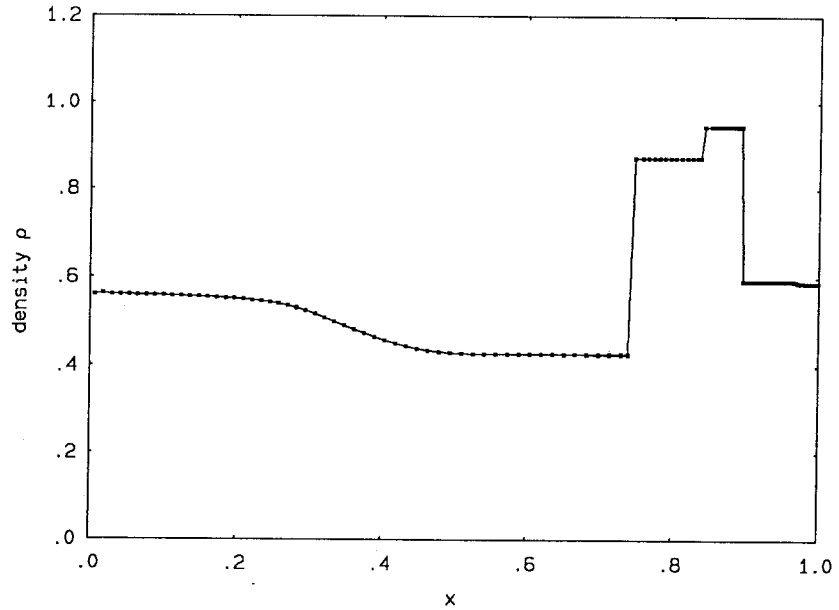

FIG.1.12b Density profile at time $t = 0.61$. An acoustic wave has been generated from the collision of the secondary shock with the contact discontinuity.

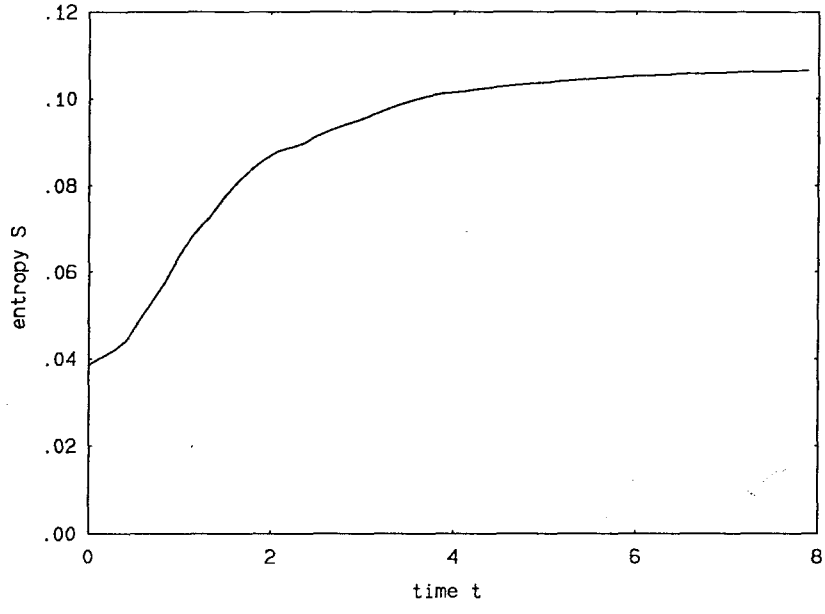

FIG.1.13 Entropy $s = \ln(p/\rho^\gamma)$ of the system as a function of time for the shock-tube problem with multiple reflections.

1.3.2 Strong shock-wave problem

The strong shock-wave problem used by Woodward and Colella (1984) is computed with the present scheme. This problem is a good test case, because of the strong interacting discontinuities. The initial condition is that of a gas with specific heat ratio $\gamma = 1.4$ at rest in the tube $0 \leq x \leq 1$. The initial density is $\rho = 1$ and the pressure is

$$\begin{aligned} p &= 1000\,, \qquad x < 0.1\,, \\ p &= 0.01\,, \qquad 0.1 < x < 0.9\,, \\ p &= 100\,, \qquad 0.9 < x < 1\,. \end{aligned} \tag{1.63}$$

The results are shown in Figs. 1.14 and Figs. 1.15 for the times $t = 0.030$ and $t = 0.038$, respectively. 800 computational cells were used for this calculation.

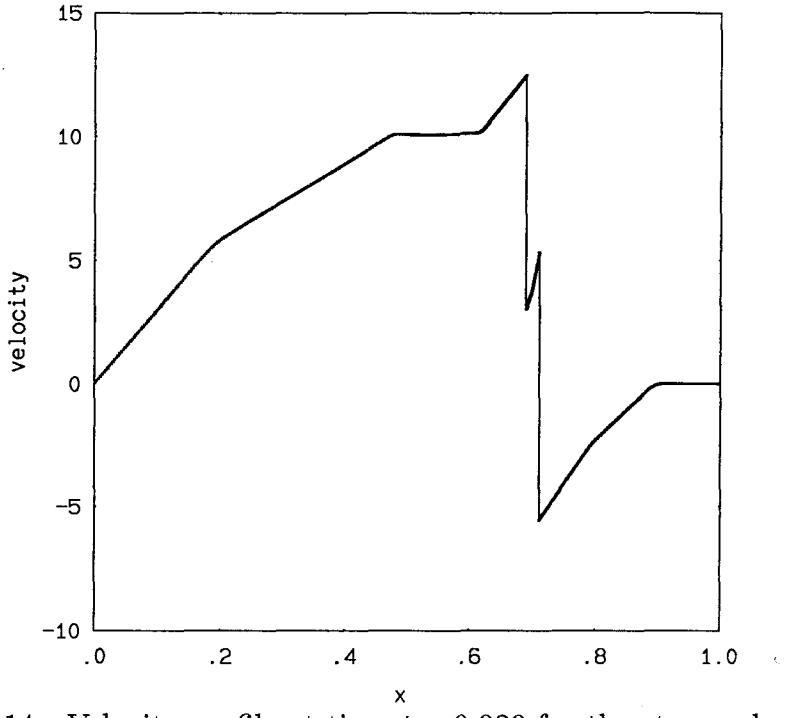

FIG.1.14a Velocity profile at time $t = 0.030$ for the strong shock-wave problem.

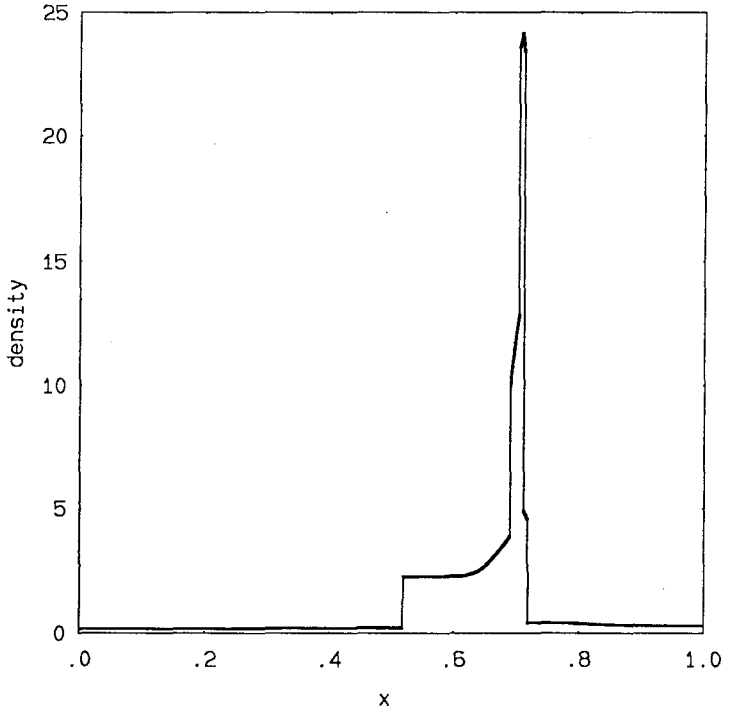

FIG.1.14b Density profile at time $t = 0.030$ for the strong shock-wave problem.

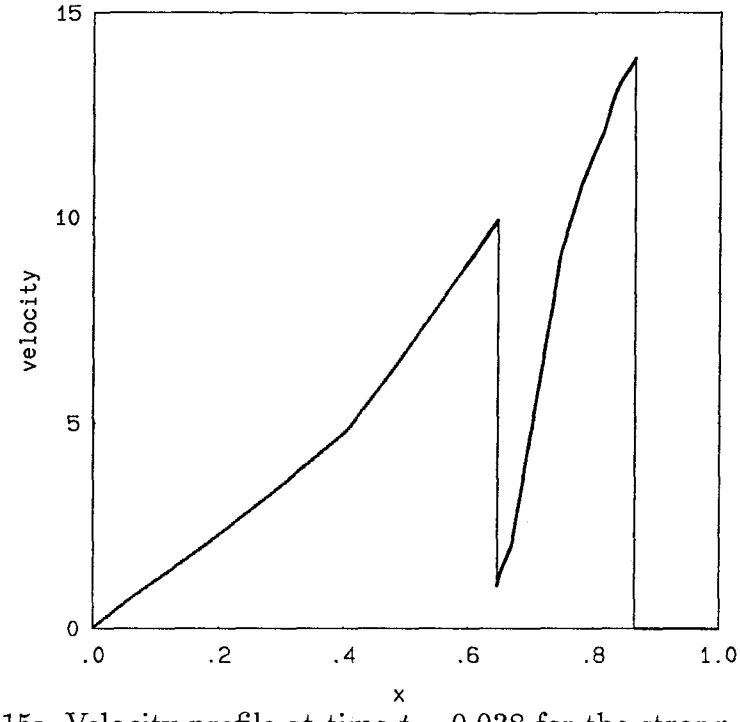

FIG.1.15a Velocity profile at time $t = 0.038$ for the strong shock-wave problem.

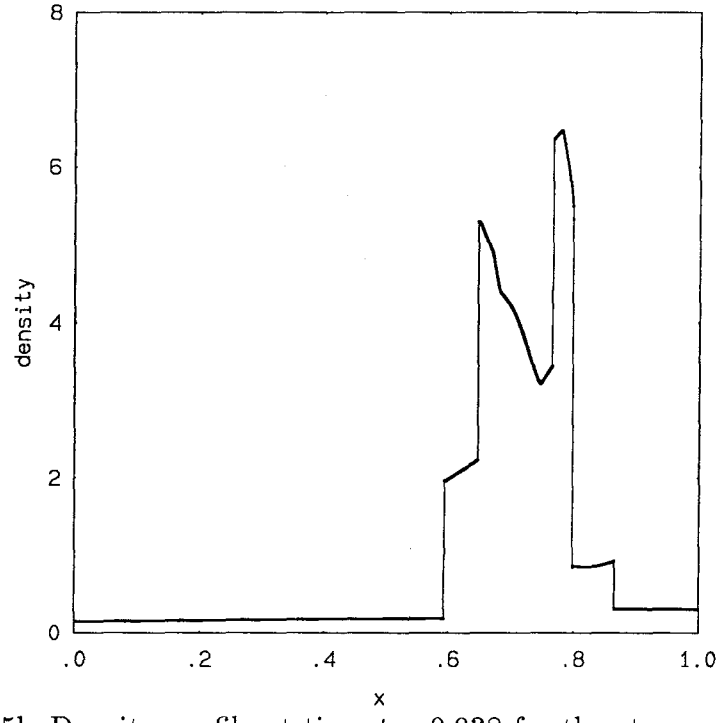

FIG.1.15b Density profile at time $t = 0.038$ for the strong shock-wave problem.

1.3.3 ZND detonation waves

Another test case is that of a steady detonation wave. The well-known ZND theory (Zel'dovich-VonNeumann-Doering) for a steady detonation is used to compare with the numerical solution obtained using this scheme. As a first check, the profile of a steady detonation wave, computed using the ZND theory, is given as the initial condition to the unsteady code. The solution after time $t = 10$ (10,000 timesteps) is then superimposed on the ZND solution and compared. The comparison, shown in Fig. 1.16, is excellent. The standard Arrhenius law, given by Eq. (1.1a), is used for the chemical reaction rate with $\alpha = 0$; *i.e.*,

$$\dot{z} \;=\; -Kz\, T^{\alpha} \exp\left(-E/R_g T\right) \;.$$

The parameters used for this test run are

$$\gamma \;=\; 1.2\,, \qquad q_0/R_g T_0 \;=\; 50\,, \qquad E/R_g T_0 \;=\; 40\,,$$

where the subscript zero denotes the undisturbed region into which the detonation propagates. This steady detonation wave corresponds to an overdrive factor of $f = 1.6$. The overdrive factor is defined by

$$f \;=\; D^2/D^2_{\rm CJ}\,,$$

where D is the detonation wave speed and D_{CJ} is the detonation speed corresponding to the Chapman-Jouguet point. For details on the ZND theory, see the book by Fickett and Davis (1979).

The case of unsteady detonation waves will now be considered. For the following cases the simplified Arrhenius chemical-rate law is used (Eq. (1.1b)); *i.e.*,

$$\dot{z} \;=\; -KzH\left(T - T_c\right)\,,$$

where T_c is a critical temperature above which the chemical reaction begins. Fig. 1.17 shows the evolution of an unsteady detonation propagating in an undisturbed region. It is the well-known piston problem. The motion of the piston, starting at $x = 0$, generates a shock that raises the temperature of the gas above the critical value T_c. The chemical reaction begins and the detonation wave accelerates into the undisturbed region. The numerical values used in this run are

$$\gamma \;=\; 1.4\,, \qquad q_0 \;=\; 20\,, \qquad T_c \;=\; 1.3\,,$$

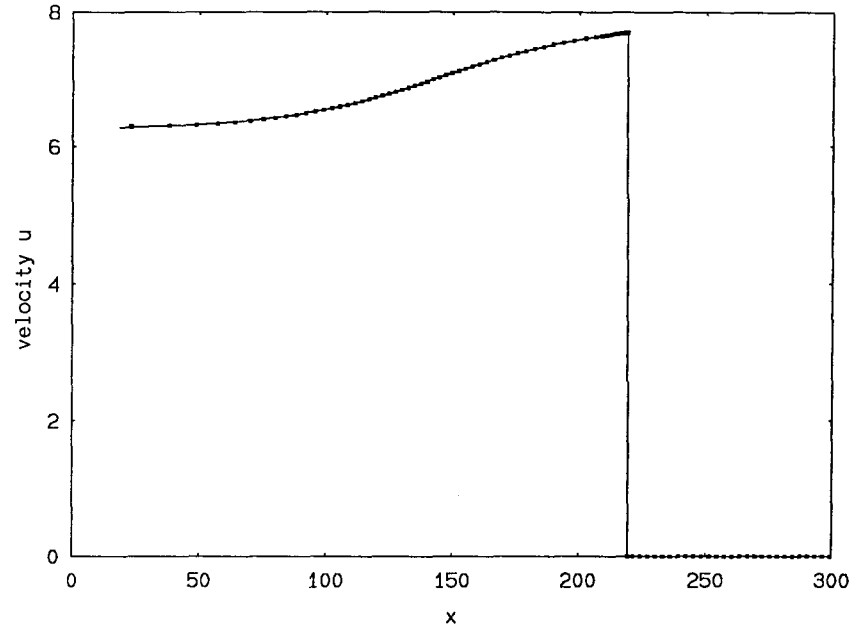

FIG.1.16a Velocity profile at $t = 10$. The solid line is the solution given by the ZND theory. The boxes are the numerical solution.

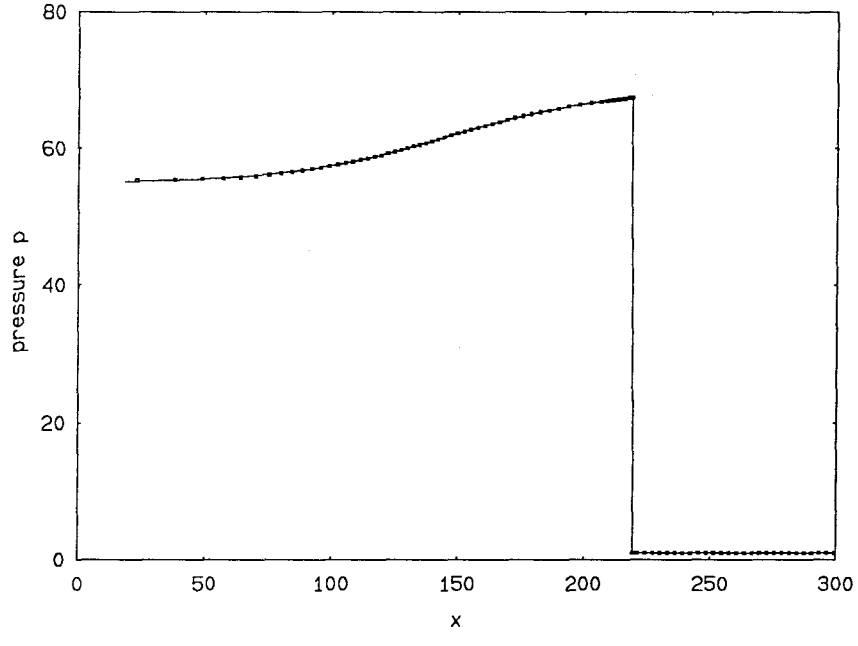

FIG.1.16b Pressure profile at $t = 10$. The solid line is the solution given by the ZND theory. The boxes are the numerical solution.

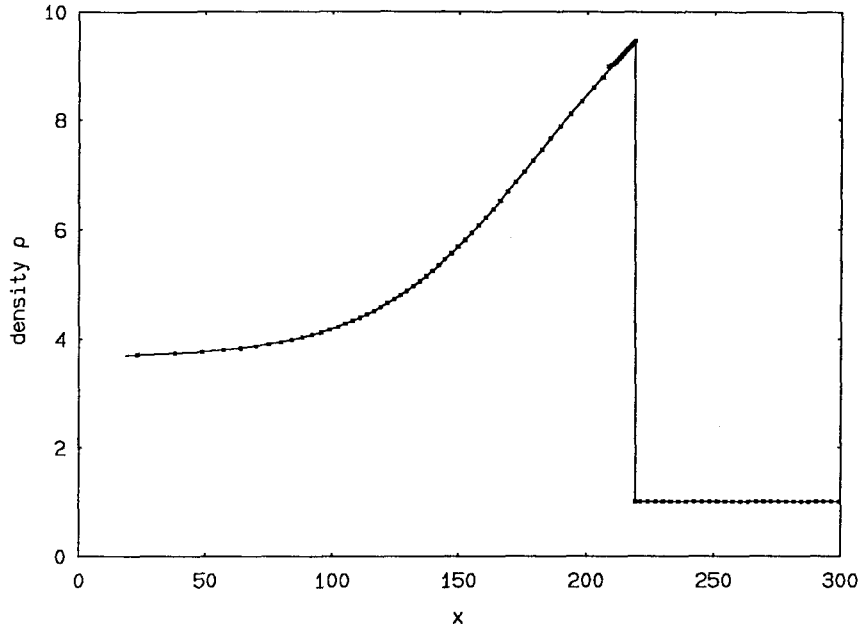

FIG.1.16c Density profile at $t = 10$. The solid line is the solution given by the ZND theory. The boxes are the numerical solution.

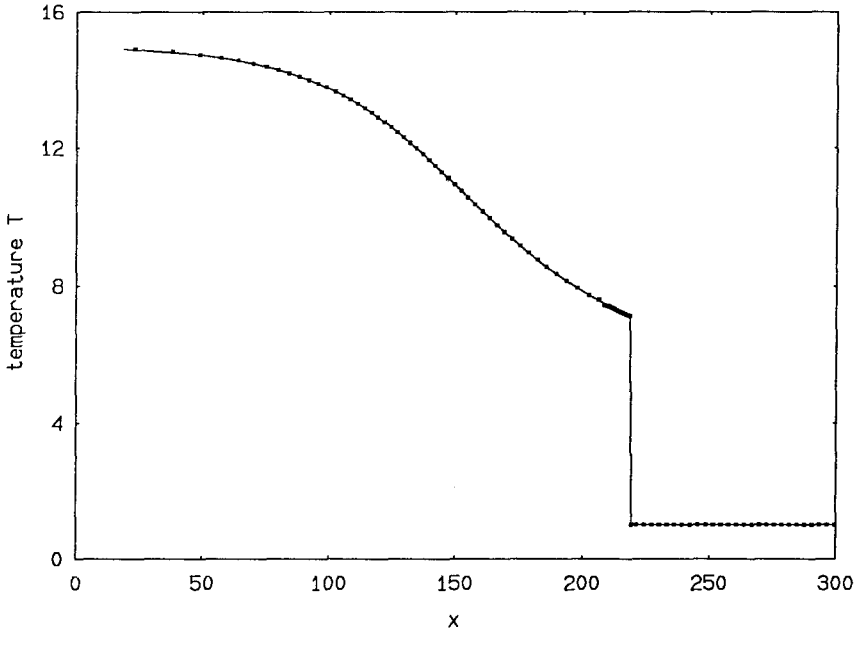

FIG.1.16d Temperature profile at $t = 10$. The solid line is the solution given by the ZND theory. The boxes are the numerical solution.

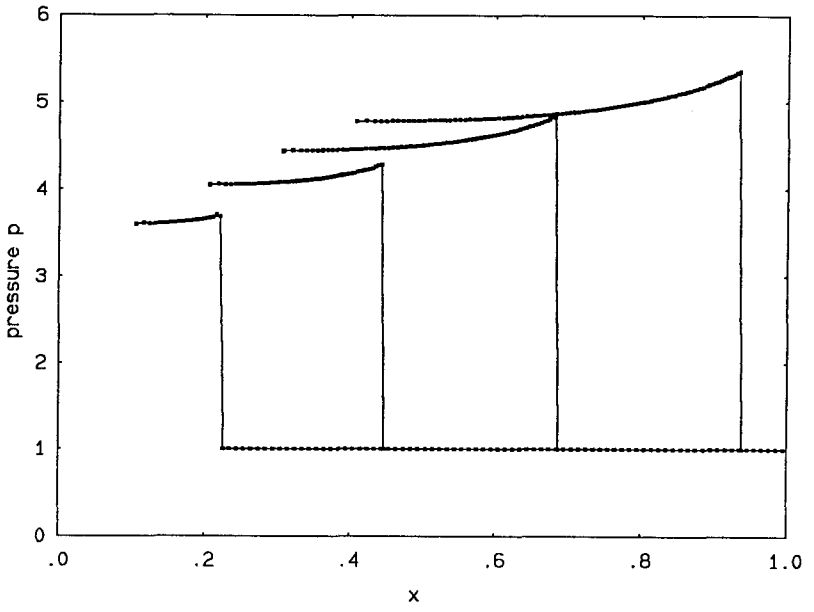

FIG.1.17a Pressure profiles for the piston problem. The detonation wave generated accelerates into the undisturbed region. In this case the critical temperature is $T_c = 1.3$. Times $t = 0.1,\ 0.2,\ 0.3,\ 0.4$.

where all quantities are normalized with the corresponding values in the undisturbed region. The piston velocity is taken to be $u_p = 1$.

A more interesting case is shown in Fig. 1.18. The initial condition is a smooth pressure distribution with zero initial velocity, which leads to isentropic compression and eventually to shock formation. If in this compression the temperature of the gas becomes larger than T_c, then the chemical reaction starts, and a detonation wave is generated. The formation of the shock from a smooth flow is captured very well by this scheme. $N = 200$ computational cells were used. The numerical values used in this run are

$$\gamma = 1.4\,, \qquad q_0 = 20\,, \qquad T_c = 1.2\,, \qquad K = 1\,,$$

where all quantities are normalized appropriately. The normalization is such that the initial temperature of the gas at rest is $T_0 = 1$, or equivalently, $\rho_0 = p_0$ in dimensionless units. The initial pressure distribution is given by

$$p_0(x) = 0.10 + 3.0\exp(-25x^2)\,.$$

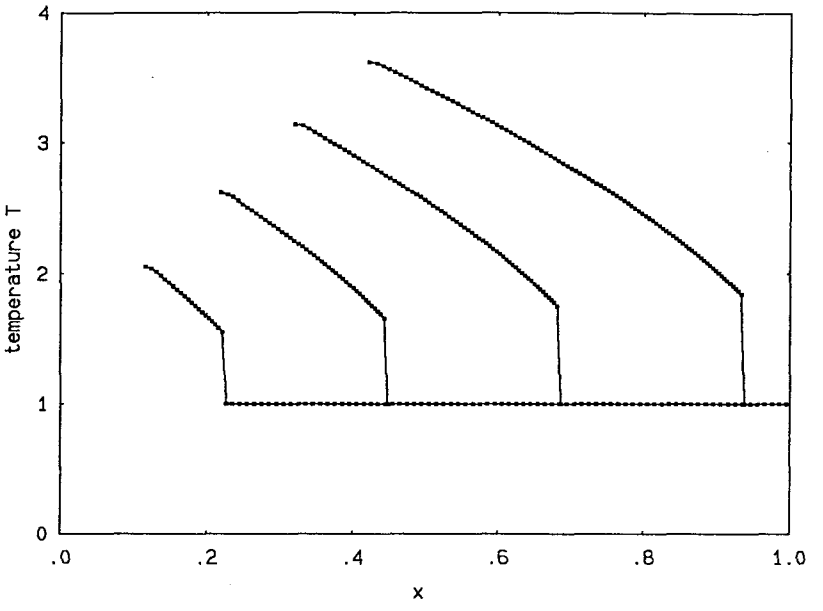

FIG.1.17b Temperature profiles for the piston problem. The detonation wave generated accelerates into the undisturbed region. In this case the critical temperature is $T_c = 1.3$. Times $t = 0.1,\ 0.2,\ 0.3,\ 0.4$.

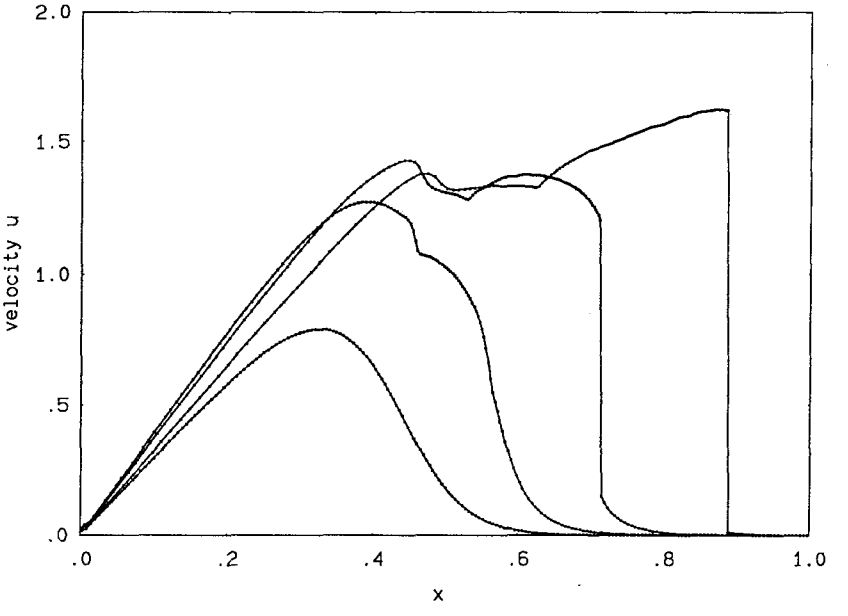

FIG.1.18a Velocity profiles for a smooth compression. When the compression raises the temperature above the critical value $T_c = 1.2$, the reaction begins and a detonation wave is formed. Times $t = 0.075,\ 0.150,\ 0.225,\ 0.300$.

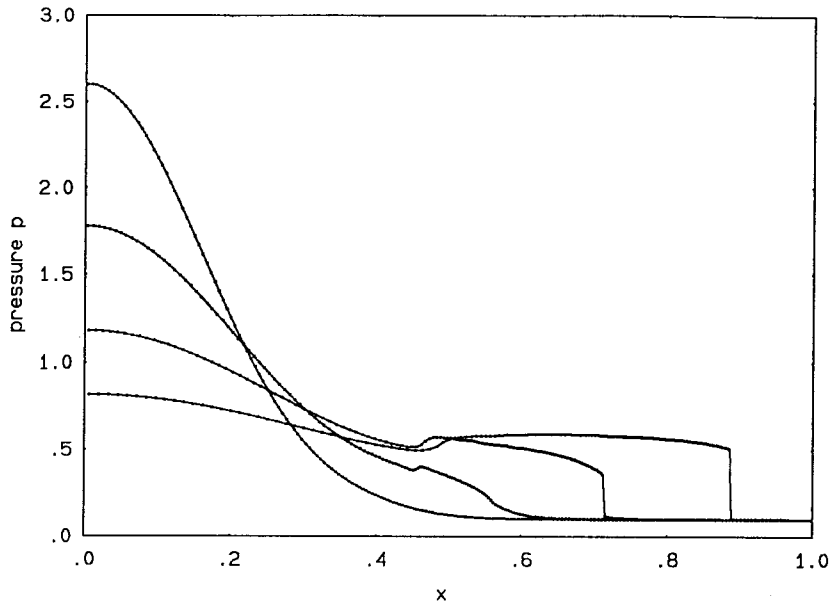

FIG.1.18b Pressure profiles for a smooth compression. When the compression raises the temperature above the critical value $T_c = 1.2$, the reaction begins and a detonation wave is formed. Times $t = 0.075,\ 0.150,\ 0.225,\ 0.300$.

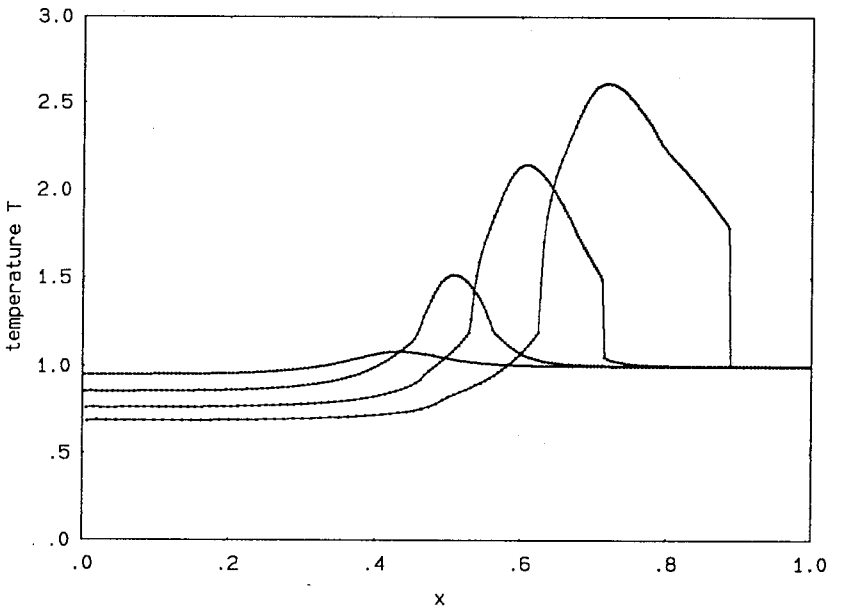

FIG.1.18c Temperature profiles for a smooth compression. When the compression raises the temperature above the critical value $T_c = 1.2$, the reaction begins and a detonation wave is formed. Times $t = 0.075,\ 0.15,\ 0.225,\ 0.3$.

1.4 Conclusions

An adaptive numerical scheme has been presented for the computation of flows with complicated interactions of discontinuity waves. Its accuracy and robustness, as demonstrated by numerical experiments make it a valuable tool, especially for the study of unsteady reacting flows with detonation waves. The conservative formulation gives the method all the advantages of higher-order shock-capturing schemes and its adaptive characteristic allows for good accuracy near shocks with no smearing effect. The advantages of the conservative shock-capturing schemes are combined with the advantages of the front-tracking methods very well to give a useful computational scheme.

The drawback is that the extension of this scheme to multidimensional flows is not straightforward. The main idea of the scheme is the conservative front-tracking of shocks and contact discontinuities on a Lagrangian grid. The Lagrangian aspect of the method is the most difficult to extend. The conservative front-tracking aspect can be extended and work in this area is in progress.

CHAPTER 2

Riemann Invariant Manifolds

Progress has been made in recent years in the development of numerical schemes for computing hyperbolic systems of equations. This has been motivated by the need to perform reliable numerical simulations of compressible flows. The presence of shocks in these flows complicates matters. Older shock-capturing schemes, which are more than first-order accurate, produced spurious oscillations in the vicinity of discontinuities. A new generation of methods was developed to overcome the problems of the simple, conservative, finite-difference schemes. These high-resolution schemes, such as the ENO and TVD schemes, described by Harten *et al.* (1987) and Harten (1983,1984), the MUSCL scheme introduced by van Leer (1979), PPM by Colella and Woodward (1984) and Roe's Approximate Riemann Solver given by Roe (1981), take advantage of the extensive theory on hyperbolic systems of equations in two independent variables. The two variables are, usually, time and one spatial variable. The primary application is the one-dimensional flow of a gas. Most of these schemes are based on the original Godunov scheme (1959). The main idea is to use the knowledge from the theory of characteristics, locally in each computational cell, to compute the various flux terms. By doing this, the local characteristic wave patterns are accurately accounted for. Since discontinuities are likely to be present, the characteristic problem is generalized to allow for their presence. This constitutes the well-known Riemann problem. Two arbitrary, constant states, separated by a discontinuity in space, are given as the initial condition. For 1-D gas dynamics, it can be shown that the Riemann problem has a unique solution and that the general, initial value problem has a unique weak solution. See Glimm (1965) and Smoller (1983). The Riemann problem reduces to the known characteristic problem in the absence of discontinuities. The solution to the Riemann problem is used as the building block for numerical methods of this type. It provides the information needed to compute the fluxes at the interfaces of the computational cells.

Although the application of this idea is straightforward for the one-dimensional case, the extension to multidimensional flows is not. Practically, these schemes are extended to more dimensions by treating the additional spatial dimensions separately. The computation is not truly multidimensional, but rather a number of separate, one-dimensional computations in each spatial direction. Even schemes that appear to be multidimensional (unsplit), actually use the local directions of the grid to set up and solve a 1-D Riemann problem, thus taking advantage of the 1-D results. The only real effort to create a multidimensional scheme is that by Roe (1986); Hirsch & Lacor (1989), and Deconinck *et al.* (1986). These efforts are within the context of conservative, shock-capturing schemes of the Godunov type. Butler (1960) has shown a possible extension of the method of characteristics for computing unsteady, two-dimensional flows. This scheme is also genuinely multidimensional.

In what follows, the multidimensional flow of a gas is examined. A brief summary of the theory of characteristic surfaces for hyperbolic systems in several independent variables is given as background. It is then shown how it is possible to find surfaces in spacetime, that are convenient for computational purposes. The solution along any curve on these surfaces satisfies relations completely analogous to the 1-D characteristic relations. In the special case of zero-entropy gradients, it is possible to define functions analogous to the Riemann invariants in 1-D. If N is the number of spatial dimensions, there is, in general, an $(N-1)$-parameter family of such N-dimensional manifolds in spacetime on which these generalized Riemann Invariants are constant. These manifolds are referred to as Riemann Invariant Manifolds. They can be constructed locally by an appropriate set of curves. These curves are the integral curves of a vector field in spacetime, which depends on the local spatial gradients of the solution. The local geometry of these manifolds is examined, and in particular, their location with respect to the characteristic manifolds. It is the characteristic manifolds that determine the domains of dependence and domains of influence of the solution in regions of spacetime. The concepts of domains of dependence and influence are closely related to the important existence and uniqueness theorems for solutions of such systems. See Courant and Hilbert (1963); Friedrichs (1954); Friedrichs and Lax (1965), and Kato (1975). It turns out that the Riemann Invariant Manifolds may be space-like or time-like with respect to the bicharacteristic cone. A parameter μ_n is introduced, which plays the role of an algebraic Mach number for these manifolds. It depends on the local flow gradients

and gives an indication of how close the particular Riemann Invariant Manifold is to the bicharacteristic cone.

Weak solutions are not examined in this analysis. Although the solution is assumed to be continuous with possible discontinuities only in the derivatives, it is hoped that it will be clear as to how the results can be used in the cases where shocks, *i.e.*, jump discontinuities, are present. The examination of these special manifolds in spacetime provides a means of determining spatial directions in the flow, which are special in some sense. There are directions that provide obvious computational advantages, but there are also directions that are optimal when a shock is present. Finding the appropriate directions may actually allow the general 1-D Riemann problem to be used consistently in multidimensional flows.

This theory of Riemann Invariant Manifolds can best be viewed as an extension of the method of characteristics to multidimensional flows. It can be viewed as the the theoretical framework for developing numerical schemes in the spirit of Butler (1960).

2.1 Hyperbolic Systems

2.1.1 Characteristic Surfaces

The basic ideas of the theory of hyperbolic equations in many independent variables and the theory of characteristic surfaces are presented in this section to serve as background for what follows. For a more detailed exposition, see Courant and Hilbert (1963). The practical problem of interest is the unsteady flow of a compressible fluid in more than one space dimension. This is a specific case of the general hyperbolic system of equations in several independent variables of the form

$$\frac{\partial U}{\partial t} + \frac{\partial F_m(U)}{\partial x_m} = 0 \qquad m = 1, \ldots, N \,, \tag{2.1}$$

where $U \in \Re^M$ is the M-dimensional solution vector, N is the spatial dimension of the problem and (F_m) is the flux vector. Time has been chosen as a special independent variable, and the summation convention is assumed. Eq. (2.1) describes a conservation law and is equivalent to the following quasi-linear form

$$\frac{\partial U}{\partial t} + A_m \frac{\partial U}{\partial x_m} = 0 \qquad m = 1, \ldots, N \,, \tag{2.2}$$

where the A_m are the Jacobian matrices, given by

$$A_m \equiv \frac{\partial F_m(U)}{\partial U} . \tag{2.3}$$

A linear system is one for which the matrices A_m are independent of the solution U. The solution is also assumed to be sufficiently smooth for all operations performed to have meaning.

It is sometimes useful not to single out the time variable t. The advantage of this is that the conservation law, Eq (2.1), takes the particularly simple form of a divergence in spacetime,

$$\frac{\partial F_\mu(U)}{\partial x_\mu} = A_\mu \frac{\partial U}{\partial x_\mu} = A_0 \frac{\partial U}{\partial t} + A_m \frac{\partial U}{\partial x_m} = 0 \qquad \mu = 0, 1, \ldots, N , \tag{2.4}$$

where $x_0 \equiv t$. Greek subscripts will be used when time is not singled out as a special variable. In what follows, A_0 is usually taken to be the identity matrix I. It is also useful sometimes to write (2.1) and (2.2) using absolute notation,

$$\begin{aligned} \frac{\partial U}{\partial t} + \nabla \cdot \mathbf{F}(U) &= 0 \\ \frac{\partial U}{\partial t} + \mathbf{A} \cdot \nabla U &= 0 , \end{aligned} \tag{2.5}$$

where

$$\begin{aligned} \nabla &\equiv \left(\frac{\partial}{\partial x_m} \right) \\ \mathbf{F} &\equiv (F_m) \\ \mathbf{A} &\equiv (A_m) . \end{aligned} \tag{2.6}$$

In order for this system of equations to be hyperbolic, the matrices A_m must satisfy certain conditions. The concept of hyperbolicity is related to the existence of special surfaces in spacetime, which are called characteristic surfaces. The quest for such surfaces is motivated by the Cauchy Initial Value Problem (IVP) for Eq. (2.2). Consider a surface $\varphi(t, \mathbf{x}) = 0$, $\mathbf{x} \in \Re^N$, in spacetime. The Cauchy IVP consists in specifying initial data U on this surface and using Eq. (2.2) to find the solution $U = U(t, \mathbf{x})$ off the surface. The natural question to ask is whether this is possible for any surface $\varphi(t, \mathbf{x}) = 0$.

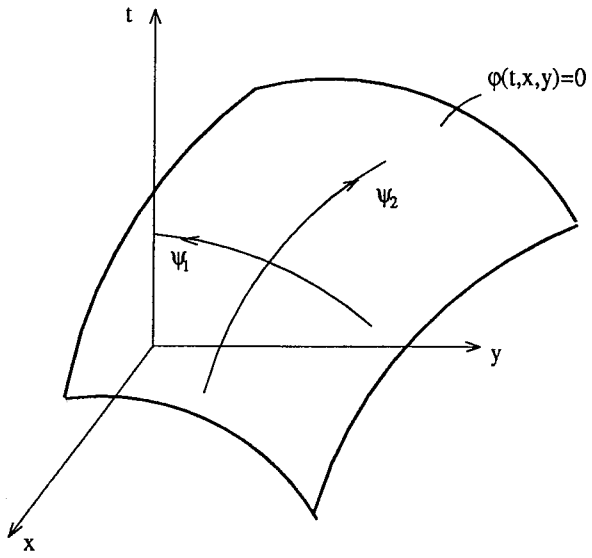

FIG.2.1 The surface $\varphi(t, \mathbf{x}) = 0$ in three-dimensional spacetime.

For visualization purposes, it is convenient to consider the special case $N = 2$. Spacetime is now a three-dimensional space. See Fig. 2.1.

Consider the general coordinate transformation

$$\begin{aligned} \varphi &= \varphi(t, \mathbf{x}) \\ \psi_k &= \psi_k(t, \mathbf{x}) \qquad\qquad k = 1, \ldots, N \,, \end{aligned} \tag{2.7}$$

where the given surface $\varphi(t, \mathbf{x}) = 0$ is used as one of the new coordinate surfaces. The transformation is assumed to be smooth, with a non-vanishing Jacobian at the points of interest. It is easy to see that

$$\begin{aligned} \frac{\partial U}{\partial t} &= \frac{\partial \varphi}{\partial t}\frac{\partial U}{\partial \varphi} + \frac{\partial \psi_k}{\partial t}\frac{\partial U}{\partial \psi_k} \\ \frac{\partial U}{\partial x_m} &= \frac{\partial \varphi}{\partial x_m}\frac{\partial U}{\partial \varphi} + \frac{\partial \psi_k}{\partial x_m}\frac{\partial U}{\partial \psi_k} \,, \end{aligned} \tag{2.8}$$

where U is now considered a function of the new variables; *i.e.*, $U = U(\varphi, \psi_k)$. Substituting Eqs. (2.8) in (2.2), one finds

$$\left(\frac{\partial \varphi}{\partial t} I + \frac{\partial \varphi}{\partial x_m} A_m\right)\frac{\partial U}{\partial \varphi} + \left(\frac{\partial \psi_k}{\partial t} I + \frac{\partial \psi_k}{\partial x_m} A_m\right)\frac{\partial U}{\partial \psi_k} = 0 \,. \tag{2.9}$$

Assume that initial data are given on $\varphi = 0$. Then all the tangential derivatives

$$\frac{\partial U}{\partial \psi_k} \,, \qquad k = 1, \ldots, N \,,$$

are known from the initial data, and only the derivative in the normal direction, *i.e.*,

$$\frac{\partial U}{\partial \varphi} ,$$

is unknown. This normal derivative can be found by solving for it in Eq. (2.9). By differentiating (2.9), similar algebraic equations can be found for the higher-order derivatives of U in the normal direction. One can, then, use these derivatives to construct the solution off the $\varphi = 0$ surface with the aid of a Taylor series expansion.

It can be seen from Eq. (2.9) that it is not possible to solve for the unknown derivative when

$$Q \equiv \det\left(\frac{\partial \varphi}{\partial t} I + \frac{\partial \varphi}{\partial x_m} A_m\right) = \det\left(\frac{\partial \varphi}{\partial x_\mu} A_\mu\right) = 0 . \tag{2.10}$$

A surface for which (2.10) holds, is called a *characteristic surface*. Q is a function of the first derivatives of φ and is called the *characteristic function*. $Q = 0$ is a first-order, differential equation for the function $\varphi = \varphi(t, \mathbf{x})$. Although Eq. (2.10) must hold only for $\varphi = 0$, one can embed this surface in the family of $\varphi = \text{const}$ surfaces. This family is the solution of the first-order, partial-differential equation (2.10). Note that all these relations are local. This is particularly important for nonlinear problems for which the matrices A_μ and thus the characteristic surfaces, depend on the solution U.

From the previous discussion it follows that the derivative of the solution normal to a characteristic surface cannot be determined by the differential equation and therefore, a discontinuity in this derivative is possible. The same holds for all higher-order, normal derivatives. Thus, one can define the characteristic surfaces as the surfaces across which discontinuities in the derivatives of the solution are possible. This definition is a little restrictive, because it implies that the characteristic surfaces are significant only when discontinuities are present, which is not the case.

A more useful definition is that characteristic surfaces are the surfaces on which the differential operator in (2.2) may become an "internal" operator. What is meant by this is seen from the transformed system (2.9). If

$$\left(\frac{\partial \varphi}{\partial t} I + \frac{\partial \varphi}{\partial x_m} A_m\right) \frac{\partial U}{\partial \varphi} = 0 , \tag{2.11}$$

for a particular vector $\dfrac{\partial U}{\partial \varphi}$, then the system of equations contains only derivatives on the surface, *i.e.*, no normal derivatives. For Eq. (2.11) to hold for a non-trivial value of the normal derivative, the surface $\varphi = 0$ must satisfy the condition given by (2.10); *i.e.*, it must be characteristic.

The differential operator

$$D \equiv A_\mu \frac{\partial}{\partial x_\mu} = I\frac{\partial}{\partial t} + A_m \frac{\partial}{\partial x_m} , \tag{2.12}$$

is hyperbolic if real characteristic surfaces exist. This requirement can be made more specific by defining

$$\begin{aligned} \mathbf{n} &\equiv \nabla\varphi / |\nabla\varphi| \\ \lambda &\equiv -\frac{\partial\varphi}{\partial t} / |\nabla\varphi| , \end{aligned} \tag{2.13}$$

where $\nabla\varphi$ is the spatial gradient of φ. Substituting in (2.10) one finds

$$\hat{Q} = \hat{Q}(\mathbf{n}, \lambda) \equiv \det(n_m A_m - \lambda I) = 0 , \tag{2.14}$$

which is the characteristic equation for the eigenvalue problem associated with the matrix $\mathbf{n}\cdot\mathbf{A} \equiv n_m A_m$. Given a spatial unit vector $\mathbf{n}$, if the eigenvalues λ_m , $m = 1, \ldots, M$, of $\mathbf{n}\cdot\mathbf{A}$ are real, then the operator D is hyperbolic. This must hold for any unit vector $\mathbf{n}$. The right eigenvectors of this matrix will be denoted by r_m and the left egenvectors by l_m. Thus,

$$\begin{aligned} (\mathbf{n}\cdot\mathbf{A})\, r_m &= \lambda_m r_m \\ (\mathbf{n}\cdot\mathbf{A})^{\mathrm{T}}\, l_m &= \lambda_m l_m \end{aligned} \qquad m = 1, \ldots, M \qquad \text{(No summation on } m) . \tag{2.15}$$

The characteristic function Q (or $\hat{Q}$) is of the form

$$Q = Q_1^{k_1} Q_2^{k_2} \cdots Q_p^{k_p} , \qquad k_j \in Z^+ , \quad j = 1, \ldots, p . \tag{2.16}$$

This is because the characteristic function is a polynomial in the derivatives of φ. The j^{th} factor in (2.16) corresponds to a particular type of characteristic manifold for the differential operator and to a particular eigenvalue λ_j in (2.14). k_j is the degeneracy of λ_j and the corresponding characteristic manifold. The j^{th} factor can be written, in general, as

$$Q_j = \frac{\partial\varphi}{\partial t} + H_j(\mathbf{x}, \nabla\varphi; U) = 0 . \tag{2.17}$$

The characteristic equation (2.17) is a first-order, partial-differential equation of the general form

$$F\left(x_\alpha, \varphi, \frac{\partial \varphi}{\partial x_\beta}\right) = 0 , \qquad \alpha, \beta = 0, 1, \ldots, N \tag{2.18}$$

for the function $\varphi = \varphi(x_\alpha)$. An extensive theory exists for such equations; *e.g.*, see Courant and Hilbert (1963). The solution of (2.18) is a surface in the $(N+2)$-dimensional space (φ, x_α).

It is important to note that this integral surface can be generated by a family of characteristic curves. An important special case of (2.18) is the Hamilton-Jacobi equation, which arises in many applications in physics, the best known being the Hamiltonian formulation of classical mechanics. This differential equation has a variational problem associated with it. The general form of the Hamilton-Jacobi equation is

$$\frac{\partial \varphi}{\partial t} + H(t, \mathbf{x}, \mathbf{p}) = 0 , \tag{2.19}$$

where H is the corresponding Hamiltonian function and $\mathbf{p}$ is defined as

$$\mathbf{p} \equiv \nabla \varphi . \tag{2.20}$$

The variable $x_0 = t$ is singled out as a special independent variable, usually time. Eq. (2.17) for the j^{th} characteristic manifold is of this form, with no explicit dependence of the Hamiltonian on time. The action in the Hamiltonian formulation of classical mechanics also satisfies an equation of this form. The space dimension N corresponds to the degrees of freedom of the mechanical system and $\mathbf{p}$, which is the spatial gradient of φ, corresponds to the generalized momentum. The following canonical system of ordinary differential equations,

$$\begin{aligned} \dot{\mathbf{x}}(t) &= \frac{\partial H}{\partial \mathbf{p}} \\ \dot{\mathbf{p}}(t) &= -\frac{\partial H}{\partial \mathbf{x}} , \end{aligned} \tag{2.21}$$

can then be used to generate the integral manifold $\varphi = \varphi(t, \mathbf{x})$ from some initial N-dimensional manifold in the space $(t, \mathbf{x}, \varphi)$. Eqs. (2.21) are used to find the trajectory $\mathbf{x} = \mathbf{x}(t)$ and $\mathbf{p} = \mathbf{p}(t)$ of the mechanical system in the phase space $(\mathbf{x}, \mathbf{p})$. They define the characteristic strips for the Hamilton-Jacobi Equation (2.19). From Eqs. (2.19) and (2.21), we see that along these paths in phase space,

$$\dot{\varphi}(t) = \dot{\mathbf{x}}(t) \cdot \mathbf{p}(t) - H\left[t, \mathbf{x}(t), \mathbf{p}(t)\right] . \tag{2.22}$$

The right-hand side of Eq. (2.22) is equal to the Lagrangian of classical mechanics. For the special Hamilton-Jacobi Equation (2.17), which arises from the study of the characteristic surfaces of (2.1), it can be shown that $\dot{\varphi}(t) = 0$. Hence, the trajectories $\mathbf{x} = \mathbf{x}(t)$ in N-dimensional space lie on $\varphi(t, \mathbf{x}) = \text{const}$ surfaces, *i.e.*, on the characteristic surfaces. These trajectories are called the rays of the characteristic surfaces and the bicharacteristics of the original sytem of differential equations.

Any surface $\varphi(t, \mathbf{x}) = 0$ in spacetime, *e.g.*, the one shown in Fig. 2.1, can be interpreted as a wave front. Fig. 2.2 shows a two-dimensional front, which is equivalent to a surface $\varphi = 0$ in three-dimensional spacetime. Given the front location at time t, the motion can be described using the position vector $\mathbf{x} = \mathbf{X}(s, t)$, where s is a convenient parameter, say, the arclength of the front at the initial time t. The unit normal $\mathbf{n}$ is the one defined in (2.13). This description of a surface in spacetime is equivalent to the function $\varphi(t, \mathbf{x}) = 0$, but is sometimes more convenient. It shows how such a surface can be interpreted as a wave front, and in the case of characteristic surfaces, it makes more clear their interpretation as waves of discontinuities of the derivatives of the solution. The velocity of the front is defined by

$$\mathbf{V}(s, t) = \frac{\partial \mathbf{X}}{\partial t}(s, t) \,. \tag{2.23}$$

It is interesting to note that the motion of the front is specified by the normal front velocity $\mathbf{n} \cdot \mathbf{V}$ only. A tangential velocity component can be added without changing the location of the front at some later time $t + \Delta t$. See Fig. 2.2. This is equivalent to redefining the parameter s of the front at the initial time t.

For the case of characteristic fronts, there is a special local direction that can be used to assign a tangential velocity component. That is the direction of the characteristic rays of the surface $\varphi(t, \mathbf{x}) = 0$ corresponding to this front. The characteristic rays are given by the first of the canonical set of Equations (2.21). This is possible only because the characteristic rays lie on the surface $\varphi = 0$; *i.e.*, $\varphi\,[t, \mathbf{x}(t)] = 0$. It is important to note that from a computational point of view, generating the surface $\varphi = 0$ locally should be done using the most convenient set of curves. These do not always coincide with the characteristic rays.

The first of Eqs. (2.21) defines a vector field in spacetime given by

$$\dot{\mathbf{x}}(t) = \frac{\partial H}{\partial \mathbf{p}}(\mathbf{x}, \mathbf{p}) \,.$$

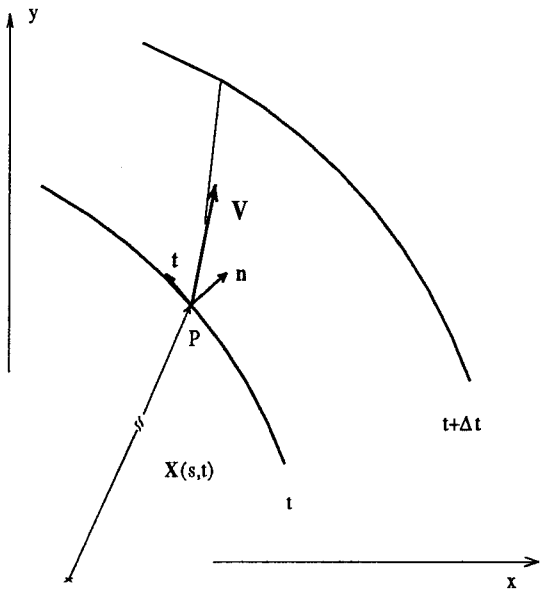

FIG.2.2 A two-dimensional front at times t and $t + \Delta t$. This front is described by the position vector $\mathbf{X}(s,t)$ and is equivalent to the surface $\varphi(t,\mathbf{x}) = 0$ in three-dimensional spacetime.

Actually, at every point in spacetime there is a family of vectors, since there is a dependence on the generalized momentum $\mathbf{p} = \nabla\varphi$. It is easy to visualize this in the special case of three-dimensional spacetime. It can be seen that for every possible orientation of the unit normal $\mathbf{n}$ in Fig. 2.2, which is related to $\mathbf{p}$ through (2.13), there is a different bicharacteristic direction. These directions form the so-called ray cone at every point. By integrating in time, the bicharacteristic curves emanating from a point form the ray conoid, which is essentially the conical solution of the characteristic Hamilton-Jacobi equation. See Fig. 2.3. The ray cone is tangent to the ray conoid.

Insofar as a characteristic surface can be interpreted as a wave, the characteristic conoid emanating from a point can be considered a wave front generated by a disturbance at this point. This characteristic conoid is tangent to all characteristic surfaces that pass through the given point. Moreover, the intersection of this conoid with the hyperplanes t = const determines the domain of dependence D and the domain of influence I of the solution at the given point. See Fig. 2.3.

One can prove the existence and uniqueness of solutions of the hyperbolic

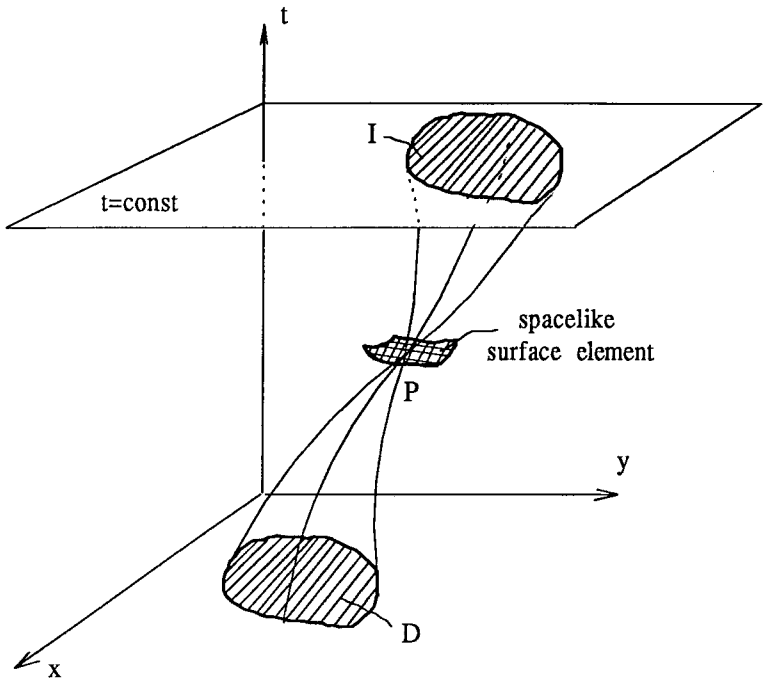

FIG.2.3 The ray conoid through the point P determines the domain of dependence D and the domain of influence I of the solution at P.

systems under consideration. These theorems show that given initial data on the hyperplane $t = 0$, the solution at the point P cannot depend on initial data outside the domain of dependence D. Furthermore, the solution at P cannot possibly influence the solution outside the forward-facing conoid, which cuts out the domain of influence I at some later time t. The details of the proof of these theorems can be found in Courant and Hilbert (1963); Friedrichs (1954); Friedrichs and Lax (1965), and Kato (1975).

The domains D and I in Fig. 2.3 are shown as simply connected. This is not necessarily the case for an arbitrary, hyperbolic system. One can define a space-like or time-like surface element passing through the point P with respect to the characteristic conoid. A surface element is space-like if its normal direction is inside the conoid, and time-like if it is not. The hyperplanes $t = \text{const}$, on which initial data are usually specified, are space-like. The Cauchy IVP has a unique solution provided initial data are specified on any space-like surface, not necessarily the hyperplanes $t = \text{const}$.

2.1.2 Application to Gas Dynamics

To illustrate these concepts consider the example of interest here, namely, the 3-D inviscid flow of a compressible fluid. The equations of motion can be written in the non-conservative form

$$\begin{aligned} \frac{\partial \rho}{\partial t} + \nabla\cdot(\rho\mathbf{u}) &= 0 \\ \frac{\partial \mathbf{u}}{\partial t} + \mathbf{u}\cdot\nabla\mathbf{u} + \frac{1}{\rho}\nabla p &= 0 \\ \frac{\partial p}{\partial t} + \mathbf{u}\cdot\nabla p + \rho a^2 \nabla\cdot\mathbf{u} &= 0\,, \end{aligned} \tag{2.24}$$

where ρ is the density, p is the pressure, $\mathbf{u} = (u, v, w)^{\mathrm{T}}$ is the velocity vector and a is the speed of sound. Eqs. (2.24) can be written in the general form

$$\frac{\partial U}{\partial t} + A_x \frac{\partial U}{\partial x} + A_y \frac{\partial U}{\partial y} + A_z \frac{\partial U}{\partial z} = 0\,, \tag{2.25}$$

where

$$\begin{aligned} U &= \begin{pmatrix} \rho \\ u \\ v \\ w \\ p \end{pmatrix}, \qquad A_x = \begin{pmatrix} u & \rho & 0 & 0 & 0 \\ 0 & u & 0 & 0 & 1/\rho \\ 0 & 0 & u & 0 & 0 \\ 0 & 0 & 0 & u & 0 \\ 0 & \rho a^2 & 0 & 0 & u \end{pmatrix}, \\ A_y &= \begin{pmatrix} v & 0 & \rho & 0 & 0 \\ 0 & v & 0 & 0 & 0 \\ 0 & 0 & v & 0 & 1/\rho \\ 0 & 0 & 0 & v & 0 \\ 0 & 0 & \rho a^2 & 0 & v \end{pmatrix}, \quad A_z = \begin{pmatrix} w & 0 & 0 & \rho & 0 \\ 0 & w & 0 & 0 & 0 \\ 0 & 0 & w & 0 & 0 \\ 0 & 0 & 0 & w & 1/\rho \\ 0 & 0 & 0 & \rho a^2 & w \end{pmatrix}. \end{aligned} \tag{2.26}$$

There are five unknown functions; *i.e.*, $M = 5$, defined on 4-dimensional spacetime, *i.e.*, $N = 3$. One can easily specialize the following results to the case $N = 2$, or $N = 1$. It is a straightforward calculation to substitute (2.26) in Eq. (2.10) to find

$$Q = \left(\frac{\partial \varphi}{\partial t} + \mathbf{u}\cdot\nabla\varphi\right)^3 \left(\frac{\partial \varphi}{\partial t} + \mathbf{u}\cdot\nabla\varphi + a\,|\nabla\varphi|\right)\left(\frac{\partial \varphi}{\partial t} + \mathbf{u}\cdot\nabla\varphi - a\,|\nabla\varphi|\right) = 0\,. \tag{2.27}$$

The convective characteristic manifold is defined by the Hamilton-Jacobi equation

$$\frac{\partial \varphi}{\partial t} + \mathbf{u}\cdot\nabla\varphi = 0\,. \tag{2.28}$$

It has a 3-fold degeneracy. The acoustic characteristic manifold is defined by the equations

$$\frac{\partial \varphi}{\partial t} + \mathbf{u}\cdot\nabla\varphi \pm a\,|\nabla\varphi| \;=\; 0\,. \tag{2.29}$$

Let's examine the acoustic manifold given by (2.29) with just the plus sign. Referring to the general Hamilton-Jacobi notation, the Hamiltonian is seen to be

$$H(\mathbf{x},\mathbf{p}) \;=\; \mathbf{u}\cdot\mathbf{p} + a\,|\mathbf{p}|\;, \tag{2.30}$$

where $\mathbf{p} = \nabla\varphi$. From the canonical ODEs (2.21), it is seen that the rays of the acoustic characteristic manifold are given by

$$\dot{\mathbf{x}}(t) \;=\; \frac{\partial H}{\partial \mathbf{p}} \;=\; \mathbf{u} + a\frac{\mathbf{p}}{|\mathbf{p}|}\;, \tag{2.31}$$

or by (2.13),

$$\dot{\mathbf{x}}(t) \;=\; \mathbf{u} + a\mathbf{n}\,. \tag{2.32}$$

These rays are the bicharacteristics for the equations of gas dynamics. They are the generators of the ray conoid. See Fig. 2.3. The eigenvalues λ_m , $m = 1,\ldots,5$, of the matrix $\mathbf{n}\cdot\mathbf{A}$, are given by the second expression in (2.13); *i.e.*,

$$\lambda \;=\; -\frac{\partial \varphi}{\partial t}\Big/\,|\nabla\varphi| \;=\; H\,(\mathbf{x},\mathbf{p})\,/\,|\mathbf{p}|\;. \tag{2.33}$$

For the particular example of the acoustic manifold, the Hamiltonian is given by (2.30) and, hence the corresponding eigenvalue is

$$\lambda \;=\; (\mathbf{u}\cdot\mathbf{p} + a|\mathbf{p}|)\,/|\mathbf{p}| \;=\; \mathbf{u}\cdot\mathbf{n} + a\,. \tag{2.34}$$

It is interesting that the eigenvalue λ coincides with the normal velocity component of the characteristic front. See Fig. 2.2. It is also easy to show that along the bicharacteristics,

$$\dot{\varphi}(t) \;=\; \dot{\mathbf{x}}(t)\cdot\mathbf{p}(t) - H\,[\mathbf{x}(t),\mathbf{p}(t)] \;=\; \mathbf{u}\cdot\mathbf{p} + a|\mathbf{p}| - H \;=\; 0\,. \tag{2.35}$$

Therefore, the bicharacteristics lie on the characteristic surfaces, as expected. Similarly, one finds that the rays of the convective manifold (2.28) are the flow streamlines

$$\dot{\mathbf{x}}(t) \;=\; \mathbf{u}\,. \tag{2.36}$$

2.2 Riemann Invariant Manifolds

The differential equations that hold on the characteristic manifolds will be derived for the Euler equations of gas dynamics. It will be shown that the equations along characteristic directions are greatly simplified, only in the special case of one-dimensional flow. In this case, it is possible to introduce the well known Riemann invariants and the theory of characteristics can be used for computational purposes. For multidimensional flows, there appears to be no advantage in using the characteristic surfaces to integrate the equations. It will be shown that other spacetime manifolds exist that provide the same computational advantage as the characteristics in 1-D flow. These manifolds are referred to as Riemann Invariant Manifolds.

A straightforward calculation yields the left and right eigenvectors of the matrix $\mathbf{n}\cdot\mathbf{A}$ for the example of gas dynamics. The differential equation that holds along a characteristic ray can be found by multiplying from the left by the appropriate eigenvector; *i.e.*,

$$\langle\, l_k, \frac{\partial U}{\partial t}\,\rangle + \langle\, l_k, A_m \frac{\partial U}{\partial x_m}\,\rangle \;=\; 0\,, \qquad k = 1, \ldots, M\,, \tag{2.37}$$

where $\langle\cdot,\cdot\rangle$ is the usual inner product in $\Re^M$. By multiplying from the left with the left eigenvectors l_k corresponding to the acoustic manifold (2.29) of the Euler equations, one finds the differential equation, which holds along the bicharacteristic, $\dot{\mathbf{x}}(t) = \mathbf{u} + a\mathbf{n}$,

$$\begin{aligned}\left[\frac{\partial p}{\partial t} + (\mathbf{u}+a\mathbf{n})\cdot\nabla p\right] + \rho a\mathbf{n}\cdot\left[\frac{\partial \mathbf{u}}{\partial t} + (\mathbf{u}+a\mathbf{n})\cdot\nabla\mathbf{u}\right] \\ + \rho a^2\left[\nabla\cdot\mathbf{u} - \mathbf{n}\cdot(\nabla\mathbf{u})\,\mathbf{n}\right] \;=\; 0\,.\end{aligned} \tag{2.38}$$

Using index notation and dividing through by ρa,

$$\begin{aligned}\frac{1}{\rho a}\left[\frac{\partial p}{\partial t} + (u_j + a n_j)\frac{\partial p}{\partial x_j}\right] + n_i\left[\frac{\partial u_i}{\partial t} + (u_j + a n_j)\,\frac{\partial u_i}{\partial x_j}\right] \\ + a\,(\delta_{ij} - n_i n_j)\left(\frac{\partial u_i}{\partial x_j}\right) \;=\; 0\,,\end{aligned} \tag{2.39}$$

where δ_{ij} is the Kronecker delta. Since the tensor $\delta_{ij} - n_i n_j$ is symmetric,

$$G_n \;\equiv\; (\delta_{ij} - n_i n_j)\left(\frac{\partial u_i}{\partial x_j}\right) \;=\; (\delta_{ij} - n_i n_j)\,S_{ij}\,, \tag{2.40}$$

where

$$S_{ij} \equiv \frac{1}{2}\left(\frac{\partial u_i}{\partial x_j} + \frac{\partial u_j}{\partial x_i}\right)$$

is the rate of strain tensor. Only the symmetric part of the velocity-gradient tensor enters in the term G_n.

The significance of Eq. (2.38) can be seen by deriving it in a way that is not related to the concept of characteristic manifolds. Consider an arbitrary, spatial, unit vector $\mathbf{n}$. The last two equations in (2.24) can be combined to give Eq. (2.38). The momentum equation can be written as follows, by taking its inner product with the vector $\rho a\mathbf{n}$ and adding and subtracting the term $\rho a^2 \mathbf{n}\cdot(\nabla \mathbf{u})\,\mathbf{n}$; *i.e.*,

$$\frac{\partial \mathbf{u}}{\partial t} + \mathbf{u}\cdot\nabla\mathbf{u} + \frac{1}{\rho}\nabla p \;=\; 0$$

$$\Rightarrow \qquad \rho a\mathbf{n}\cdot\left[\frac{\partial \mathbf{u}}{\partial t} + (\mathbf{u} + a\mathbf{n})\cdot\nabla\mathbf{u}\right] - \rho a^2 \mathbf{n}\cdot(\nabla\mathbf{u})\,\mathbf{n} + a\mathbf{n}\cdot\nabla p \;=\; 0\,.$$

The energy equation can be written

$$\frac{\partial p}{\partial t} + \mathbf{u}\cdot\nabla p + \rho a^2 \nabla\cdot\mathbf{u} \;=\; 0$$

$$\Rightarrow \qquad \frac{\partial p}{\partial t} + (\mathbf{u} + a\mathbf{n})\cdot\nabla p + \rho a^2\nabla\cdot\mathbf{u} - a\mathbf{n}\cdot\nabla p \;=\; 0.$$

Adding the two equations gives Eq. (2.38).

It is clear from this derivation that this equation holds for an arbitrary vector $\mathbf{n}$. It gives the relation between velocity changes and pressure changes along the direction $\dot{\mathbf{x}} = \mathbf{u} + a\mathbf{n}$. It is the previous discussion of characteristic surfaces, which allows us to identify these directions as the generating rays of the acoustic characteristic manifold, *i.e.*, the bicharacteristics. It is also important to notice that it is really a family of equations. By fixing $\mathbf{n}$ to be a unit vector, it is easy to see that Eq. (2.38) or (2.39) is actually an $(N-1)$-parameter family of equations. Indeed, for two-dimensional flow ($N = 2$), the vector $\mathbf{n}$ is constrained to the unit circle and for three-dimensional flow it is constrained to the surface of the unit sphere. This is important because, although they are all dependent equations and consistent with the original system (2.24), a particular choice of $\mathbf{n}$ may be optimal for computational purposes.

Consider the special case of one-dimensional flow ($N = 1$) in the x-direction. The characteristic surfaces are now characteristic curves in two-dimensional space-time (t, x), given by

$$C_\pm \; : \; \frac{dx}{dt} \; = \; u \pm a \, . \tag{2.41}$$

The only possible choices for the unit vector are $\mathbf{n} = \pm \hat{e}_x$, where $\hat{e}_x$ is the unit vector in the direction of the flow. The family of Equations (2.39) consists of just the two equations in the direction of the two characteristics,

$$\frac{1}{\rho a} \left[\frac{\partial p}{\partial t} + (u \pm a) \frac{\partial p}{\partial x} \right] \pm \left[\frac{\partial u}{\partial t} + (u \pm a) \frac{\partial u}{\partial x} \right] \; = \; 0 \, . \tag{2.42}$$

These two equations are written in the more conventional form as

$$\frac{1}{\rho a} \frac{dp}{dt} \pm \frac{du}{dt} \; = \; 0 \, , \tag{2.43}$$

where the time derivatives are derivatives along the appropriate characteristic directions. Eqs. (2.43) form the basis for the well-known theory of characteristics in 1-D gas dynamics. Moreover, when supplemented with the jump conditions, they form the basis for the solution of the 1-D Riemann problem. This is important from a computational perspective, since most numerical codes use this one-dimensional problem as the basis for multidimensional computations as well.

If there are no entropy gradients, then (2.43) can be further simplified. Define the thermodynamic state variable W by

$$W \; \equiv \; \int_{ds=0} \frac{dp}{\rho a} \, , \tag{2.44}$$

where the integral is performed in thermodynamic state space along a path of constant entropy s. For a perfect gas this function is simply

$$W \; = \; \frac{2a}{\gamma - 1} \, , \tag{2.45}$$

where γ is the specific heat ratio. When there are no entropy gradients in the flow, (2.43) can be integrated to give

$$\frac{d}{dt} (W \pm u) \; = \; 0 \quad \Rightarrow R_\pm \; \equiv \; W \pm u \; = \; \text{const} \, . \tag{2.46}$$

The variables $R_\pm$ are the well-known Riemann invariants. They remain constant along the characteristic directions. It is this simple relation that makes the method of characteristics a useful computational tool.

Returning to the multidimensional case and motivated by the one-dimensional results, one can also simplify Eq. (2.38) for the case of no entropy gradients by again introducing the thermodynamic variable W given by (2.44). Then,

$$\left[\frac{\partial W}{\partial t} + (\mathbf{u} + a\mathbf{n})\cdot\nabla W\right] + \left[\frac{\partial(\mathbf{u}\cdot\mathbf{n})}{\partial t} + (\mathbf{u} + a\mathbf{n})\,\nabla(\mathbf{u}\cdot\mathbf{n})\right] + a\left[\nabla\cdot\mathbf{u} - \mathbf{n}\cdot(\nabla\mathbf{u})\,\mathbf{n}\right] = 0\,. \tag{2.47}$$

The vector $\mathbf{n}$ is assumed to be constant. Motivated by the one-dimensional case, one is led to define the family of Riemann Invariants

$$R_n \equiv W + \mathbf{u}\cdot\mathbf{n}\,, \tag{2.48}$$

which are analogous to the Riemann invariants $R_\pm$ in 1-D flow. Eq. (2.47) can now be written

$$\frac{\partial R_n}{\partial t} + (\mathbf{u} + a\mathbf{n})\cdot\nabla R_n + a\left[\nabla\cdot\mathbf{u} - \mathbf{n}\cdot(\nabla\mathbf{u})\,\mathbf{n}\right] = 0\,, \tag{2.49a}$$

or

$$\frac{\partial R_n}{\partial t} + (\mathbf{u} + a\mathbf{n})\cdot\nabla R_n + aG_n = 0\,. \tag{2.49b}$$

Unfortunately, the presence of the term $aG_n = a\,(\delta_{ij} - n_i n_j)\,S_{ij}$ in Eq. (2.49) acts as a source term and complicates matters in multidimensional flows.

If a unit vector $\mathbf{n}$ exists, such that $G_n = 0$, then along the direction $\dot{\mathbf{x}} = \mathbf{u} + a\mathbf{n}$, Eq. (2.49) is integrable and $R_n = \text{const}$. By examining the form of G_n, one can see that it is not always possible to find such a direction $\mathbf{n}$. G_n is the two-dimensional divergence of the velocity field in the plane normal to the vector $\mathbf{n}$. For the case of 2-D flow, *i.e.*, $N = 2$, it can be shown that a direction $\mathbf{n}$, such that $G_n = 0$, can be found only when the eigenvalues of the rate of strain tensor S are such that

$$\lambda_{\min}\lambda_{\max} \leq 0\,. \tag{2.50}$$

This condition is not always satisfied in an arbitrary flow. The generalization of the simple, one-dimensional results does not appear to be straightforward, and this has thwarted many efforts to extend the method of characteristics to higher dimensions. There appears to be no advantage whatsoever in integrating the equations of motion along the bicharacteristic directions, which are the multidimensional extensions of the characteristics in 1-D. The characteristic surfaces are significant for the reasons explained in the previous discussion and primarily for the role they play

in proving the existence and uniqueness of solutions. The existence and uniqueness theorems are closely related to the concepts of domain of dependence and domain of influence. Integrating along paths on the characteristic surfaces gives no advantage over integrating along, say, $\mathbf{x}$ = const paths, which is what is usually done on a computer.

It would be very useful to know along which curves in spacetime it is possible to have R_n = const. The equations of motion would be integrable along these paths in a way completely analogous to the 1-D case. Obviously, these paths are not the bicharacteristics. The paths of interest will have to lie on the surfaces $R_n(t, \mathbf{x})$ = const.

It is easy to see what paths lie on the surfaces R_n = const in spacetime by adding and subtracting the following term in Eq. (2.49),

$$\mathbf{v}\cdot\nabla R_n \ , \tag{2.51}$$

where $\mathbf{v}$ is a velocity. Eq. (2.49) is now written

$$\frac{\partial R_n}{\partial t} + (\mathbf{u} + a\mathbf{n} + \mathbf{v})\cdot\nabla R_n + aG_n - \mathbf{v}\cdot\nabla R_n \ = \ 0 \ . \tag{2.52}$$

If the velocity $\mathbf{v}$ is chosen so that

$$\mathbf{v}\cdot\nabla R_n \ = \ aG_n \ = \ a\left[\nabla\cdot\mathbf{u} - \mathbf{n}\cdot(\nabla\mathbf{u})\,\mathbf{n}\right] \ , \tag{2.53}$$

then

$$\frac{\partial R_n}{\partial t} + (\mathbf{u} + a\mathbf{n} + \mathbf{v})\cdot\nabla R_n \ = \ 0 \ . \tag{2.54}$$

Eq. (2.54) says that along the paths

$$\dot{\mathbf{x}}(t) = \mathbf{V} \ \equiv \ \mathbf{u} + a\mathbf{n} + \mathbf{v} \ , \tag{2.55}$$

the Riemann Invariant R_n is constant. Eq. (2.53) is simply a compatibility condition, which must be satisfied by the integral curve of (2.55), in order for it to lie on the surface R_n = const. The velocity $\mathbf{v}$ depends on the local, spatial gradients of the flow, as can be seen from Eq. (2.53). Given a point in the flow where ∇R_n and G_n have a specified value, this relation is linear in the velocity components of $\mathbf{v}$. The reason is that there is an infinity of curves passing through this given point, which lie on the surface R_n = const. See Fig. 2.4. All possible choices of $\mathbf{v}$ correspond to all possible directions of motion on this surface. Moreover, it is well known from differential geometry that there are an infinity of curves for every such direction. In what follows, some interesting and useful choices of directions will be examined.

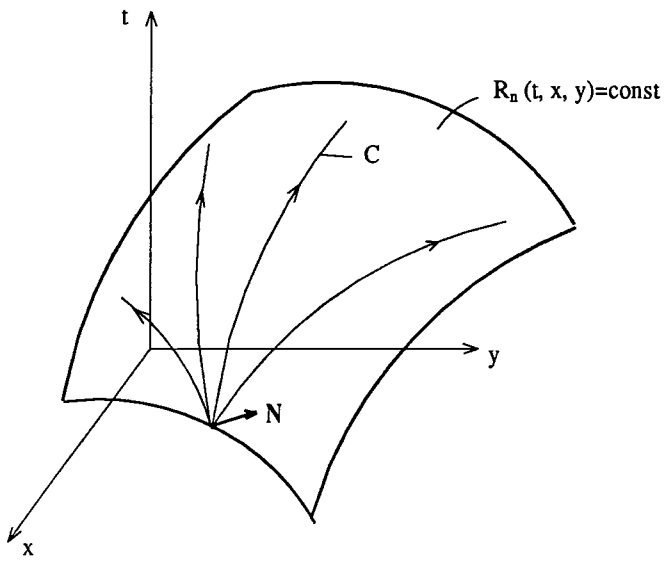

FIG.2.4 The surface $R_n\,(t, \mathbf{x}) = \text{const}$ in three-dimensional spacetime. There are an infinity of curves passing through a given point, which lie on this surface.

The assumption of zero entropy gradients allowed the introduction of the Riemann Invariants R_n, which simplified the analysis by making the equations integrable. Let's abandon this assumption and repeat the previous analysis. Eq. (2.38) will be the starting point:

$$\left[\frac{\partial p}{\partial t} + (\mathbf{u} + a\mathbf{n})\cdot\nabla p\right] + \rho a\mathbf{n}\cdot\left[\frac{\partial \mathbf{u}}{\partial t} + (\mathbf{u} + a\mathbf{n})\cdot\nabla\mathbf{u}\right] + \rho a^2\left[\nabla\cdot\mathbf{u} - \mathbf{n}\cdot(\nabla\mathbf{u})\,\mathbf{n}\right] = 0\,.$$

By adding and subtracting the term

$$\mathbf{v}\cdot[\nabla p + \rho a\nabla(\mathbf{u}\cdot\mathbf{n})] = \mathbf{v}\cdot\left[\nabla p + \rho a\,(\nabla\mathbf{u})^{\mathrm{T}}\mathbf{n}\right]\,, \tag{2.56}$$

and for a $\mathbf{v}$ chosen so that

$$\mathbf{v}\cdot[\nabla p + \rho a\nabla(\mathbf{u}\cdot\mathbf{n})] = \rho a^2\left[\nabla\cdot\mathbf{u} - \mathbf{n}\cdot(\nabla\mathbf{u})\,\mathbf{n}\right]\,, \tag{2.57}$$

one finds

$$\left[\frac{\partial p}{\partial t} + (\mathbf{u} + a\mathbf{n} + \mathbf{v})\cdot\nabla p\right] + \rho a\left[\frac{\partial(\mathbf{u}\cdot\mathbf{n})}{\partial t} + (\mathbf{u} + a\mathbf{n} + \mathbf{v})\cdot\nabla(\mathbf{u}\cdot\mathbf{n})\right] = 0\,. \tag{2.58}$$

Again $\mathbf{n}$ is assumed to be a constant vector. Eq. (2.58) can be written in a more conventional form as

$$\frac{1}{\rho a}\frac{dp}{dt} + \frac{du_n}{dt} = 0\,, \tag{2.59}$$

along the paths

$$\dot{\mathbf{x}}(t) \;=\; \mathbf{V} \;\equiv\; \mathbf{u} + a\mathbf{n} + \mathbf{v}\,, \tag{2.60}$$

where $u_n \equiv \mathbf{u}\cdot\mathbf{n}$, *i.e.*, the velocity component in the direction of the fixed $\mathbf{n}$ vector. Eq. (2.59) is of the same form as the first of Eqs. (2.43), which holds along the C_+ characteristic in the 1-D case. The previous discussion for the R_n = const surfaces holds for these manifolds as well, but their interpretation is different and more general. The solutions at any two points on such a manifold, connected by a trajectory given by (2.60), are related in exactly the same way that solutions are related along characteristics in the 1-D case. Knowledge of the integral curves of the vector field (2.60) allows one to use the simple results of the one-dimensional theory in multidimensional flows. In what follows, the notation R_n = const will be used for these manifolds even when entropy gradients are present and the Riemann Invariants $R_n = W + \mathbf{u}\cdot\mathbf{n}$ cannot be used.

There is a computational advantage of knowing the integral curves of these vector fields. The solution of the gas-dynamic equations at points along these curves are related in a certain, simple way. It is interesting to see what the geometry of these manifolds is, in relation to the characteristic manifolds. A few ways of describing their geometry are presented in what follows.

One way of visualizing the relative position of the characteristic manifolds and the Riemann Invariant Manifolds is by examining the motion of the equivalent $(N-1)$-dimensional fronts. Recall that any surface $\varphi(t,\mathbf{x}) = 0$ in spacetime, is equivalent to a wave front. For simplicity consider the case of a two-dimensional flow; *i.e.*, $N = 2$. Fig. 2.5, shows the local geometry and motion of the wave front R_n = const for a finite time Δt. The local unit normal of this front is

$$\mathbf{N} \;=\; \frac{\nabla p + \rho a\,(\nabla\mathbf{u})^{\mathrm{T}}\mathbf{n}}{\left|\nabla p + \rho a\,(\nabla\mathbf{u})^{\mathrm{T}}\mathbf{n}\right|}\,. \tag{2.61}$$

For the case of zero-entropy gradients, this is seen to be

$$\mathbf{N} \;=\; \frac{\nabla R_n}{|\nabla R_n|}\,. \tag{2.62}$$

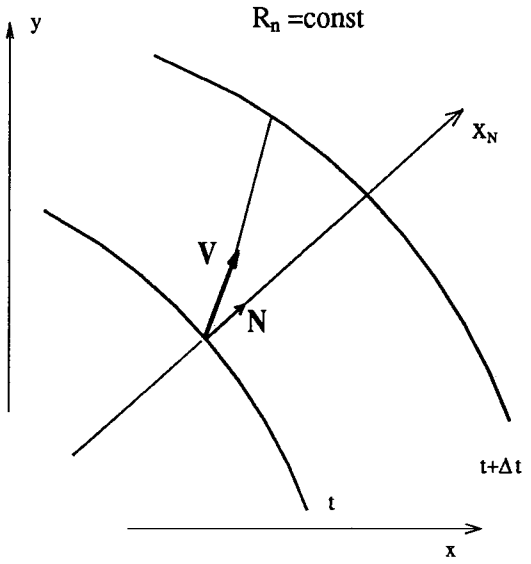

FIG.2.5 Local geometry of the Riemann Invariant front R_n = const. The outer normal is **N** and its velocity is **V**.

At this point, it is important to note that the unit normal **n** serves as a label for the particular manifold. It determines the fluid velocity component that is used for the equivalent, one-dimensional problem. The vector **n** should be considered as the parameter of the one-parameter family of Riemann Invariant wave fronts. From Eq. (2.61), it is apparent that **N** depends on **n**. Moreover, the mapping is not bijective; *i.e.*, it is not always possible to find a wave front R_n = const for an arbitrary **N**. The spatial gradients of the flow determine a range of allowed propagation directions **N** for these fronts.

It is also useful to define the vector $\mathbf{n}^-$, which determines the front propagating in the $-\mathbf{N}$ direction; *i.e.*,

$$-\mathbf{N} = \frac{\nabla p + \rho a \left(\nabla \mathbf{u}\right)^{\mathrm{T}} \mathbf{n}^-}{\left|\nabla p + \rho a \left(\nabla \mathbf{u}\right)^{\mathrm{T}} \mathbf{n}^-\right|}, \tag{2.63}$$

if it exists. One can also define $\mathbf{N}^-$ by

$$\mathbf{N}^- = \frac{\nabla p - \rho a \left(\nabla \mathbf{u}\right)^{\mathrm{T}} \mathbf{n}}{\left|\nabla p - \rho a \left(\nabla \mathbf{u}\right)^{\mathrm{T}} \mathbf{n}\right|}. \tag{2.64}$$

It is important to keep in mind that in general, $\mathbf{n}^- \neq -\mathbf{n}$ and $\mathbf{N}^- \neq -\mathbf{N}$.

The velocity of the front $R_n = \text{const}$ is given by

$$\mathbf{V} = \mathbf{u} + a\mathbf{n} + \mathbf{v} \,, \tag{2.65}$$

where $\mathbf{v}$ has to satisfy Eq. (2.57); *i.e.*,

$$\mathbf{v}\cdot[\nabla p + \rho a \nabla(\mathbf{u}\cdot\mathbf{n})] \;=\; \rho a^2 \left[\nabla\cdot\mathbf{u} - \mathbf{n}\cdot(\nabla\mathbf{u})\,\mathbf{n}\right] \,. \tag{2.66}$$

The geometry of the front at time $t + \Delta t$ is completely determined by the normal front velocity. One can add an arbitrary, tangential velocity component without changing the front geometry. This freedom is seen in choosing the velocity component $\mathbf{v}$, which need only satisfy Eq. (2.66). This equation represents a straight line in velocity space. It is possible to find the front velocity that corresponds to minimum $|\mathbf{v}|$. This is the case when $\mathbf{v} \,/\!/\, \mathbf{N}$. The corresponding front velocity is

$$\mathbf{V}_H \;=\; \mathbf{u} + a\mathbf{n} + \frac{\rho a^2 \left[\nabla\cdot\mathbf{u} - \mathbf{n}\cdot(\nabla\mathbf{u})\,\mathbf{n}\right]}{\left|\nabla p + \rho a\,(\nabla\mathbf{u})^{\mathrm{T}}\mathbf{n}\right|}\mathbf{N} \,. \tag{2.67}$$

The integral curves of this vector field are the curves on the manifold $R_n = \text{const}$, which are closest to the bicharacteristics $\dot{\mathbf{x}}(t) = \mathbf{u} + a\mathbf{n}$. The normal front velocity can be found by combining Eqs. (2.61), (2.65) and (2.66),

$$\mathbf{V}_N \;\equiv\; (\mathbf{V}\cdot\mathbf{N})\,\mathbf{N} \;=\; (\mathbf{u}\cdot\mathbf{N})\,\mathbf{N} + \mu_n a \mathbf{N} \,, \tag{2.68}$$

where μ_n is a dimensionless number defined by

$$\mu_n \;\equiv\; \frac{\mathbf{n}\cdot\nabla p + \rho a \nabla\cdot\mathbf{u}}{\left|\nabla p + \rho a\,(\nabla\mathbf{u})^{\mathrm{T}}\mathbf{n}\right|} \,, \tag{2.69}$$

and plays the role of an algebraic Mach number. The front velocity can also be chosen so that the integral curve of this vector field is as close to the fluid streamline as possible. This is done by minimizing $|a\mathbf{n} + \mathbf{v}|$ in Eq. (2.65). It is possible to show that this is minimized when $(a\mathbf{n} + \mathbf{v}) \,/\!/\, \mathbf{N}$. The front velocity in this case is given by

$$\mathbf{V}_S \;=\; \mathbf{u} + \mu_n a \mathbf{N} \,. \tag{2.70}$$

This particular choice of front velocity is very useful because it resembles the bicharacteristic velocities that generate the characteristic manifolds. It is clear that the parameter μ_n is an indication of how much the manifold $R_n = \text{const}$ deviates from the local characteristic surfaces. In Fig. 2.6, a normal slice of these surfaces is shown. A normal slice is the intersection of the surface with the plane defined by the direction $\mathbf{N}$ and the time axis. The surface $R_n = \text{const}$ is characteristic when $\mu_n = \pm 1$. Furthermore, it is time-like when $-1 < \mu_n < 1$ and space-like when $|\mu_n| > 1$. The following useful relation can be found by combining Eqs. (2.61),(2.66) and (2.69),

$$\mu_n = \mathbf{n}\cdot\mathbf{N} + \frac{\rho a G_n}{\left|\nabla p + \rho a \left(\nabla \mathbf{u}\right)^{\mathrm{T}} \mathbf{n}\right|} \quad . \tag{2.71}$$

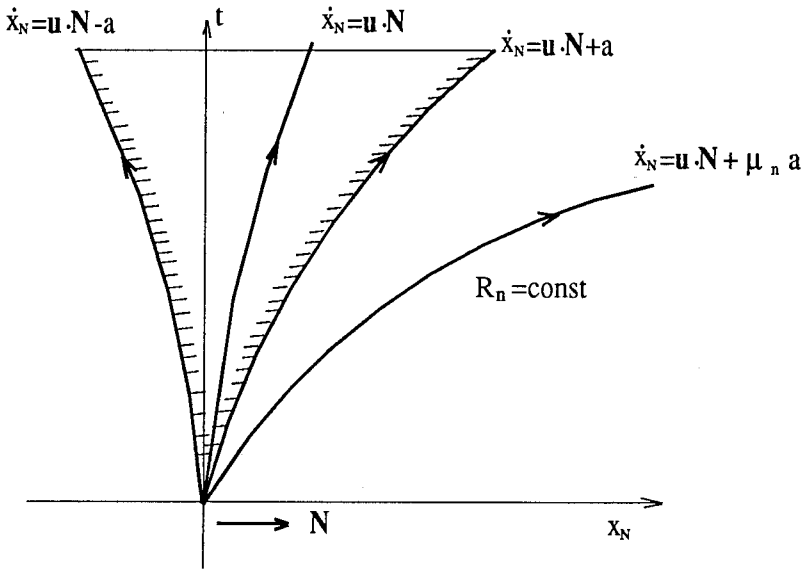

FIG.2.6 Normal slice of the Riemann Invariant Manifold $R_n = \text{const}$ and the characteristic manifolds. Their relative position is determined by the parameter μ_n. When $|\mu_n| \leq 1$, the surface element is time-like. This is an example of a space-like surface.

Most of the geometrical information of the Riemann Invariant Manifolds is contained in the two quantities $\mathbf{N}$ and μ_n. They show the allowed direction of propagation of the corresponding fronts and how much they deviate from the characteristic surfaces. They both depend on the unit vector $\mathbf{n}$, *i.e.*, on the particular

choice of Riemann Invariant Manifold. Using the definition of μ_n (2.69) and the equations of motion (2.24), one can show that

$$\mu_n \equiv \frac{\mathbf{n}\cdot\nabla p + \rho a \nabla\cdot\mathbf{u}}{\left|\nabla p + \rho a\,(\nabla\mathbf{u})^{\mathrm{T}}\mathbf{n}\right|} = \frac{\mathbf{n}\cdot\nabla p - \dfrac{1}{a}\dfrac{Dp}{Dt}}{\left|\nabla p + \rho a\,(\nabla\mathbf{u})^{\mathrm{T}}\mathbf{n}\right|}\,, \tag{2.72}$$

where D/Dt denotes the Lagrangian derivative. It is interesting that the magnitude of μ_n depends directly on the difference between the pressure gradient in the $\mathbf{n}$ direction and the pressure change along the fluid-particle streamline. For the case of zero-entropy gradient, it is easy to show that

$$\mu_n = \frac{\mathbf{n}\cdot\nabla W + \nabla\cdot\mathbf{u}}{\left|\nabla W + (\nabla\mathbf{u})^{\mathrm{T}}\mathbf{n}\right|} = -\frac{1}{a\,|\nabla R_n|}\frac{DR_n}{Dt}\,. \tag{2.73}$$

The starting point of this discussion has been Eq. (2.49); *i.e.*,

$$\frac{\partial R_n}{\partial t} + (\mathbf{u} + a\mathbf{n})\cdot\nabla R_n + a\left[\nabla\cdot\mathbf{u} - \mathbf{n}\cdot(\nabla\mathbf{u})\,\mathbf{n}\right] = 0\,. \tag{2.74}$$

This equation is a first-order differential equation for the function $R_n = R_n(t,\mathbf{x})$ of the form (2.18). It resembles a Hamilton-Jacobi equation similar to the one satisfied by the characteristic manifolds. The Hamiltonian in this case is seen to be

$$H(\mathbf{x},\mathbf{p}) = (\mathbf{u} + a\mathbf{n})\cdot\mathbf{p} + aG_n\,, \tag{2.75}$$

where

$$\mathbf{p} \equiv \nabla R_n\,. \tag{2.76}$$

The only complication here is that this equation is not independent of the others in the system. Nevertheless, conclusions can be drawn about the geometry of the integral manifold in $(N+2)$-dimensional space $(t,\mathbf{x},R_n)$ or more importantly, about the geometry of the slices $R_n = \text{const}$ in spacetime $(t,\mathbf{x})$, using the insight gained from the study of 1$^{\text{st}}$ order PDEs and in particular, the Hamilton-Jacobi equation. If one applies the results obtained for the Hamilton-Jacobi equation to Eq. (2.74), formally, then Eqs. (2.21) and (2.22) give

$$\begin{aligned}
\dot{\mathbf{x}}(t) &= \frac{\partial H}{\partial \mathbf{p}} = \mathbf{u} + a\mathbf{n}\,,\\
\dot{\mathbf{p}}(t) &= -\frac{\partial H}{\partial \mathbf{x}}\,,\\
\dot{R}_n(t) &= -aG_n = -a\left[\nabla\cdot\mathbf{u} - \mathbf{n}\cdot(\nabla\mathbf{u})\,\mathbf{n}\right]\,.
\end{aligned} \tag{2.77}$$

The integral manifold of (2.74) can be conveniently visualized, locally, as a network of surfaces R_n = const. See Fig. 2.7. Eqs. (2.77) describe how R_n changes along the bicharacteristic directions $\dot{\mathbf{x}}(t) = \mathbf{u} + a\mathbf{n}$. The bicharacteristic curves do not lie on the surfaces R_n = const. Recall that the vector $\mathbf{n}$ is a constant, which labels the particular network of Riemann Invariant Manifolds. If it is possible to find a vector $\mathbf{n}$ such that $G_n = 0$, then the bicharacteristics lie on the surfaces R_n = const. It is important to keep in mind that the integral curves of the vector field $\dot{\mathbf{x}}(t) = \mathbf{u} + a\mathbf{n}$, with $\mathbf{n}$ a constant vector, are not the bicharacteristics. They are very close to the bicharacteristics for a short time. In order to remain on a bicharacteristic, the vector $\mathbf{n}$ must change according to Eqs. (2.21).

In general, integrating Eqs. (2.77) to find the solution at a point P (see Fig. 2.7), provides no computational advantage. It is apparent from the figure that there are an infinity of paths C on the surfaces R_n = const that can be used instead. The problem of finding the solution at P reduces to computing the geometry of the curves accurately, by integrating

$$\dot{\mathbf{x}}(t) = \mathbf{V} \;=\; \mathbf{u} + a\mathbf{n} + \mathbf{v}\;. \tag{2.78}$$

All such paths C are not equivalent numerically. The local curvature of these surfaces is also an important consideration in choosing the most convenient path for numerical integration. One can try to minimize the numerical error by varying the direction of approach to the point P. It is also possible to estimate the curvature of a particular path and to use this information to achieve higher-order accuracy in the integration of (2.78). Moreover, by varying the vector $\mathbf{n}$, *i.e.*, varying the network of Riemann Invariant Manifolds, it is possible to optimize the scheme even further. The algebraic parameter μ_n shows whether the surface R_n = const is space-like or time-like. Surfaces with $\mu_n >> 1$ should be avoided, because the timestep required to integrate Eq. (2.78) accurately would be too restrictive.

It is possible to find the projection of an arbitrary path $\dot{\mathbf{x}}(t) = \mathbf{W}$ on the surface R_n = const. The projection is defined to be the path $\dot{\mathbf{x}}(t) = \mathbf{V}_{\mathrm{w}}$ on R_n = const, such that $|\mathbf{v}^{\perp}|$ is minimum, where

$$\mathbf{v}^{\perp} \;\equiv\; \mathbf{V}_{\mathrm{w}} - \mathbf{W}\;. \tag{2.79}$$

Since the projection is on the Riemann Invariant Manifold,

$$\mathbf{V}_{\mathrm{w}} \;=\; \mathbf{u} + a\mathbf{n} + \mathbf{v}_{\mathrm{w}}\;, \tag{2.80}$$

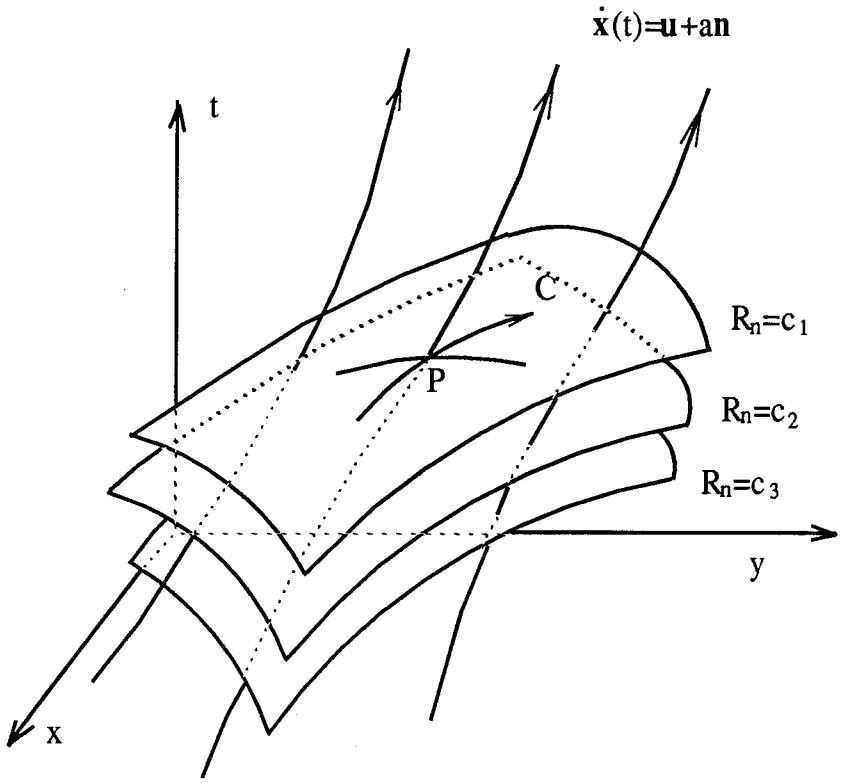

FIG.2.7 The integral manifold of Eq. (2.74) is shown as a network of Riemann Invariant Manifolds R_n = const in three-dimensional spacetime. It is more convenient to integrate along paths C on these surfaces rather than along the bicharacteristic paths $\dot{\mathbf{x}}(t) = \mathbf{u} + a\mathbf{n}$.

where $\mathbf{v}_w$ satisfies the compatibility condition (2.66). It is straightforward to show that

$$\mathbf{v}^{\perp}\cdot\mathbf{N} \;=\; \mathbf{u}\cdot\mathbf{N} + \mu_n a - \mathbf{N}\cdot\mathbf{W}\;. \tag{2.81}$$

It is seen from Eq. (2.81) that $|\mathbf{v}^{\perp}|$ is minimum when $\mathbf{v}^{\perp}$ // $\mathbf{N}$. The projection is then

$$\mathbf{V}_w \;=\; (\mathbf{u}\cdot\mathbf{N} + \mu_n a)\,\mathbf{N} + \mathbf{W} - (\mathbf{N}\cdot\mathbf{W})\,\mathbf{N}\;. \tag{2.82}$$

Now, one can find the projection of an arbitrary bicharacteristic direction $\mathbf{u} + a\hat{\mathbf{n}}$, where $\hat{\mathbf{n}}$ is a unit vector. Substituting $\mathbf{W} = \mathbf{u} + a\hat{\mathbf{n}}$ in Eq. (2.82) gives the projection of the bicharacteristic,

$$\mathbf{V}_p \;=\; \mathbf{u} + \mu_n a\mathbf{N} + a\left[\hat{\mathbf{n}} - (\hat{\mathbf{n}}\cdot\mathbf{N})\,\mathbf{N}\right]\;. \tag{2.83}$$

Fig. 2.8 shows the projection of the characteristic conoid on a particular surface R_n = const, which is space-like; *i.e.*, $|\mu_n| > 1$. It is reasonable to try to use paths contained in the projected conoid for computational purposes. The paths given by Eqs. (2.67) and (2.70) are in this projection.

Using Eq. (2.83), it is easy to examine the intersection of the manifold R_n = const and the local characteristic ray cone. This is done by requiring

$$\mathbf{V}_p = \mathbf{u} + a\hat{\mathbf{n}} \,. \tag{2.84}$$

In other words, the projection vector $\mathbf{V}_p$, tangent to the Riemann Invariant Manifold, is required to be a bicharacteristic vector. From Eq. (2.83) it is seen that one must have

$$\hat{\mathbf{n}}\cdot\mathbf{N} = \mu_n \,. \tag{2.85}$$

Since $\hat{\mathbf{n}}$ and $\mathbf{N}$ are unit vectors, this equation has a solution only when $-1 \leq \mu_n \leq 1$, *i.e.*, when the Riemann Invariant Manifold is time-like or characteristic. This is to be expected because, by definition, a space-like surface element cannot intersect the local characteristic ray cone. It is interesting that when the surface element is not space-like, it is possible to find bicharacteristic directions along which an equivalent, one-dimensional problem holds. This situation would be the direct extension of the method of characteristics to multidimensional flows, as it has been attempted in the past. A special solution is the one discussed earlier for the case $\hat{\mathbf{n}} = \mathbf{n}$. In this case Eq. (2.85) reduces to

$$\mathbf{n}\cdot\mathbf{N} = \mu_n \,. \tag{2.86}$$

Using Eq. (2.71),

$$\mathbf{n}\cdot\mathbf{N} = \mu_n \quad \Rightarrow \quad G_n = [\nabla\cdot\mathbf{u} - \mathbf{n}\cdot(\nabla\mathbf{u})\,\mathbf{n}] = 0 \,. \tag{2.87}$$

Yet another way to visualize the relative position of the Riemann Invariant surfaces and the characteristic manifolds is to examine the cone generated by the vector field (2.78) in relation to the characteristic ray cone generated by the bicharacteristic vector field. The Riemann Invariant cone is generated by varying the unit vector $\mathbf{n}$. It will be different for the different possible choices of $\mathbf{V}$ on each surface R_n = const. Examples are shown for the case of two-dimensional flow in Figs. (2.9)–(2.12). The direction chosen for these examples is that given by Eq. (2.67).

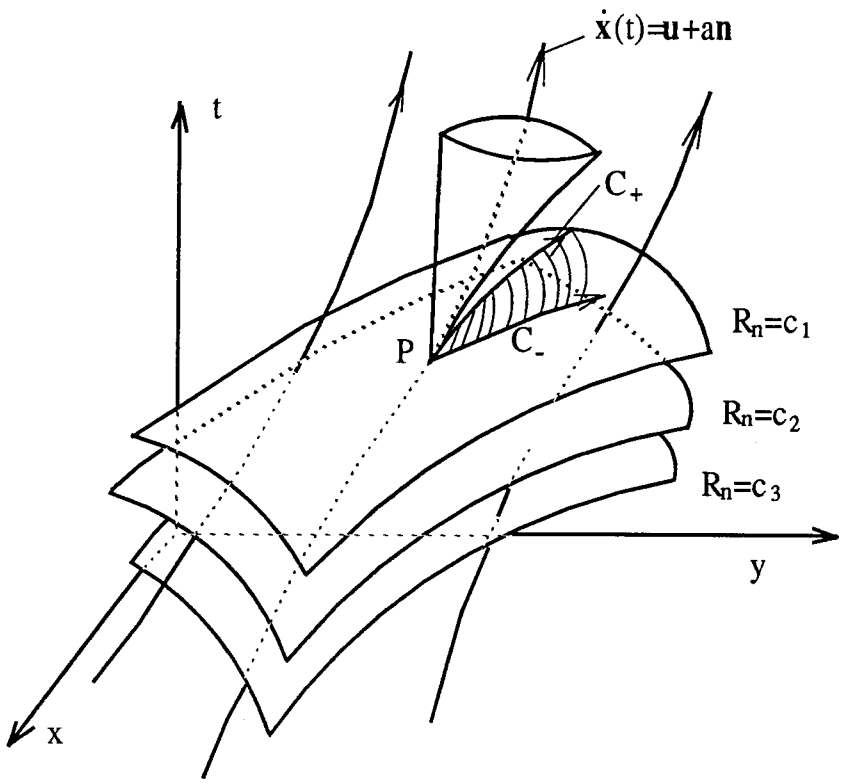

FIG.2.8 The projection of the characteristic conoid at P, on the manifold $R_n = c_1$, is shown for the particular case $|\mu_n| > 1$. It is contained between the curves C_- and C_+.

Moreover, the point of interest is located at $(x, y) = (0, 0)$, the pressure is $p = 1$, the density is $\rho = 1$ and the velocity is $(u, v) = (0.5, 0.5)$. The plots shown are slices $t = 1$ of the two cones, *i.e.*, the so-called ray surfaces. The bicharacteristic ray surface is a circle.

2.3 Riemann Invariant Manifolds and Domain of Dependence

It is important, at this point, to make some remarks about the information that is provided by the local geometry of these Riemann Invariant Manifolds. The fluid velocity **u** and the speed of sound a provide information about the local geometry of the characteristic surfaces. In particular, they give the local, bicharacteristic cone. The significance of the characteristic surfaces has been discussed previously. Their interpretation as waves of derivative discontinuities is important. What is more

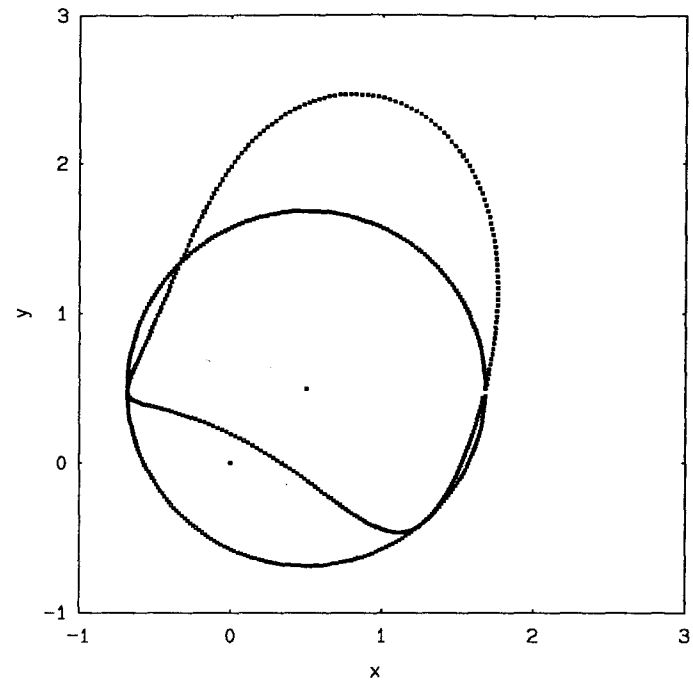

FIG.2.9 The bicharacteristic ray surface in relation to the Riemann Invariant ray surface for the case $\nabla u = (1,0)$, $\nabla v = (-1,0)$ and $\nabla p = (1,2)$.

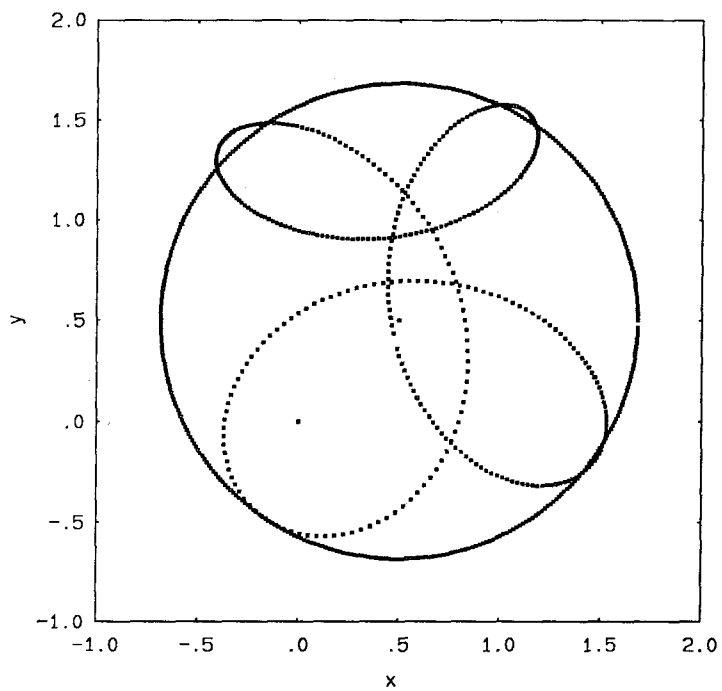

FIG.2.10 The bicharacteristic ray surface in relation to the Riemann Invariant ray surface for the case $\nabla u = (5,2)$, $\nabla v = (1,-6)$ and $\nabla p = (1,-2)$.

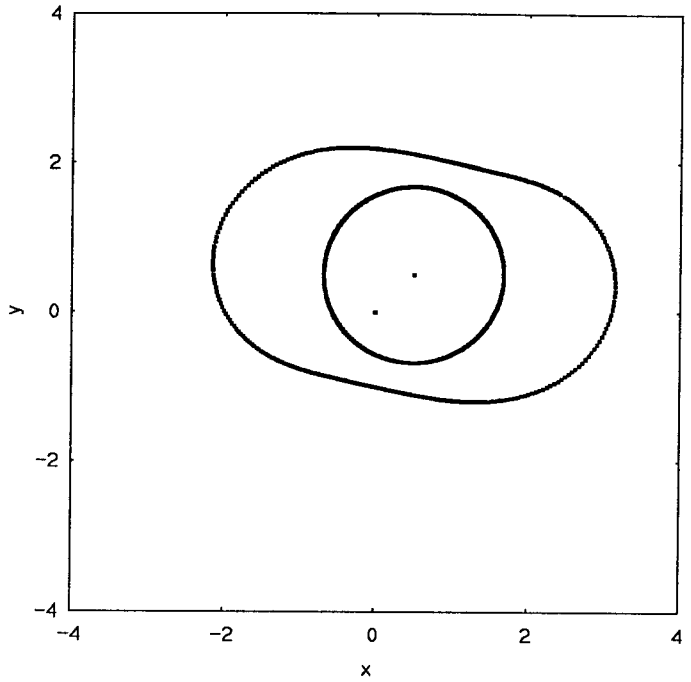

FIG.2.11 The bicharacteristic ray surface in relation to the Riemann Invariant ray surface for the case $\nabla u = (2,3)$, $\nabla v = (-2,4)$ and $\nabla p = (0,0)$.

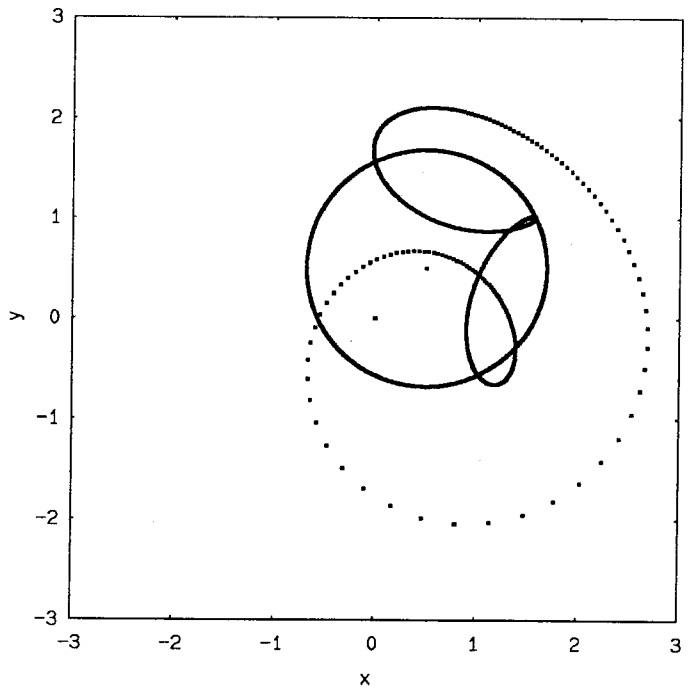

FIG.2.12 The bicharacteristic ray surface in relation to the Riemann Invariant ray surface for the case $\nabla u = (7,-5)$, $\nabla v = (-6,-7)$ and $\nabla p = (5,-7)$.

significant is the role they play in proving the existence and uniqueness of solutions. The characteristic surfaces determine the domains of dependence and influence of the solution. The concepts of domains of dependence and influence are a direct result of the assumptions and results of these theorems.

Knowledge of the local, spatial gradients in the flow provides additional information. They provide all the information required for the Riemann Invariant Manifolds and in particular, the parameter μ_n. It is important to note that the solution at points on these manifolds are related in a simple way. Moreover, these relations can be used to determine the solution at a given point. What may appear disturbing at first sight is that these manifolds may be space-like. In other words, the solution at some point may be computed from the solution at points outside its domain of dependence. See, for example, Fig. 2.11. Actually, in the case of zero-entropy gradients, there is a simple, explicit algebraic expression relating points connected by space-like paths in spacetime given by the Riemann Invariant $R_n = W + \mathbf{u}\cdot\mathbf{n}$. It then becomes trivial to compute the solution at a given point from the solution at points on these Riemann Invariant Manifolds. The difficulty is transferred to the task of finding the exact location of the relevant points by integrating $\dot{\mathbf{x}}(t) = \mathbf{V}$. In any case, no matter what their exact location is, these points are going to be outside the domain of dependence, if the Riemann Invariant Surface is space-like. At first sight, there appears to be a disturbing inconsistency with the concept of domain of dependence as described in the uniqueness theorems. Fig. 2.13 is a simplified, one-dimensional picture illustrating this situation. The solution at point P is computed by using the known solution at points Q_1 and Q_2 outside the domain of dependence D.

Careful examination of the existence and uniqueness theorems for these hyperbolic systems of equations shows that there is really no such inconsistency. It is true that if the data in D are different, then the solution at P will change. But so will the paths Q_1P and Q_2P. What seems odd at first is that even though the data in D are *sufficient* to determine the solution at P, there are points outside D where the data are "related" to the solution at P. The uniqueness statement is that *points outside D cannot affect the solution at P.* This is usually interpreted as meaning that any relation between the data outside D and at P must be completely random, depending on the data on the surface $t = 0$. This is not true. The local, spatial gradients determine a local relation of this form along space-like

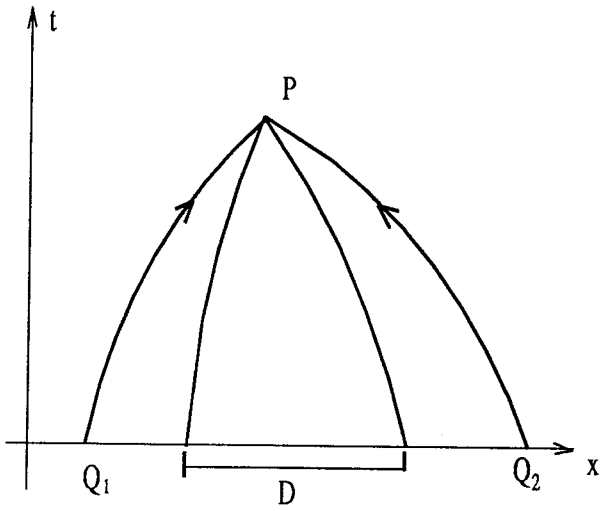

FIG.2.13 The solution at point P is related trivially through the Riemann Invariant functions to the solution at points Q_1 and Q_2, which are outside the domain of dependence D.

paths. The data in D are *sufficient* to determine the solution at P, and if the data in D are altered, the solution at P will change. Nevertheless, the solution at P *is not completely unrelated to the data outside* D. This has to do with the fact that knowledge of the local spatial gradients and their smoothness constitutes additional information about how the initial data on $t = 0$ are related. The uniqueness proofs are based on requiring the absolute minimum in terms of smoothness restrictions on the data. The data are simply required to be continuous. Discontinuities in the derivatives are allowed, and it was shown that these discontinuities are propagated by the characteristic surfaces. Other singularities in the derivatives also propagate along the characteristic surfaces. If the data are allowed to have jump discontinuities, then these jumps will propagate along the shock manifolds. The characteristic surfaces separate the regions of spacetime, where the derivatives of the solution are continuous. It is in these regions that knowledge of the gradients provides additional information about the solution. This additional information is conveniently visualized through the geometry of the Riemann Invariant Manifolds and can be used for computational purposes.

2.4 Conclusions

The theory of Riemann Invariant Manifolds extends the method of characteristics to multidimensional flows. It provides the theoretical framework for developing numerical schemes that are genuinely multidimensional. The one-dimensional characteristic problem is the basic building block for most high-resolution, shock-capturing schemes in use today. This theory allows one to use the 1-D problem for multidimensional calculations in a mathematically consistent way. There is no unique, numerical implementation of these ideas. The theory suggests that the 1-D characteristic problem may be used along trajectories that lie on the Riemann Invariant Manifolds. This is a necessary constraint, but additional degrees of freedom are available for picking a numerical scheme.

CHAPTER 3

A Multidimensional Godunov Scheme

The theory of Riemann Invariant Manifolds will now be used to construct a conservative, shock-capturing scheme for unsteady, two-dimensional flow. The basis for the scheme is a second-order Godunov scheme (MUSCL scheme, van Leer, 1979), which is modified to take into account the multidimensional character of the flow. The numerical fluxes are computed by tracing the appropriate Riemann Invariant Manifolds back in time, in order to find the states that are related with an equivalent, one-dimensional Riemann problem. This results in a multidimensional scheme without flux-splitting, *i.e.*, a truly unsplit scheme. The application of the theory is demonstrated for two-dimensional flow, but the extension to three-dimensional flow is straightforward. It is important to note that the theory of Riemann Invariant Manifolds can be used to construct a variety of multidimensional, numerical schemes. What follows is simply one example of how a Godunov-type scheme can be corrected for multidimensional effects.

3.1 Second-Order Godunov Scheme

A description of the MUSCL scheme will be given, since this is the basis for the proposed multidimensional scheme. Most high-order, shock-capturing schemes have been developed using the theory of hyperbolic systems in one space dimension and time. It is therefore convenient to describe the scheme for this special 1-D case and then to show a conventional extension to many spatial dimensions.

The goal is to solve numerically the general, nonlinear system of equations

$$\frac{\partial U}{\partial t} + \frac{\partial F(U)}{\partial x} = 0 \,. \tag{3.1}$$

This is a general conservation law, where t is the time variable, x is the space variable and $U = U(t,x) \in \Re^M$ is the conserved unknown vector. For the case of 1-D gasdynamics,

$$U = \begin{pmatrix} \rho \\ \rho u \\ \rho e_t \end{pmatrix}, \quad F(U) = \begin{pmatrix} \rho u \\ \rho u^2 + p \\ \rho u e_t + p u \end{pmatrix}, \tag{3.2}$$

where ρ is the density, p the pressure, u the velocity of the gas and $e_t = \left(e + \frac{1}{2}\, u^2\right)$ is the total energy. The internal energy e is related to the pressure p by

$$p = (\gamma - 1)\rho e\,, \tag{3.3}$$

for the case of a perfect gas with constant, specific heat ratio γ.

A finite-volume formulation is used. The spatial domain is discretized, and the average value of the conserved vector U in the j^{th} cell is denoted by U_j. Quantities associated with the two interfaces of the j^{th} cell are denoted by the subscripts $j \pm 1/2$. A general conservative scheme is of the form

$$U_j^{n+1} = U_j^n - \frac{\Delta t}{\Delta x}\left(\tilde{F}_{j+1/2} - \tilde{F}_{j-1/2}\right). \tag{3.4}$$

This is really an application of the integral-conservation form of Eq. (3.1) to the j^{th} cell. It gives the cell-averaged, conserved vector U at the time level $n+1$ from the previous time level n. Δx is the size of the cell and Δt is the timestep. The quantities $\tilde{F}_{j\pm1/2}$ are the time-averaged fluxes at the two cell interfaces; *i.e.*,

$$\tilde{F}_{j\pm1/2} \equiv \frac{1}{\Delta t}\int_{t_n}^{t_n+\Delta t} F\left(U_{j\pm1/2}\right) dt\,, \tag{3.5}$$

where $F = F(U)$ is given by Eq. (3.2). It is important to notice that Eq. (3.4) is *exact*. In a numerical scheme it is not possible to calculate the integrals given in Eq. (3.5) exactly. The integrals are therefore approximated, and the final numerical scheme is of the form

$$U_j^{n+1} = U_j^n - \frac{\Delta t}{\Delta x}\left(\hat{F}_{j+1/2} - \hat{F}_{j-1/2}\right), \tag{3.6}$$

where the quantities $\hat{F}_{j\pm1/2}$ are the numerical approximations of the $\tilde{F}_{j\pm1/2}$. Every conservative scheme reduces to calculating the numerical fluxes $\hat{F}_{j\pm1/2}$ at the cell interfaces. All Godunov schemes attempt to compute these fluxes by using the knowledge from the theory of characteristics, locally, at each cell interface. By doing this, the local characteristic wave patterns are accounted for, accurately. Since discontinuities are likely to be present, the characteristic problem is generalized to allow for their presence. This constitutes the well-known Riemann problem. How this is done for the case of a second-order Godunov scheme (MUSCL) will now be described.

At any given time t_n, one has only the average values of U in each computational cell, as given by the discrete scheme (3.6). The first step in calculating the numerical fluxes $\hat{F}_{j\pm1/2}$ is to reconstruct the solution at time t_n by some kind of spatial interpolation. This is a very important step, because the presence of discontinuities in these flows may cause problems. This constitutes the most important step for a variety of high-order, conservative schemes. The second step, then, is to use the knowledge of the solution at this time level to solve a local, characteristic problem in order to calculate the numerical fluxes. These two steps will be given for the MUSCL scheme.

A linear variation of the primitive variables ρ, p and u is assumed in each cell. The generic quantity q is given by

$$q(x) \;=\; q_j + (q_x)_j \;(x - x_j) \;, \tag{3.7}$$

in the j^{th} cell, where q_j is the average value in the cell, x_j is the center of the cell and $(q_x)_j$ is the slope of q in this cell, which is assumed to be constant. Note that discontinuities of these quantities are allowed at the cell interfaces, as shown in Fig. 3.1.

The slope $(q_x)_j$ is computed, following van Leer (1984), by

$$(q_x)_j \;=\; \text{ave}\left(q_x^- \;,\; q_x^+\right) \;, \tag{3.8}$$

where

$$q_x^- \;=\; \frac{q_j - q_{j-1}}{x_j - x_{j-1}} \quad , \quad q_x^+ \;=\; \frac{q_{j+1} - q_j}{x_{j+1} - x_j} \;, \tag{3.9}$$

$$\text{ave}(x,y) \;\equiv\; \frac{x+y}{2}\left[1 - \frac{(x-y)^2}{x^2 + y^2 + c^2}\right] \;, \tag{3.10}$$

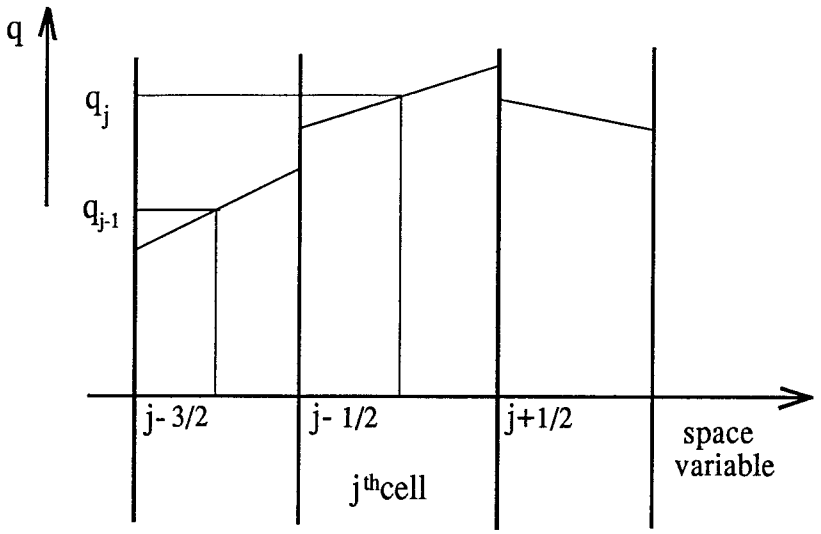

FIG.3.1 Linear variation of the generic quantity q in the j^{th} cell. In general, q is discontinuous at the cell interfaces.

and c^2 is a small constant ($c^2 \ll 1$). This slope-limiting procedure ensures the preservation of monotonicity in the interpolant in regions of discontinuities.

The numerical fluxes $\hat{F}_{j\pm1/2}$ are calculated by Eq. (3.5), using the midpoint rule, *i.e.*,

$$\hat{F}_{j\pm1/2} = F\left(U^{n+1/2}_{j\pm1/2}\right) , \tag{3.11}$$

where the superscript $n+1/2$ denotes the half-time level $t_n + \Delta t/2$. The problem of finding the numerical fluxes becomes that of estimating the solution vector U at the cell interfaces at the time $t_n + \Delta t/2$. This procedure ensures second-order accuracy in time.

The domain of dependence of $x = x_{j+1/2}$ over the time interval $\Delta t/2$ is estimated by the characteristics at the time level t. The characteristic speeds are given by

$$c_\pm = u \pm a , \qquad c_0 = u , \tag{3.12}$$

where a is the speed of sound. In the example shown in Fig. 3.2, the flow is subsonic; *i.e.*, $c_+ > 0$ and $c_- < 0$. It is known that along the characteristics $C_\pm$ the following differential equations hold:

$$\left[\frac{\partial p}{\partial t} + (u \pm a)\frac{\partial p}{\partial x}\right] \pm \rho a \left[\frac{\partial u}{\partial t} + (u \pm a)\frac{\partial u}{\partial x}\right] = 0 . \tag{3.13}$$

These two equations are written in the more conventional form as

$$\frac{dp}{dt} \pm \rho a \frac{du}{dt} = 0 , \tag{3.14}$$

where the time derivatives are derivatives along the appropriate characteristic directions. Along the streamline C_0,

$$\left[\frac{\partial p}{\partial t} + u\frac{\partial p}{\partial x}\right] - a^2 \left[\frac{\partial \rho}{\partial t} + u\frac{\partial \rho}{\partial x}\right] = 0 , \tag{3.15}$$

or

$$\frac{dp}{dt} - a^2 \frac{d\rho}{dt} = 0 , \tag{3.16}$$

which is equivalent to the statement that the entropy remains constant along the streamline.

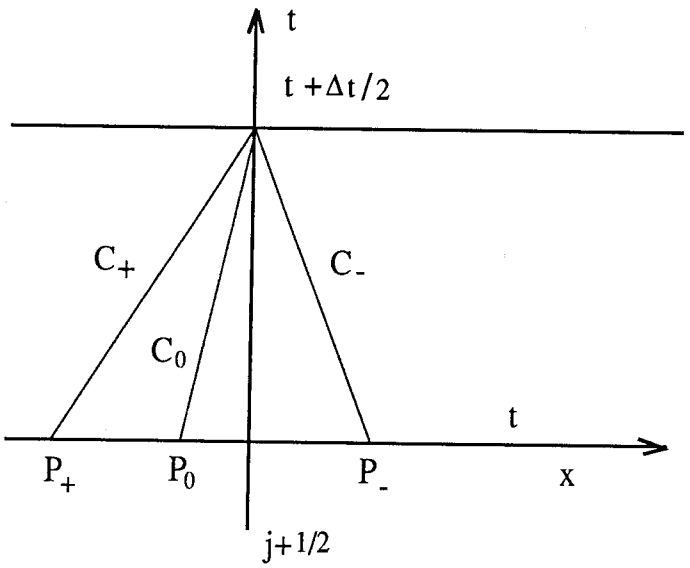

FIG.3.2 The constant states, which are to be used as the initial condition for the Riemann problem at the interface $j + 1/2$, are obtained by tracing the characteristics back in time from the half-time level $t + \Delta t/2$. In this example the flow is subsonic; *i.e.*, $c_+ > 0$ and $c_- < 0$.

Eqs. (3.14) and (3.16) form the basis for the well-known theory of characteristics in 1-D gas dynamics. Moreover, when supplemented with the jump conditions, they form the basis for the solution of the 1-D Riemann problem. It is the states at the points $P_\pm$ in Fig. 3.2 that are used as the two initial states for the 1-D Riemann problem. The solution of this Riemann problem is the state used in Eq. (3.11) to compute the numerical fluxes.

There are many variations of the MUSCL scheme that arise from changing the spatial interpolation scheme or changing the way the states for the Riemann problem are chosen. A different way of picking the two states is by using a Taylor series expansion on either side of the interface $j+1/2$. The left state of the initial condition for the Riemann problem is given by the following expansion about the center of the j^{th} cell,

$$\begin{aligned} U_L &= U_j + (x - x_c)\frac{\partial U}{\partial x} + \frac{\Delta t}{2}\frac{\partial U}{\partial t} \\ &= U_j + (x - x_c)\left(\frac{\partial U}{\partial x}\right) - \frac{\Delta t}{2} A \left(\frac{\partial U}{\partial x}\right) \\ &= U_j + \left[(x - x_c)\, I - \frac{\Delta t}{2} A\right]\left(\frac{\partial U}{\partial x}\right), \end{aligned} \tag{3.17}$$

where x_c is the center of the cell, I is the unit matrix and

$$A \equiv \frac{\partial F(U)}{\partial U}. \tag{3.18}$$

The spatial derivatives are constant in each cell, since a linear interpolant is used. Similarly, one finds the right state U_R by expanding in the $(j+1)^{\text{th}}$ cell. The two states found by the Taylor series expansion are not really related by a 1-D Riemann problem, even in the case of smooth flow without any shock waves. It does not take into account accurately the local, characteristic wave patterns. Nevertheless, this procedure works in practice, and it is mentioned because it can be extended to the multidimensional case in a straightforward way. One can also introduce corrections to the states obtained in this way to account for the local wave patterns.

The process of tracing the characteristics back in time is the best way to find the initial condition for the Riemann problem for the 1-D case, but this procedure cannot be extended to the multidimensional case. This is a general problem of all similar methods that use knowledge of the theory of hyperbolic systems in one space dimension to compute numerical fluxes. It is at this point where one can use the theory of Riemann Invariant Manifolds to find the states that are connected with an equivalent 1-D characteristic problem.

The conventional way of extending these 1-D schemes to more space dimensions is through Strang-type, dimensional splitting, given in Strang (1968). Each spatial dimension is treated separately, and the result is the "sum" of one-dimensional problems in the grid directions. Unsplit schemes like that of Colella (1990) use the

grid direction to set up a 1-D problem, but the states used as the initial condition for the Riemann problem are not clearly related via a 1-D problem, even though they are corrected for multidimensional effects. The only real effort to create a multidimensional scheme is that by Roe (1986); Hirsch & Lacor (1989), and Deconinck *et al.* (1986). It is also easy to extend the Taylor-series expansion method, mentioned earlier, to multidimensional flows. The states computed in that way are not clearly related via the 1-D characteristic equations, but the resulting scheme works in practice. Moreover, this scheme is a good reference point for the multidimensional schemes that are proposed, using the theory of the Riemann Invariant Manifolds.

Consider now the case of two-dimensional flow of a perfect gas. The second-order Godunov scheme will be described and used as the starting point for the proposed multidimensional corrections. The local geometry of a 2-D computational cell is shown in Fig. 3.3. An orthogonal grid in the x and y-directions is used. As will be seen later, this restriction on the grid can be dropped when the multidimensional corrections are introduced.

The equations of motion for the two-dimensional case are

$$\frac{\partial U}{\partial t} + \frac{\partial F_x(U)}{\partial x} + \frac{\partial F_y(U)}{\partial y} = 0 \,, \tag{3.19}$$

where

$$U = \begin{pmatrix} \rho \\ \rho u \\ \rho v \\ \rho e_t \end{pmatrix}, \quad F_x(U) = \begin{pmatrix} \rho u \\ p + \rho u^2 \\ \rho uv \\ \rho u e_t + pu \end{pmatrix}, \quad F_y(U) = \begin{pmatrix} \rho v \\ \rho uv \\ p + \rho v^2 \\ \rho v e_t + pv \end{pmatrix}. \tag{3.20}$$

$\mathbf{u} = (u, v)^{\mathrm{T}}$ is the two-dimensional, velocity vector, and $e_t = e + \frac{1}{2}|\mathbf{u}|^2$ is the total energy. The internal energy e is related to the pressure p by the perfect gas equation of state (3.3).

The spatial-interpolation scheme is the one-dimensional scheme given by Eqs. (3.7)–(3.10) and is implemented in the two orthogonal grid directions. As mentioned earlier, the spatial-interpolation scheme is a very important step, but is independent of the efforts to correct for multidimensional effects in the time integration. One can devise higher-order interpolation schemes, which take into account the presence of discontinuities, such as the interpolation used in ENO schemes. See Harten *et*

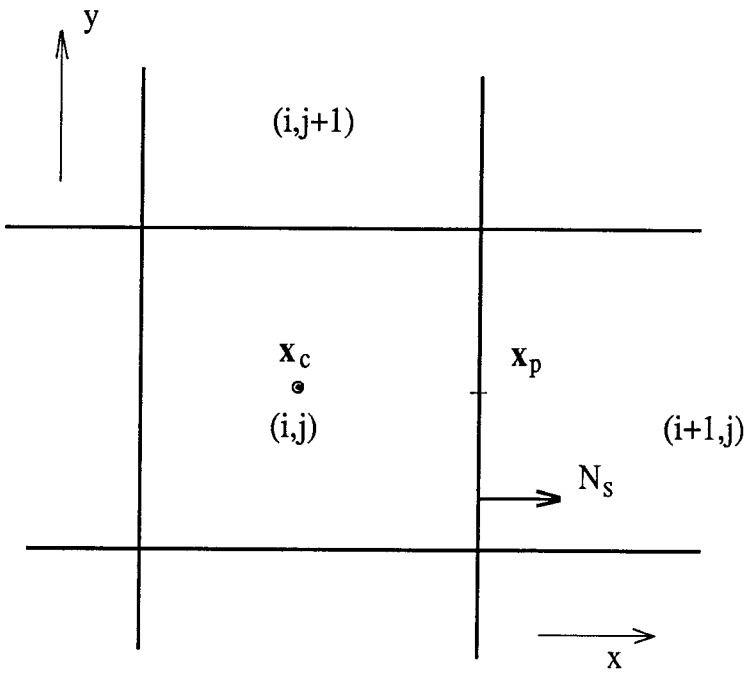

FIG.3.3 The geometry of the 2-D computational cell (i,j). The interface between the cells (i,j) and $(i+1,j)$ is denoted by $(i+1/2,j)$. $\mathbf{N}_s$ is the unit vector normal to this interface. For an orthogonal grid this corresponds to the unit vector in the x-direction.

al. (1987). It is also possible to devise schemes that work on unstructured grids. At any given time, knowledge of the spatial gradients of the flow will be assumed in using the theory of Riemann Invariant Manifolds to develop a multidimensional scheme.

The two states that are used as the initial condition for the Riemann problem at the interface $(i+1/2,j)$ are given by the Taylor series expansions on either side of the interface. The left state is given by expanding about the center of the $(i,j)^{\text{th}}$ cell to the center of the interface, $\mathbf{x}_p$, at the later time $t+\Delta t/2$. It is easy to see that the extension of Eq. (3.17) to the two-dimensional case is

$$U_L \;=\; U_{ij} + \left[(\mathbf{x}_p - \mathbf{x}_c)\, I - \frac{\Delta t}{2}\mathbf{A}\right]\cdot\nabla U \;, \tag{3.21}$$

where $\mathbf{x}_c$ is the center of the cell, I is the unit matrix and

$$\mathbf{A} \;\equiv\; (A_x, A_y)^{\mathrm{T}} \;=\; \left(\frac{\partial F_x(U)}{\partial U}, \frac{\partial F_y(U)}{\partial U}\right)^{\mathrm{T}} \;. \tag{3.22}$$

It is more convenient to expand the primitive variables ρ, p and $\mathbf{u}$ instead of the conserved vector U. The left state is, then, given by

$$\rho_L = \rho + [(\mathbf{x}_p - \mathbf{x}_c) - \mathbf{u}\delta t]\cdot\nabla\rho - \delta t\rho\nabla\cdot\mathbf{u}\,, \tag{3.23}$$

$$p_L = p + [(\mathbf{x}_p - \mathbf{x}_c) - \mathbf{u}\delta t]\cdot\nabla p - \delta t\rho a^2\nabla\cdot\mathbf{u}\,, \tag{3.24}$$

$$\mathbf{u}_L = \mathbf{u} + [(\mathbf{x}_p - \mathbf{x}_c) - \mathbf{u}\delta t]\cdot\nabla\mathbf{u} - \delta t\frac{1}{\rho}\nabla p\,, \tag{3.25}$$

where $\delta t \equiv \Delta t/2$ and all quantities are evaluated at the center of the $(i,j)^{\text{th}}$ cell. Similarly, one can find the right state by Taylor expanding about the center of the $(i+1,j)^{\text{th}}$ cell. The velocity component normal to the interface, *i.e.*, $\mathbf{u}_L\cdot\mathbf{N}_s$ is used as the left scalar velocity for the 1-D Riemann problem. In other words, a one-dimensional Riemann problem is solved in the direction of the grid line, using the above left and right states. As mentioned earlier, these states are not truly related by the 1-D characteristic equations even in smooth, shock-free flow. The tangential velocity component used to compute the numerical fluxes at the interface, is $\mathbf{u}_L\cdot\mathbf{N}_s^{\perp}$ if $\mathbf{u}_L\cdot\mathbf{N}_s > 0$; otherwise it is $\mathbf{u}_R\cdot\mathbf{N}_s^{\perp}$. The notation

$$\mathbf{a}^{\perp} \equiv (\hat{e}_x \times \hat{e}_y) \times \mathbf{a}\,, \tag{3.26}$$

for an arbitrary, two-dimensional vector $\mathbf{a}$, will be used throughout. $\mathbf{a}^{\perp}$ is just $\mathbf{a}$, rotated by 90°.

3.2 Multidimensional, Second-Order Godunov Scheme

In order to correct this scheme for multidimensional effects, it is proposed to use the Riemann Invariant Manifolds that pass through the interface to find the states that are truly related through an equivalent one-dimensional, characteristic problem.

As a first step, the geometry of the Riemann Invariant Manifold $R_n = \text{const}$, corresponding to the arbitrary unit vector $\mathbf{n}$, will be examined in the vicinity of the computational cell (i,j). The spatial gradients are assumed known from the spatial-interpolation scheme. Moreover, the spatial gradients are constant in each cell, since a linear interpolation is used. The unit normal $\mathbf{N}$ and the algebraic normal Mach number μ_n of the 2-D front $R_n = \text{const}$ are given by

$$\mathbf{N} = \frac{\nabla p + \rho a(\nabla\mathbf{u})^{\mathrm{T}}\mathbf{n}}{\left|\nabla p + \rho a(\nabla\mathbf{u})^{\mathrm{T}}\mathbf{n}\right|}\,, \tag{3.27}$$

$$\mu_n \equiv \frac{\mathbf{n}\cdot\nabla p + \rho a \nabla\cdot\mathbf{u}}{\left|\nabla p + \rho a \left(\nabla\mathbf{u}\right)^{\mathrm{T}}\mathbf{n}\right|} . \tag{3.28}$$

Both quantities are assumed constant in each computational cell. An arbitrary direction on the manifold $R_n = \text{const}$ is given by

$$\dot{\mathbf{x}}_n(t) = \mathbf{u} + a\boldsymbol{\nu} , \tag{3.29}$$

where

$$\boldsymbol{\nu} \equiv \mu_n \mathbf{N} + \mu_t \mathbf{N}^{\perp} . \tag{3.30}$$

μ_t is unspecified and it reflects the infinity of paths on this particular manifold. The Mach number of a particular trajectory $\dot{\mathbf{x}}_n(t)$ is

$$\mu \equiv |\boldsymbol{\nu}| = \sqrt{\mu_n^2 + \mu_t^2} > 0 . \tag{3.31}$$

This positive number μ contains the information about the relative position of the corresponding trajectory and the bicharacteristic conoid. When $\mu = 1$, the path is tangent to the bicharacteristic cone. When $\mu < 1$, it is time-like and when $\mu > 1$, it is space-like.

The solution is known at time t. From the knowledge of the spatial gradients of the flow it is possible to find, approximately, all paths on the manifold $R_n = \text{const}$, which pass through the center of the interface $(i + 1/2, j)$ at time $t + \delta t$. These paths must be such that

$$\mathbf{x}_p = \mathbf{x}_n(t+\delta t) = \mathbf{x}_n(t) + \int_t^{t+\delta t} \left[\mathbf{u}(\tau, \mathbf{x}_n(\tau)) + a(\tau, \mathbf{x}_n(\tau))\boldsymbol{\nu}(\tau, \mathbf{x}_n(\tau))\right] d\tau . \tag{3.32}$$

By approximating these paths by straight lines in time, one finds

$$\mathbf{x}_p \approx \mathbf{x}_w + \delta t \left[\mathbf{u}(t, \mathbf{x}_w) + a(t, \mathbf{x}_w)\boldsymbol{\nu}(t, \mathbf{x}_w)\right] , \tag{3.33}$$

where $\mathbf{x}_w \equiv \mathbf{x}_n(t)$. Using the linear interpolants for the velocity $\mathbf{u}$ and the speed of sound a at time t and the fact that $\boldsymbol{\nu}$ is constant in each cell,

$$\mathbf{x}_p - \mathbf{x}_w \approx \delta t \left\{\mathbf{u} + (\mathbf{x}_w - \mathbf{x}_c)\cdot\nabla\mathbf{u} + \left[a + (\mathbf{x}_w - \mathbf{x}_c)\cdot\nabla a\right]\boldsymbol{\nu}\right\} , \tag{3.34}$$

where all quantities are now evaluated at the center of the cell. Eq. (3.34) can be used to solve for $\mathbf{x}_w$ as a function of μ_t. It can be written as

$$\left[I + \delta t \left(\nabla\mathbf{u} + \boldsymbol{\nu}\nabla a\right)\right](\mathbf{x}_w - \mathbf{x}_c) \approx \mathbf{x}_p - \mathbf{x}_c - \delta t \left(\mathbf{u} + a\boldsymbol{\nu}\right) . \tag{3.35}$$

Eq. (3.35) is a linear system in the unknown vector $\mathbf{x}_w - \mathbf{x}_c$. The determinant of this system is easily found to be

$$\begin{aligned} D &= 1 + \delta t\,(\nabla\cdot\mathbf{u}) + \delta t^2 \det(\nabla\mathbf{u}) + \delta t\ \boldsymbol{\nu}\cdot\left[I + \delta t(\widehat{\nabla\mathbf{u}})\right]\nabla a \\ &= 1 + \delta t\,(\nabla\cdot\mathbf{u} + \boldsymbol{\nu}\cdot\nabla a) + \delta t^2\left[\det(\nabla\mathbf{u}) + \boldsymbol{\nu}\cdot(\widehat{\nabla\mathbf{u}})\nabla a\right] . \end{aligned} \tag{3.36}$$

For small enough timestep δt, $D \approx 1$. Eq. (3.35) can be solved to give

$$\mathbf{x}_p - \mathbf{x}_w = (1 - 1/D)\,\Delta\mathbf{x}_p + \frac{\delta t}{D}\left[\mathbf{u} - (\widetilde{\nabla\mathbf{u}})\,(\Delta\mathbf{x}_p - \delta t\mathbf{u})\right] + \frac{\delta t}{D} a\hat{T}\boldsymbol{\nu} , \tag{3.37}$$

where $\Delta\mathbf{x}_p \equiv \mathbf{x}_p - \mathbf{x}_c$, $a\hat{T}$ is the tensor

$$a\hat{T} \equiv aI + (\nabla a)^{\perp}(\Delta\mathbf{x}_p)^{\perp} + \delta t\left[a(\widetilde{\nabla\mathbf{u}}) - (\nabla a)^{\perp}\mathbf{u}^{\perp}\right] , \tag{3.38}$$

and

$$(\widehat{\nabla\mathbf{u}}) \equiv \begin{pmatrix} \dfrac{\partial v}{\partial y} & \dfrac{\partial v}{\partial x} \\ \dfrac{\partial u}{\partial y} & \dfrac{\partial u}{\partial x} \end{pmatrix}, \quad (\widetilde{\nabla\mathbf{u}}) \equiv \begin{pmatrix} \dfrac{\partial v}{\partial y} & -\dfrac{\partial u}{\partial y} \\ -\dfrac{\partial v}{\partial x} & \dfrac{\partial u}{\partial x} \end{pmatrix} . \tag{3.39}$$

Eq. (3.37) gives $\mathbf{x}_w$ as a function of μ_t, which is contained in $\boldsymbol{\nu}$. In other words, it is the locus of all points, at time t, that are connected with point $(t + \delta t, \mathbf{x}_p)$ by the 1-D characteristic differential equation

$$\frac{dp}{dt} + \rho a \frac{du_n}{dt} = 0 , \tag{3.40}$$

where $u_n = \mathbf{u}\cdot\mathbf{n}$, for the particular choice of $\mathbf{n}$.

For the point $\mathbf{x}_w$ to be inside the cell (i, j), the following relations must hold

$$\begin{aligned} 0 < (\mathbf{x}_p - \mathbf{x}_w)\cdot\mathbf{N}_s &< \delta x \\ \left|(\mathbf{x}_p - \mathbf{x}_w)\cdot\mathbf{N}_s^{\perp}\right| &< 0.5\delta y , \end{aligned} \tag{3.41}$$

where $(\delta x, \delta y)$ is the size of the cell. If the point $\mathbf{x}_w$ is restricted to the half of the cell closest to the interface $(i + 1/2, j)$, then

$$\begin{aligned} 0 < (\mathbf{x}_p - \mathbf{x}_w)\cdot\mathbf{N}_s &< 0.5\delta x \\ \left|(\mathbf{x}_p - \mathbf{x}_w)\cdot\mathbf{N}_s^{\perp}\right| &< 0.5\delta y , \end{aligned} \tag{3.42}$$

Eq. (3.37) can be used to find the range of the parameter μ_t for which the inequalities (3.41) or (3.42) hold. This range can be found explicitly if the simplifying assumption $D \approx 1$ is made. In that case, Eq. (3.37) becomes

$$\frac{\mathbf{x}_p - \mathbf{x}_w}{\delta t} \approx \mathbf{V}_c + a\hat{T}\boldsymbol{\nu} , \tag{3.43}$$

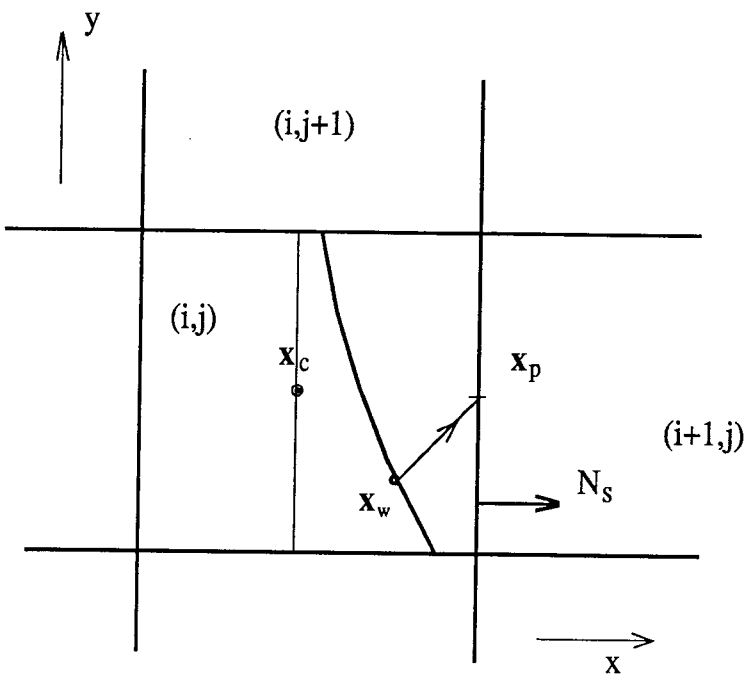

FIG.3.4 The locus of all points $\mathbf{x}_w$ in the cell (i,j) at time t, which are connected with point $(t+\delta t, \mathbf{x}_p)$ by the 1-D characteristic differential Equation (3.40).

where

$$\mathbf{V}_c \equiv \mathbf{u} - (\widetilde{\nabla \mathbf{u}})(\Delta \mathbf{x}_p - \delta t \mathbf{u}) \ . \tag{3.44}$$

The inequalities (3.42) can now be written

$$\begin{aligned} 0 < u_s < 0.5\frac{\delta x}{\delta t} &\equiv 0.5u_g \\ |v_s| < 0.5\frac{\delta y}{\delta t} &\equiv 0.5v_g \ , \end{aligned} \tag{3.45}$$

where

$$\begin{aligned} u_s &\equiv \frac{\mathbf{x}_p - \mathbf{x}_w}{\delta t}\cdot\mathbf{N}_s = \mathbf{V}_c\cdot\mathbf{N}_s + a\boldsymbol{\nu}\cdot\left(\hat{T}^{\mathrm{T}}\mathbf{N}_s\right) \\ v_s &\equiv \frac{\mathbf{x}_p - \mathbf{x}_w}{\delta t}\cdot\mathbf{N}_s^{\perp} = \mathbf{V}_c\cdot\mathbf{N}_s^{\perp} + a\boldsymbol{\nu}\cdot\left(\hat{T}^{\mathrm{T}}\mathbf{N}_s^{\perp}\right) \ . \end{aligned} \tag{3.46}$$

Using Eq. (3.30), the inequalities (3.45) become

$$\begin{aligned} 0 < \mathbf{V}_c\cdot\mathbf{N}_s + a\mu_n\mathbf{N}\cdot\mathbf{k}_s - a\mu_t\mathbf{N}\cdot\mathbf{k}_s^{\perp} &< 0.5u_g \\ -0.5v_g < \mathbf{V}_c\cdot\mathbf{N}_s^{\perp} + a\mu_n\mathbf{N}\cdot\boldsymbol{\kappa}_s - a\mu_t\mathbf{N}\cdot\boldsymbol{\kappa}_s^{\perp} &< 0.5v_g \ , \end{aligned} \tag{3.47}$$

where

$$\mathbf{k}_s \equiv \hat{T}^{\mathrm{T}}\mathbf{N}_s \ , \qquad \boldsymbol{\kappa}_s \equiv \hat{T}^{\mathrm{T}}\mathbf{N}_s^{\perp} \ . \tag{3.48}$$

This can be written as

$$\begin{aligned}
\mathbf{V}_c\cdot\mathbf{N}_s + a\mu_n\mathbf{N}\cdot\mathbf{k}_s - 0.5u_g \;&<\; a\mu_t\mathbf{N}\cdot\mathbf{k}_s^{\perp} \;<\; \mathbf{V}_c\cdot\mathbf{N}_s + a\mu_n\mathbf{N}\cdot\mathbf{k}_s \\
\mathbf{V}_c\cdot\mathbf{N}_s^{\perp} + a\mu_n\mathbf{N}\cdot\boldsymbol{\kappa}_s - 0.5v_g \;&<\; a\mu_t\mathbf{N}\cdot\boldsymbol{\kappa}_s^{\perp} \;<\; \mathbf{V}_c\cdot\mathbf{N}_s^{\perp} + a\mu_n\mathbf{N}\cdot\boldsymbol{\kappa}_s + 0.5v_g\ .
\end{aligned} \tag{3.49}$$

This is equivalent to

$$\mu_t \in (\alpha_-,\alpha_+)\cap(\beta_-,\beta_+)\ , \tag{3.50}$$

where

$$\begin{aligned}
\alpha_\pm &\equiv \max_{\min}\left(\frac{\mathbf{V}_c\cdot\mathbf{N}_s + a\mu_n\mathbf{N}\cdot\mathbf{k}_s - 0.5u_g}{a\mathbf{N}\cdot\mathbf{k}_s^{\perp}}\ ,\ \frac{\mathbf{V}_c\cdot\mathbf{N}_s + a\mu_n\mathbf{N}\cdot\mathbf{k}_s}{a\mathbf{N}\cdot\mathbf{k}_s^{\perp}}\right) \\
\beta_\pm &\equiv \max_{\min}\left(\frac{\mathbf{V}_c\cdot\mathbf{N}_s^{\perp} + a\mu_n\mathbf{N}\cdot\boldsymbol{\kappa}_s - 0.5v_g}{a\mathbf{N}\cdot\boldsymbol{\kappa}_s^{\perp}}\ ,\ \frac{\mathbf{V}_c\cdot\mathbf{N}_s^{\perp} + a\mu_n\mathbf{N}\cdot\boldsymbol{\kappa}_s + 0.5v_g}{a\mathbf{N}\cdot\boldsymbol{\kappa}_s^{\perp}}\right)\ .
\end{aligned} \tag{3.51}$$

Define

$$\mu_t^{\pm} \equiv \min_{\max}(\alpha_\pm,\beta_\pm)\ . \tag{3.52}$$

If $\mu_t^- > \mu_t^+$, then there is no solution to these inequalities. Otherwise, the inequalities are satisfied for

$$\mu_t \in \left(\mu_t^-,\mu_t^+\right)\ . \tag{3.53}$$

This range of values can be restricted further, if one requires that

$$\mu = \sqrt{\mu_n^2+\mu_t^2} \le \mu_{\max}\ . \tag{3.54}$$

This restricts the locus of points to those within a certain distance from the domain of dependence of the point $(t+\delta t,\mathbf{x}_p)$.

It is now a straightforward calculation to find the pressure, density and velocity at the point $\mathbf{x}_w$, using the linear interpolants in the $(i,j)^{\text{th}}$ cell. We denote this state with the superscript W. The pressure at point $(t,\mathbf{x}_w)$ is given by

$$p^W = p + (\mathbf{x}_w - \mathbf{x}_c)\cdot\nabla p\ . \tag{3.55}$$

By substituting $\mathbf{x}_w$ from Eq. (3.37), one finds

$$\begin{aligned}
p^W &= p^G - a\left[\boldsymbol{\nu}\cdot\nabla p - \rho a\nabla\cdot\mathbf{u}\right]\delta t - (1-1/D)\Delta\mathbf{x}_p\cdot\nabla p \\
&\quad - \delta t\left[\mathbf{E}_\nu^{(1)} - (1-1/D)\left(\mathbf{u}+a\boldsymbol{\nu}\right)\right]\cdot\nabla p - \delta t^2\ \mathbf{E}_\nu^{(2)}\cdot\nabla p\ ,
\end{aligned} \tag{3.56}$$

where p^G is the pressure given by the conventional Godunov scheme in Eq. (3.24); *i.e.*,

$$p^G = p + \left[(\mathbf{x}_p - \mathbf{x}_c) - \delta t\mathbf{u}\right]\cdot\nabla p - \delta t\rho a^2\nabla\cdot\mathbf{u}\ . \tag{3.57}$$

All quantities are evaluated at the center of the cell, and the two vectors $\mathbf{E}_\nu^{(1)}$ and $\mathbf{E}_\nu^{(2)}$ are given by

$$\mathbf{E}_\nu^{(1)} \equiv \frac{1}{D}\left[(\boldsymbol{\nu}\cdot\Delta\mathbf{x}_p^\perp)\,(\nabla a)^\perp - \widetilde{(\nabla\mathbf{u})}\Delta\mathbf{x}_p\right] , \tag{3.58}$$

$$\mathbf{E}_\nu^{(2)} \equiv \frac{1}{D}\left[\widetilde{(\nabla\mathbf{u})}\,(\mathbf{u}+a\boldsymbol{\nu}) - (\boldsymbol{\nu}\cdot\mathbf{u}^\perp)\,(\nabla a)^\perp\right] . \tag{3.59}$$

Similarly, for the component of the velocity vector in the $\mathbf{n}$ direction, one can show that

$$\begin{aligned}\mathbf{u}^W\cdot\mathbf{n} &= \mathbf{u}^G\cdot\mathbf{n} + \left[\frac{1}{\rho}\mathbf{n}\cdot\nabla p - a\boldsymbol{\nu}\cdot(\nabla\mathbf{u})^{\mathrm{T}}\mathbf{n}\right] - (1-1/D)\Delta\mathbf{x}_p\cdot(\nabla\mathbf{u})^{\mathrm{T}}\mathbf{n} \\ &\quad - \delta t\,[\mathbf{E}_\nu^{(1)} - (1-1/D)\,(\mathbf{u}+a\boldsymbol{\nu})]\cdot(\nabla\mathbf{u})^{\mathrm{T}}\mathbf{n} - \delta t^2\;\mathbf{E}_\nu^{(2)}\cdot(\nabla\mathbf{u})^{\mathrm{T}}\mathbf{n} .\end{aligned} \tag{3.60}$$

By the definition of the Riemann Invariant Manifold,

$$\boldsymbol{\nu}\cdot\left[\nabla p + \rho a\,(\nabla\mathbf{u})^{\mathrm{T}}\mathbf{n}\right] \;=\; \mathbf{n}\cdot\nabla p + \rho a\nabla\cdot\mathbf{u} . \tag{3.61}$$

Therefore, Eq. (3.60) can be written

$$\begin{aligned}\mathbf{u}^W\cdot\mathbf{n} &= \mathbf{u}^G\cdot\mathbf{n} + \frac{1}{\rho}\left[\boldsymbol{\nu}\cdot\nabla p - \rho a\nabla\cdot\mathbf{u}\right]\delta t - (1-1/D)\Delta\mathbf{x}_p\cdot(\nabla\mathbf{u})^{\mathrm{T}}\mathbf{n} \\ &\quad - \delta t\,[\mathbf{E}_\nu^{(1)} - (1-1/D)\,(\mathbf{u}+a\boldsymbol{\nu})]\cdot(\nabla\mathbf{u})^{\mathrm{T}}\mathbf{n} - \delta t^2\;\mathbf{E}_\nu^{(2)}\cdot(\nabla\mathbf{u})^{\mathrm{T}}\mathbf{n} .\end{aligned} \tag{3.62}$$

It is seen from these equations that the leading order difference between the state given by the Godunov scheme and the state given by the Riemann Invariant Manifold is the term

$$\boldsymbol{\nu}\cdot\nabla p - \rho a\nabla\cdot\mathbf{u} , \tag{3.63}$$

for both the pressure and the velocity. The density is given by a similar equation,

$$\begin{aligned}\rho^W &= \rho^G - \left[a\boldsymbol{\nu}\cdot\nabla\rho - \rho\nabla\cdot\mathbf{u}\right]\delta t - (1-1/D)\Delta\mathbf{x}_p\cdot\nabla\rho \\ &\quad - \delta t\,[\mathbf{E}_\nu^{(1)} - (1-1/D)\,(\mathbf{u}+a\boldsymbol{\nu})]\cdot\nabla\rho - \delta t^2\;\mathbf{E}_\nu^{(2)}\cdot\nabla\rho .\end{aligned} \tag{3.64}$$

The state computed this way, *i.e.*, by tracing the Riemann Invariant Manifold R_n = const, serves as the left state for a 1-D characteristic problem. To find the right state, one needs to trace the R_{-n} = const manifold, which corresponds to the unit vector $-\mathbf{n}$. A locus of points $(t, \mathbf{x}_w)$ can be found, which are connected with the point $(t+\delta t, \mathbf{x}_p)$ by

$$\frac{dp}{dt} - \rho a\frac{du_n}{dt} \;=\; 0 . \tag{3.65}$$

These points may lie in the $(i,j)^{\text{th}}$ cell or the $(i+1,j)^{\text{th}}$ cell or both, depending on the local flow gradients. The solution to this 1-D characteristic problem will give the pressure, density and velocity component $\mathbf{u}\cdot\mathbf{n}$ at the point $(t+\delta t, \mathbf{x}_p)$. It is obvious that the velocity component $\mathbf{u}\cdot\mathbf{n}^{\perp}$ is also needed. There are two ways to find this.

One way is to examine the geometry of the Riemann Invariant Manifolds that correspond to the unit vectors $\pm\mathbf{n}^{\perp}$ and to set up another 1-D characteristic problem. The solution to this will give the velocity component required, along with a new value for the pressure and density. One can, then, take the average of the pressures and densities of the two 1-D problems.

There is a different way of calculating the velocity component $\mathbf{u}\cdot\mathbf{n}^{\perp}$, which is now described. The momentum equation is

$$\frac{\partial \mathbf{u}}{\partial t} + \mathbf{u}\cdot\nabla\mathbf{u} + \frac{1}{\rho}\nabla p \;=\; 0\,. \tag{3.66}$$

By taking the inner product of this equation with the constant unit vector $\mathbf{n}^{\perp}$, one finds

$$\frac{\partial}{\partial t}\left(\mathbf{u}\cdot\mathbf{n}^{\perp}\right) + \mathbf{u}\cdot(\nabla\mathbf{u})^{\mathrm{T}}\mathbf{n}^{\perp} + \frac{1}{\rho}\mathbf{n}^{\perp}\cdot\nabla p \;=\; 0\,. \tag{3.67}$$

It can be seen that along any path $\dot{\mathbf{x}}(t) = \mathbf{u} + a\boldsymbol{\nu}_u$ in spacetime such that

$$\boldsymbol{\nu}_u\cdot(\nabla\mathbf{u})^{\mathrm{T}}\mathbf{n}^{\perp} \;=\; \frac{1}{\rho a}\mathbf{n}^{\perp}\cdot\nabla p\,, \tag{3.68}$$

one has

$$\frac{\partial}{\partial t}\left(\mathbf{u}\cdot\mathbf{n}^{\perp}\right) + (\mathbf{u}+a\boldsymbol{\nu}_u)\cdot\nabla\left(\mathbf{u}\cdot\mathbf{n}^{\perp}\right) \;=\; 0\,, \tag{3.69}$$

which means that the velocity component $\mathbf{u}\cdot\mathbf{n}^{\perp}$ is constant along this path. In effect, a manifold is defined in a way completely analogous to the Riemann Invariant Manifolds. It is straightforward to show that Eq. (3.68) implies that

$$\boldsymbol{\nu}_u \;=\; \zeta_n\mathbf{N}_u + \zeta_t\mathbf{N}_u^{\perp}\,, \tag{3.70}$$

where

$$\mathbf{N}_u \;=\; \frac{(\nabla\mathbf{u})^{\mathrm{T}}\mathbf{n}^{\perp}}{\left|(\nabla\mathbf{u})^{\mathrm{T}}\mathbf{n}^{\perp}\right|}\,, \tag{3.71}$$

$$\zeta_n \;=\; \frac{1}{\rho a}\frac{\mathbf{n}^{\perp}\cdot\nabla p}{\left|(\nabla\mathbf{u})^{\mathrm{T}}\mathbf{n}^{\perp}\right|}\,. \tag{3.72}$$

The equations for this manifold are the same as those for the Riemann Invariant Manifolds with the following substitutions,

$$\mathbf{N} \rightarrow \mathbf{N}_u \ , \quad \mu_n \rightarrow \zeta_n \quad \text{and} \quad \mu_t \rightarrow \zeta_t \ . \tag{3.73}$$

One can find a locus of points in a given cell by tracing this manifold back in time, exactly the way the Riemann Invariant Manifolds were traced. It can be seen, then, that the velocity component $\mathbf{u}\cdot\mathbf{n}^{\perp}$ is given by

$$\begin{aligned} \mathbf{u}^{W}\cdot\mathbf{n}^{\perp} \ = \ & \mathbf{u}^{G}\cdot\mathbf{n}^{\perp} - (1-1/D_u)\Delta\mathbf{x}_p\cdot(\nabla\mathbf{u})^{\mathrm{T}}\mathbf{n}^{\perp} - \delta t^2\ \mathbf{E}^{(2)}_{\nu_u}\cdot(\nabla\mathbf{u})^{\mathrm{T}}\mathbf{n}^{\perp} \\ & - \delta t\left[\mathbf{E}^{(1)}_{\nu_u} - (1-1/D_u)\left(\mathbf{u}+a\boldsymbol{\nu}_u\right)\right]\cdot(\nabla\mathbf{u})^{\mathrm{T}}\mathbf{n}^{\perp} \ , \end{aligned} \tag{3.74}$$

where

$$D_u \ \equiv \ 1 + \delta t\left(\nabla\cdot\mathbf{u} + \boldsymbol{\nu}_u\cdot\nabla a\right) + \delta t^2\left[\det\left(\nabla\mathbf{u}\right) + \boldsymbol{\nu}_u\cdot\widehat{(\nabla\mathbf{u})}\nabla a\right] \ , \tag{3.75}$$

$$\mathbf{E}^{(1)}_{\nu_u} \ \equiv \ \frac{1}{D_u}\left[\left(\boldsymbol{\nu}_u\cdot\Delta\mathbf{x}_p^{\perp}\right)(\nabla a)^{\perp} - \widetilde{(\nabla\mathbf{u})}\Delta\mathbf{x}_p\right] \ , \tag{3.76}$$

$$\mathbf{E}^{(2)}_{\nu_u} \ \equiv \ \frac{1}{D_u}\left[\widetilde{(\nabla\mathbf{u})}\left(\mathbf{u}+a\boldsymbol{\nu}_u\right) - \left(\boldsymbol{\nu}_u\cdot\mathbf{u}^{\perp}\right)(\nabla a)^{\perp}\right] \ . \tag{3.77}$$

The theory of Riemann Invariant Manifolds has given us a way of finding a 1-D characteristic problem near the interface $(i+1/2, j)$. The solution of the 1-D problem gives us the state at $(t+\delta t, \mathbf{x}_p)$ and hence the numerical fluxes. In the procedure described, the unit vector $\mathbf{n}$ was arbitrary. Therefore, the derived equations give us a two-parameter family of schemes for computing the fluxes. One degree of freedom comes from $\mathbf{n}$ and the other from the freedom to choose μ_t, although the latter is restricted by relations like (3.53). This family of schemes is consistent with the multidimensional theory and provides a way for correcting the conventional Godunov scheme. The conventional scheme assumes $\mathbf{n} = \mathbf{N}_s$; *i.e.*, it sets up a 1-D problem in the grid direction. If this choice is made, then one is left with choosing μ_t in each case. The conventional scheme described here always takes the left state from the cell (i, j) and the right state from the cell $(i+1, j)$. The proposed, multidimensional scheme examines the geometry of the manifolds $R_n =$ const and $R_{-n} =$ const to determine the left and right states. It was seen in Eqs. (3.52) and (3.53) that $\mu_t^- < \mu_t^+$ must hold if the $(i,j)^{\text{th}}$ cell can be used to compute the left state. It is possible for both states to be taken from one cell, depending on the local flow gradients. A possible choice for μ_t, which works well in practice, is

$$\mu_t \ = \ (\mu_t^- + \mu_t^+)/2 \ . \tag{3.78}$$

So far, the tacit assumption of smooth, shock-free flow was made. The theory of Riemann Invariant Manifolds has been developed with the assumption that the flow gradients exist and are smooth. It is known that in gas-dynamical flows, discontinuities in the flow variables and their gradients may be present. The theory, nevertheless, can still be used for flows with such discontinuities. In the 1-D case, although the characteristics cannot propagate information across shocks, they can still be used on either side of shocks to determine the states that are related via the jump conditions. It is the generalization of the 1-D characteristic equations that leads to the concept of the Riemann problem. In the context of a Godunov scheme, discontinuities are assumed at every cell interface. In the smooth regions of the flow, these discontinuities are infinitesimally weak, and the characteristics are used to compute the numerical fluxes as shown in Fig. 3.2. To take care of the flow regions containing shocks, the characteristic problem is generalized to the Riemann problem.

In the multidimensional case the situation is similar. The Riemann Invariant Manifolds cannot propagate information through shocks or characteristic surfaces that contain derivative discontinuities. Nevertheless, they can be used on either side of these discontinuities to determine the states that are connected with the appropriate jump conditions. The easiest way of implementing this, although possibly not the most accurate, is to use the left and right states, determined by the Riemann Invariant Manifolds, as the initial condition for a 1-D Riemann problem. In this case, care must be taken so that the left and right states are not both taken from the unshocked region, because then, the information carried by the manifolds will not propagate through the approaching shock and will never reach the appropriate interface. This geometric picture also suggests the possibility of changing the unit vector $\mathbf{n}$ locally, so that it coincides with the unit normal of the discontinuity fronts. For example, consider a shock with unit normal $\mathbf{n}$, locally. The Riemann Invariant Manifolds $R_{\pm n} = \text{const}$ on either side of the shock can be used to determine the states that are related with the jump conditions.

This procedure is reminiscent of the attempts to fit shocks in flows when the method of characteristics is used. The analogy is not surprising, since the theory of Riemann Invariant Manifolds can be looked at as an extension of the method of characteristics to the general, multidimensional case.

It is also interesting to determine when the conventional MUSCL scheme, at

least the version used here as a reference point, will give the same results as the multidimensional scheme. It is seen from Equations (3.56), (3.62), (3.74) and (3.64) that the two schemes will coincide to *leading order*, if the left state can be taken from the left cell, the right state from the right cell and in addition,

$$\begin{aligned} \boldsymbol{\nu}\cdot\nabla p - \rho a \nabla\cdot\mathbf{u} &= 0\,, \\ a\boldsymbol{\nu}\cdot\nabla \rho - \rho \nabla\cdot\mathbf{u} &= 0\,, \end{aligned} \tag{3.79}$$

for both manifolds $R_{\pm n}$ = const. This cannot always be satisfied, but it now becomes clear why the conventional schemes give reasonable results in multidimensional flows. The terms in Eq. (3.79) can be taken to be very small and sometimes zero. This depends on the local flow conditions.

3.3 Conclusions

A new way of looking at multidimensional gas dynamics has been presented. Examining the local geometry of the Riemann Invariant Manifolds it is possible to develop effective, numerical methods for computing such flows. The theory allows one to develop numerical schemes that take into account the multidimensional character of these flows in a mathematically consistent way. This theory can be considered an extension of the method of characteristics to multidimensional flows. Although the theory was developed for smooth flows, it is possible to use the geometrical information of these manifolds to determine the appropriate 1-D problem that needs to be solved across a flow discontinuity.

There are many ways of implementing these ideas numerically. As an example, it was shown how a second-order Godunov scheme can be modified to give a conservative, multidimensional, shock-capturing scheme for two-dimensional flows.

CHAPTER 4
Numerical Applications

The new multidimensional Godunov scheme developed in the previous chapter, is used to compute three gas-dynamical flows on rectangular grids. The first case is the steady-state, regular shock reflection off a wall at low resolution. The second flow is a double Mach reflection of a planar-shock incident on an oblique surface. These two problems have been used extensively as test cases for a variety of numerical methods, and there are detailed comparisons of existing methods in the literature; *e.g.*, see Woodward and Colella (1984) and Colella (1990). The third flow is an example of an inviscid, shear layer bounded by reflecting walls. There is no roll-up of the layer, so in effect we compute the interaction of the generated waves with a slip surface. In all the calculations, a perfect gas is assumed, with constant, specific heat ratio equal to $\gamma = 1.4$.

4.1 Regular shock reflection

This case is a simple shock reflection, which has been used as a test case by many investigators. Colella (1990), among others, describes the initial and boundary conditions for this problem.

The computational domain is the rectangular domain $0 < x < 4$ and $0 < y < 1$. The lower boundary $y = 0$ is a reflecting wall, and at the right boundary $x = 4$, outflow conditions are imposed. The following inflow conditions are specified at the left boundary $x = 0$,

$$p = 1.0/1.4 \quad \rho = 1.0 \quad u = 2.9 \quad v = 0\,, \tag{4.1}$$

and at the top boundary $y = 1$, the following Dirichlet boundary condition is imposed:

$$p = 1.52819 \quad \rho = 1.69997 \quad u = 2.61934 \quad v = -0.50632\,. \tag{4.2}$$

The initial condition in the entire domain is that of the inflow condition.

The computation is carried out with a CFL number of 0.40 until a steady state is achieved. Pressure contours at time $t = 5$ are shown in Fig. 4.1. The pressure profile at the location $y = 0.525$ is shown in Fig. 4.2. Some oscillations can be seen in the postshock region. The present scheme employs no explicit, artificial dissipation as does the PPM scheme described by Colella and Woodward (1984). According to these authors this additional dissipation is needed to suppress oscillations behind shocks that don't move with respect to the grid.

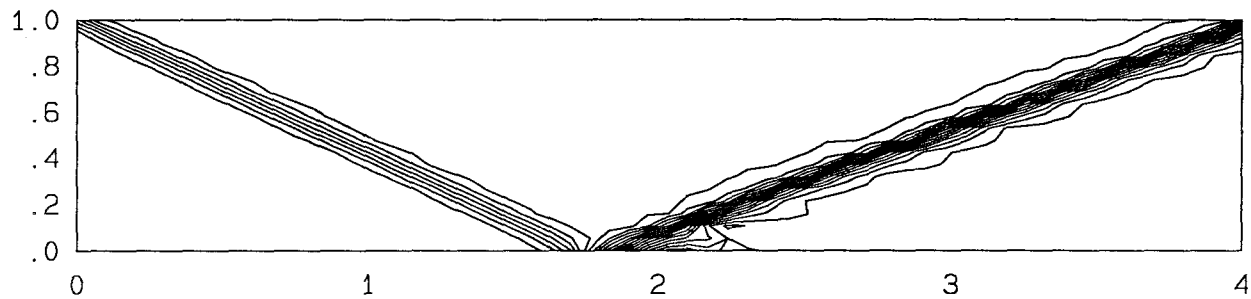

FIG.4.1 Regular shock reflection. Pressure contour levels at time $t = 5$. There are 30 contour levels in the range $0.5 < p < 3.5$. The resolution is 60×20 cells.

4.2 Double Mach reflection

This flow has been used by Woodward and Colella (1984) as a test problem for the comparison of existing numerical methods. The initial condition is that of a strong planar-shock incident on an oblique surface at a 30° angle. The shock Mach number is $M_s = 10$. The computational domain is the rectangular domain $0 < x < 4$ and $0 < y < 1$. The incident shock at time $t = 0$ is an oblique shock starting at the location $(x, y) = (1/6, 0)$ and forming a 60° angle with the positive x-axis. The lower boundary is a reflecting wall for $1/6 < x < 4$. At the small portion $0 < x < 1/6$ of the lower wall, a Dirichlet boundary condition is imposed, which corresponds to the initial post-shock flow. This artificial boundary condition ensures that the reflected shock is always attached to the point $(x, y) = (1/6, 0)$. The right boundary $x = 4$ is an outflow boundary, and the left boundary $x = 0$ is an inflow boundary with inflow conditions those of the initial post-shock flow. The

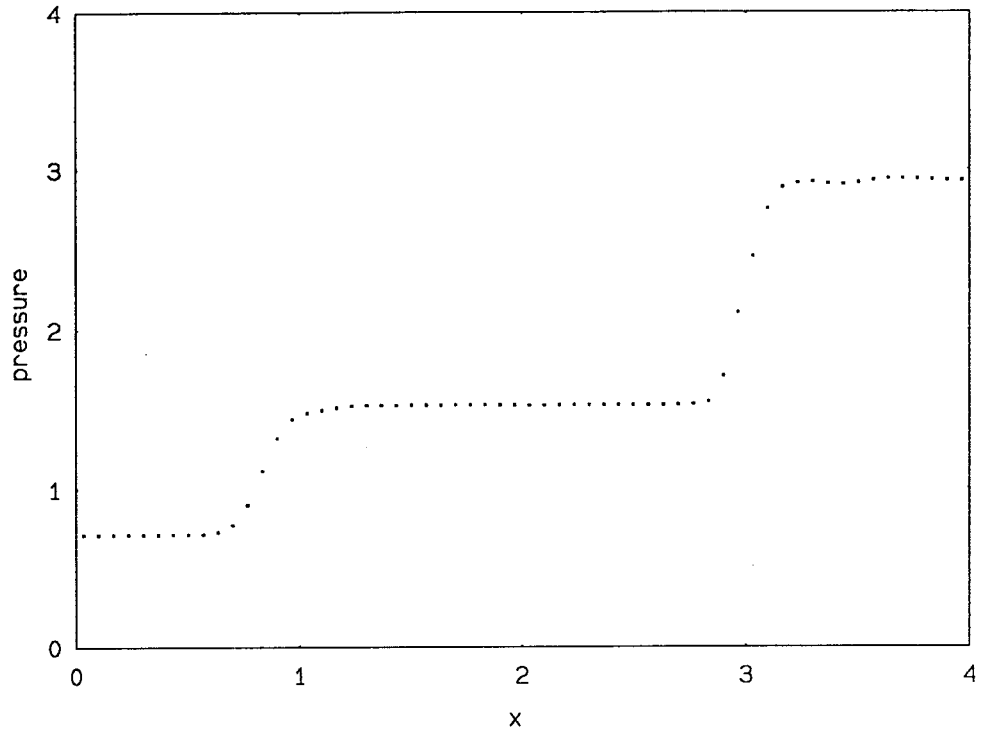

FIG.4.2 Regular shock reflection at time $t = 5$. Pressure profile along the line $y = 0.525$.

conditions at the top boundary $y = 1$ are specified to be those corresponding to the motion of the initial planar shock wave.

Results of this unsteady calculation are shown at time $t = 0.20$. The solution is shown in Figs. 4.3, for a low-resolution computation corresponding to a 120×30 grid. In Figs. 4.4, the higher-resolution computation is shown. This corresponds to a 240×60 grid.

4.3 Inviscid shear layer

The splitter plate is located at $y = 0$ and $x < 0$. The left boundary $x = 0$ is an inflow boundary with specified inflow conditions

$$\begin{aligned} p = 1.0 \quad \rho = 1.0 \quad M = 1.414\,, \qquad y < 0 \\ p = 1.5 \quad \rho = 2.0 \quad M = 1.633\,, \qquad y > 0\,, \end{aligned} \tag{4.3}$$

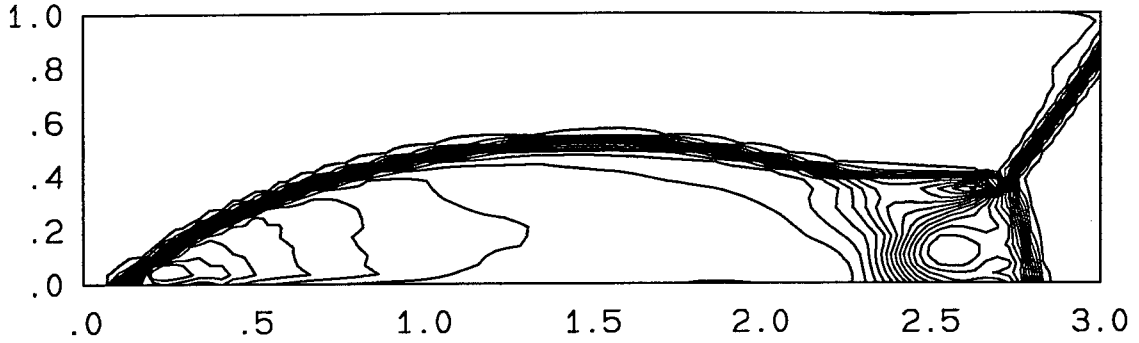

FIG.4.3a Double Mach reflection. Density contour levels at time $t = 0.20$. There are 30 contour levels in the range $1.7 < \rho < 18.5$. The resolution is 120×30 cells.

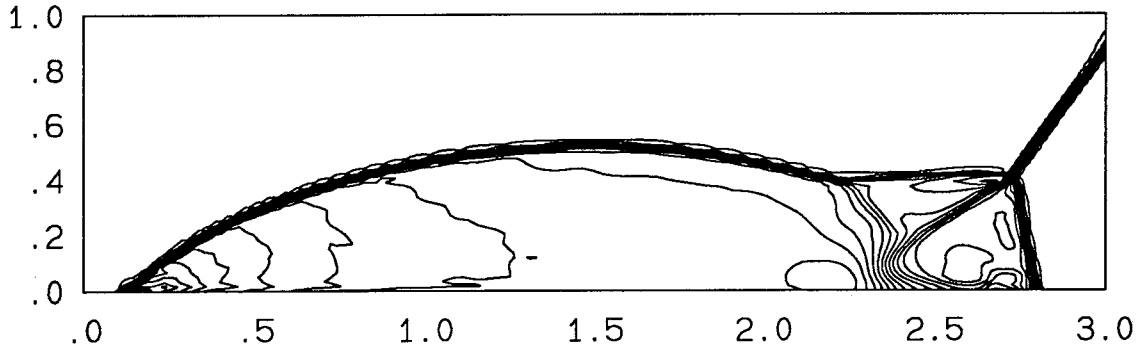

FIG.4.3b Double Mach reflection. Density contour levels at time $t = 0.20$. There are 30 contour levels in the range $1.73 < u < 21.0$. The resolution is 240×60 cells.

where p is the pressure, ρ is the density and M is the Mach number. These conditions are chosen so that the two free-stream velocities are equal, $U_1 = U_2 = 1.673$. Reflecting walls are assumed at the locations $y = \pm 1$, and the right boundary $x = 3$ is an outflow boundary. The initial condition is taken to be $p = 1$ everywhere and $\rho = 1$ for $y < 0$ and $\rho = 2$ for $y > 0$. The velocity is everywhere constant and equal to the two free-stream velocities. The computation was carried out until time $t = 5$, using a timestep that corresponds to a CFL number of 0.40. The results are shown in Figs. 4.5–4.9.

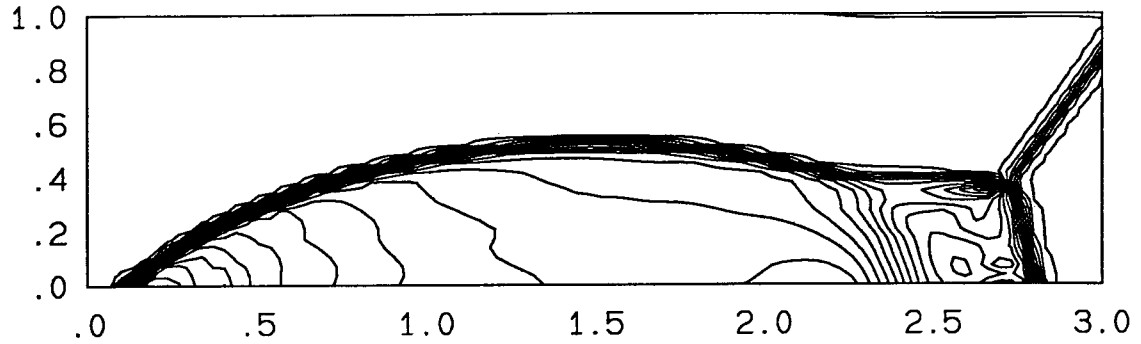

FIG.4.4a Double Mach reflection. Pressure contour levels at time $t = 0.20$. There are 30 contour levels in the range $2 < \rho < 450$. The resolution is 120×30 cells.

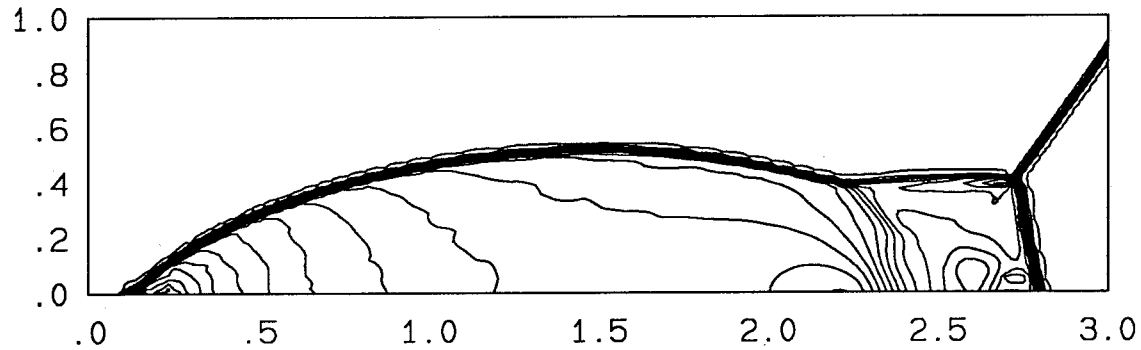

FIG.4.4b Double Mach reflection. Pressure contour levels at time $t = 0.20$. There are 30 contour levels in the range $2 < u < 480$. The resolution is 240×60 cells.

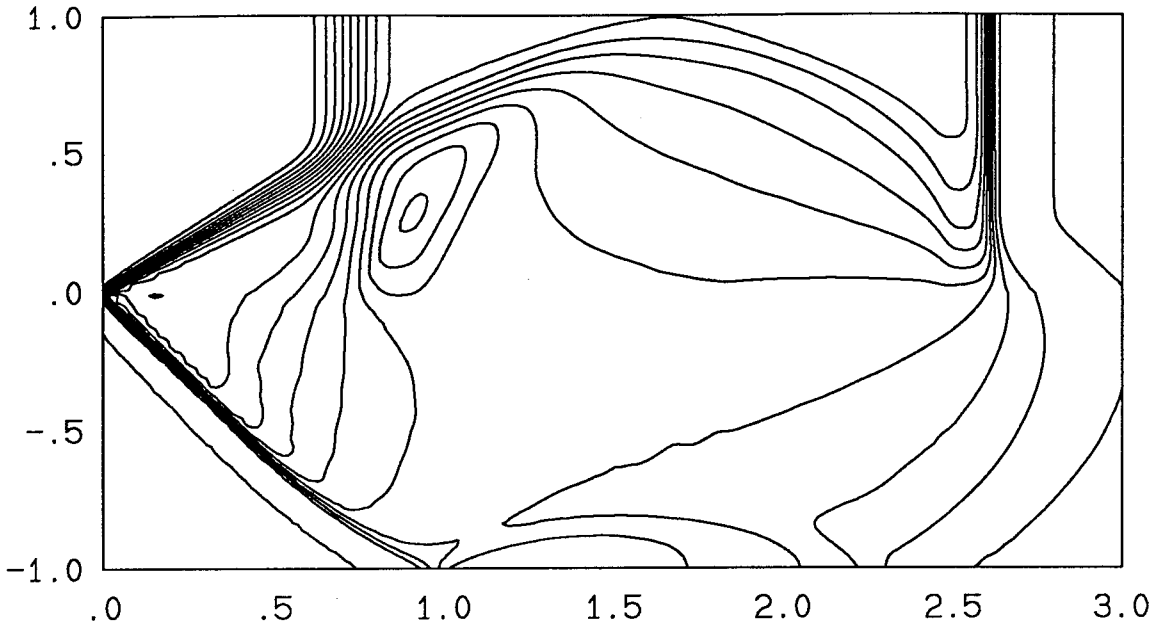

FIG.4.5a Inviscid shear layer. Pressure contour levels at time $t = 1.0$. There are 20 contour levels in the range $1.00 < p < 1.50$. The resolution is 200×100 cells.

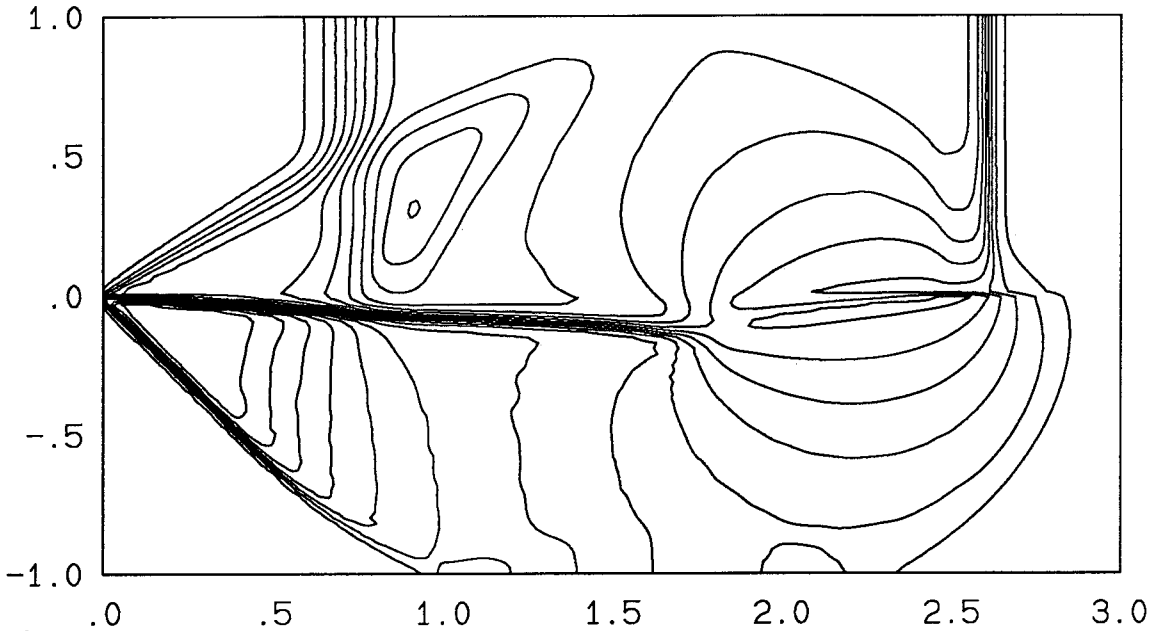

FIG.4.5b Inviscid shear layer. U-velocity contour levels at time $t = 1.0$. There are 20 contour levels in the range $1.54 < u < 1.87$. The resolution is 200×100 cells.

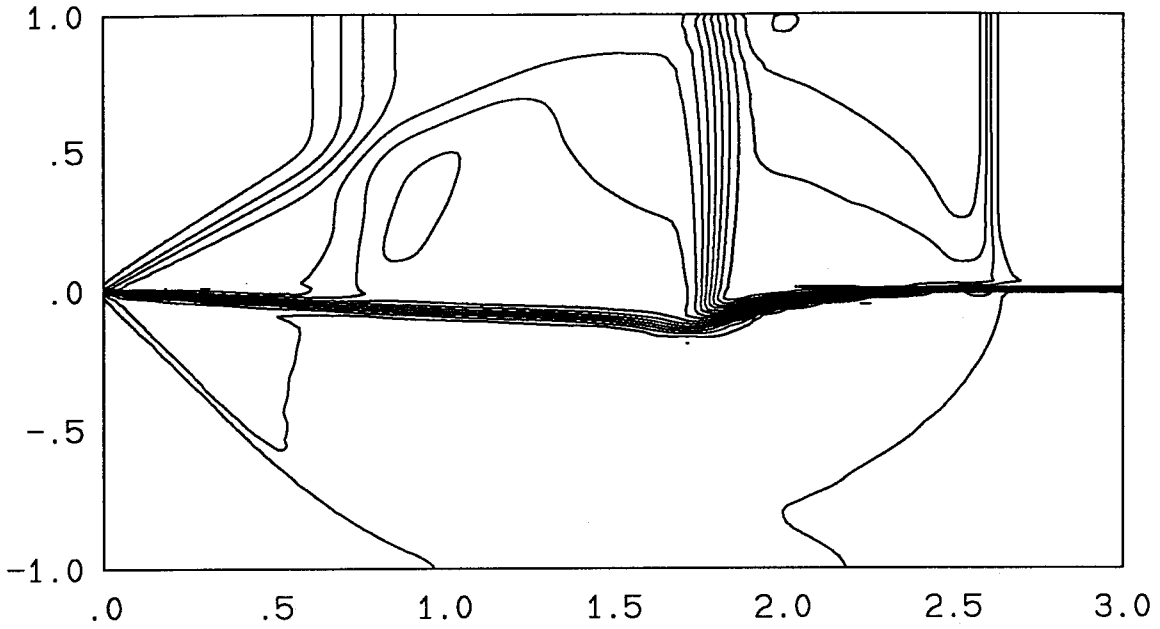

FIG.4.5c Inviscid shear layer. Density contour levels at time $t = 1.0$. There are 20 contour levels in the range $0.97 < \rho < 2.34$. The resolution is 200×100 cells.

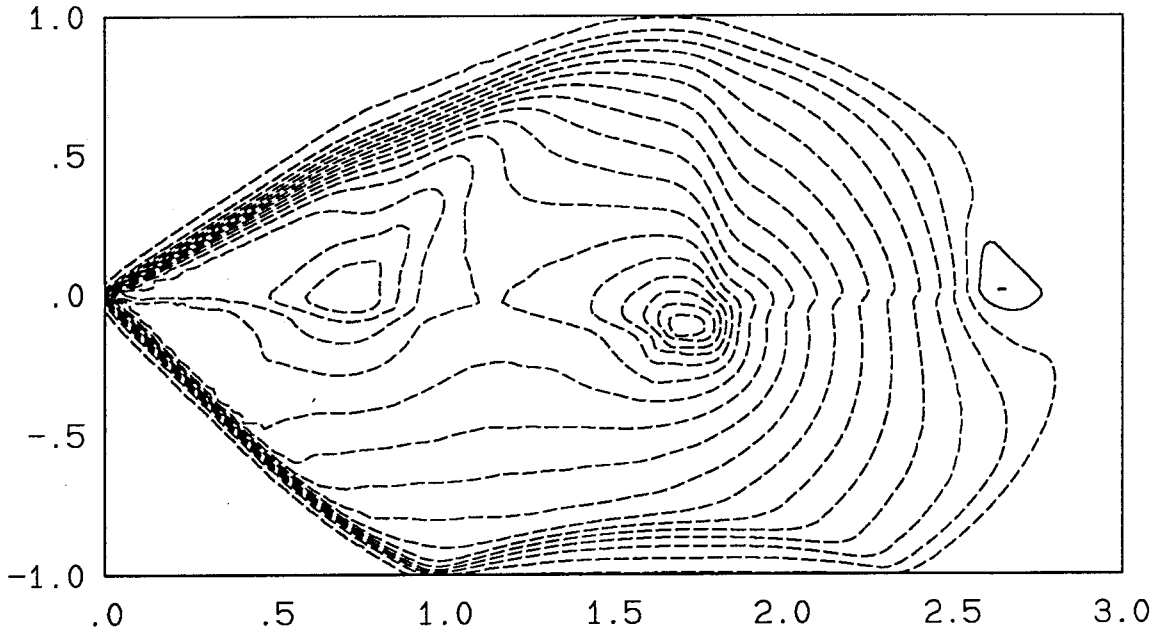

FIG.4.5d Inviscid shear layer. V-velocity contour levels at time $t = 1.0$. There are 20 contour levels in the range $-0.17 < v < 0.017$. The resolution is 200×100 cells.

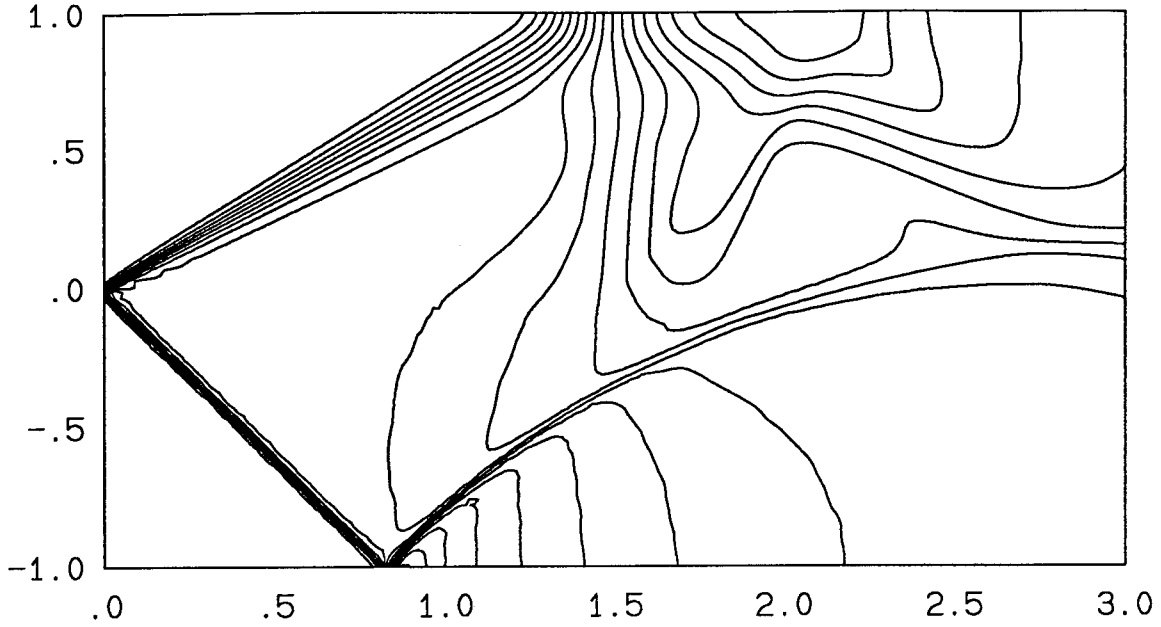

FIG.4.6a Inviscid shear layer. Pressure contour levels at time $t = 2.0$. There are 20 contour levels in the range $0.86 < p < 1.50$. The resolution is 200×100 cells.

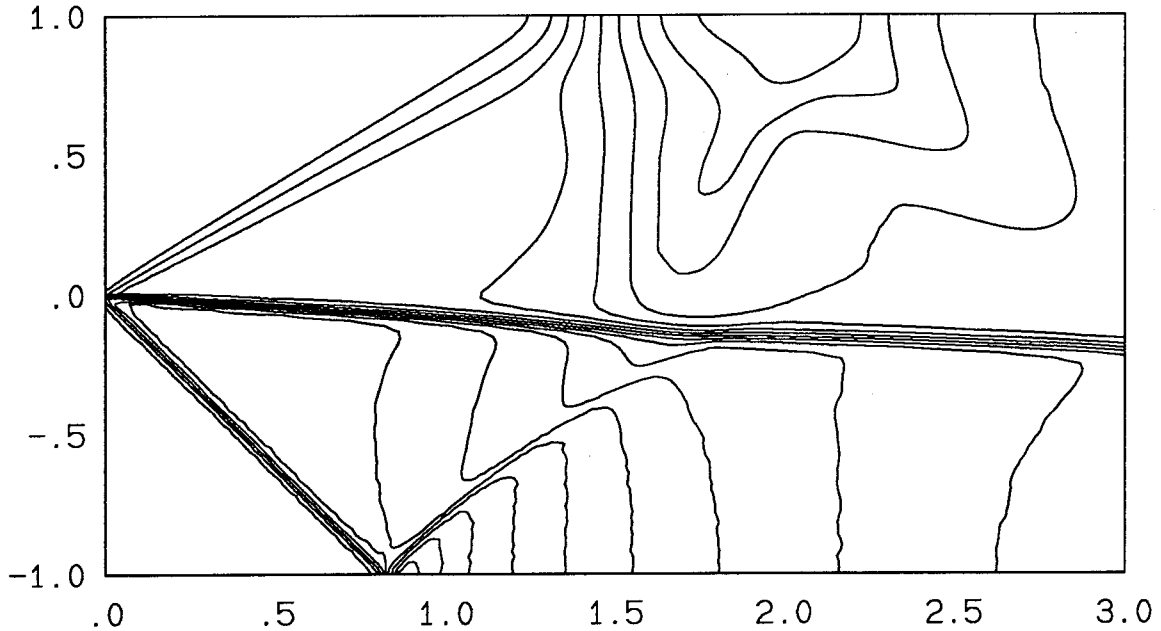

FIG.4.6b Inviscid shear layer. U-velocity contour levels at time $t = 2.0$. There are 20 contour levels in the range $1.42 < u < 1.93$. The resolution is 200×100 cells.

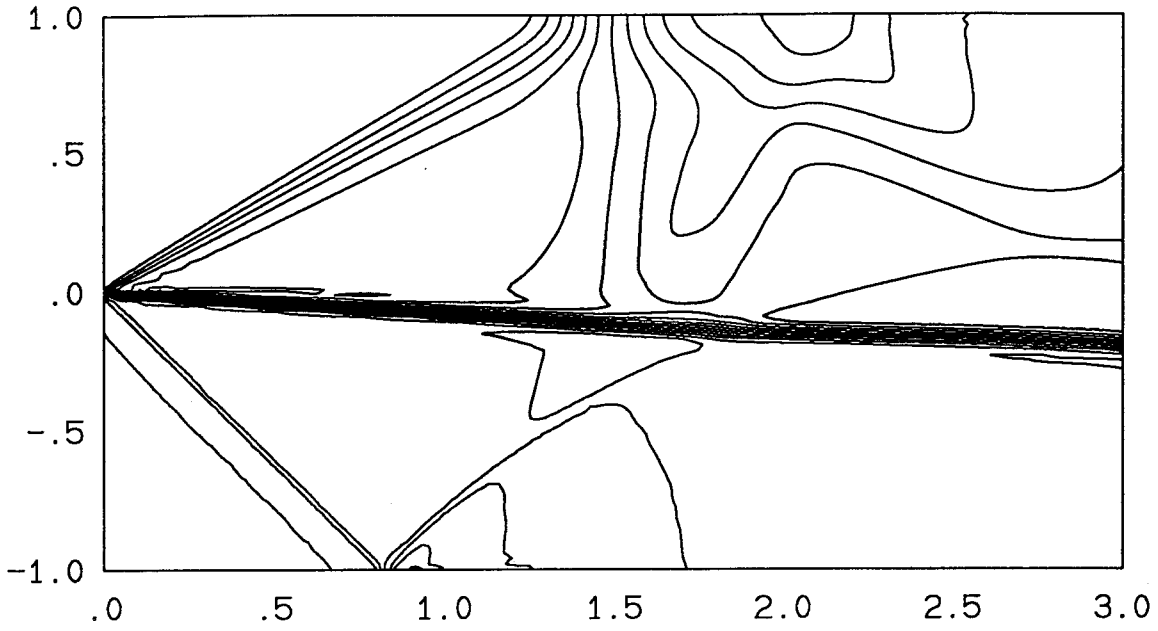

FIG.4.6c Inviscid shear layer. Density contour levels at time $t = 2.0$. There are 20 contour levels in the range $1.00 < \rho < 2.00$. The resolution is 200×100 cells.

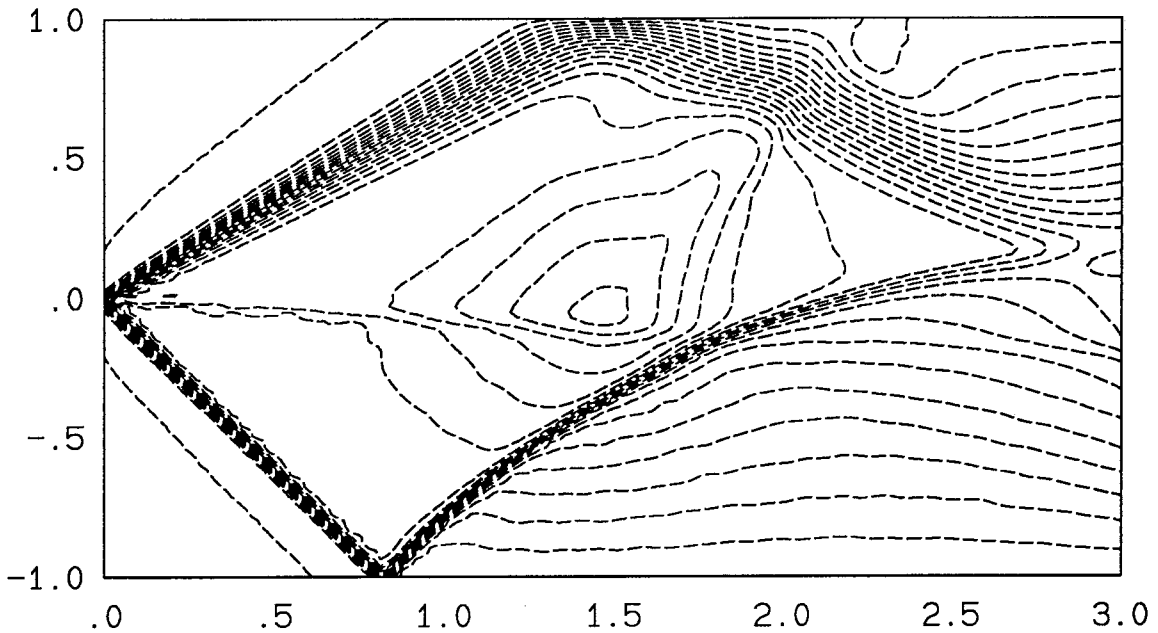

FIG.4.6d Inviscid shear layer. V-velocity contour levels at time $t = 2.0$. There are 20 contour levels in the range $-0.15 < v < 0.00$. The resolution is 200×100 cells.

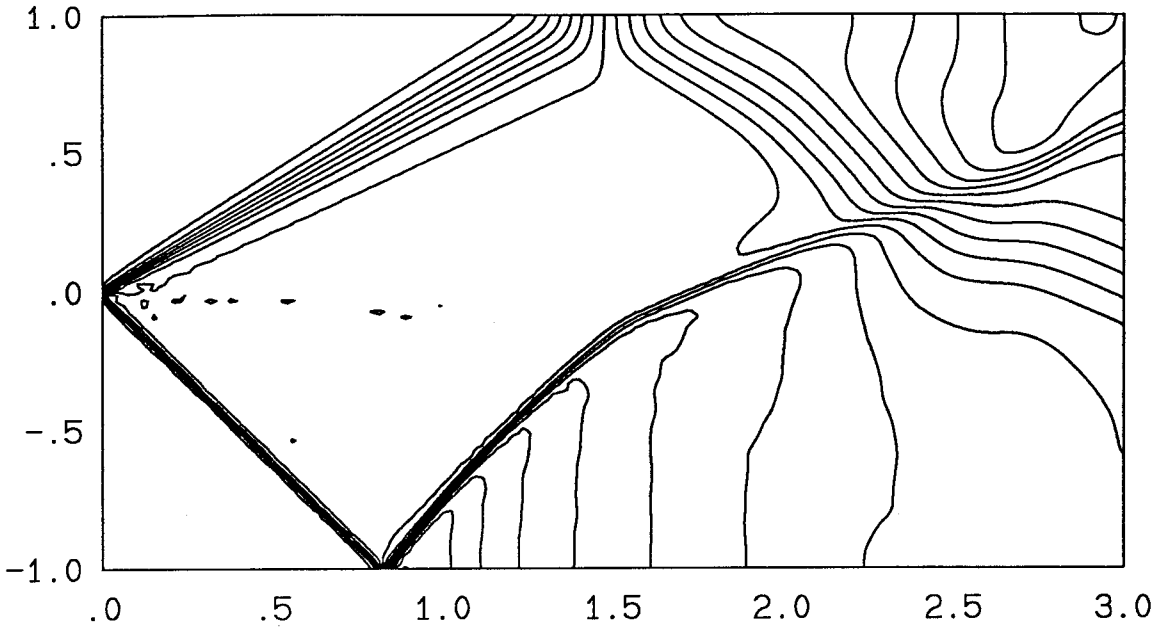

FIG.4.7a Inviscid shear layer. Pressure contour levels at time $t = 3.0$. There are 20 contour levels in the range $0.81 < p < 1.52$. The resolution is 200×100 cells.

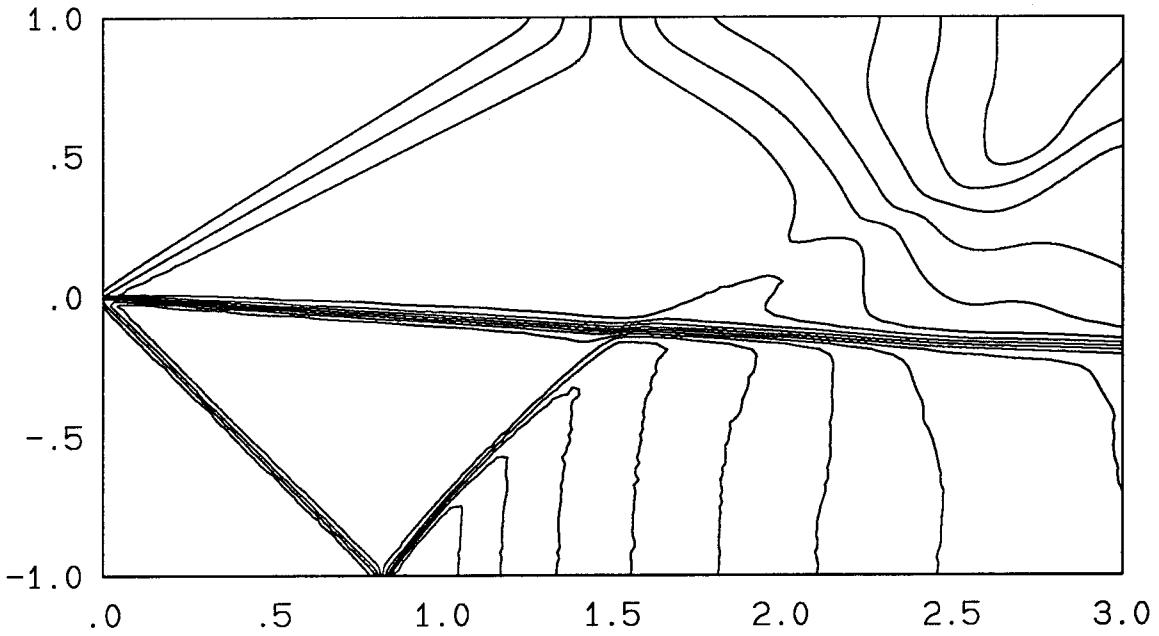

FIG.4.7b Inviscid shear layer. U-velocity contour levels at time $t = 3.0$. There are 20 contour levels in the range $1.38 < u < 1.96$. The resolution is 200×100 cells.

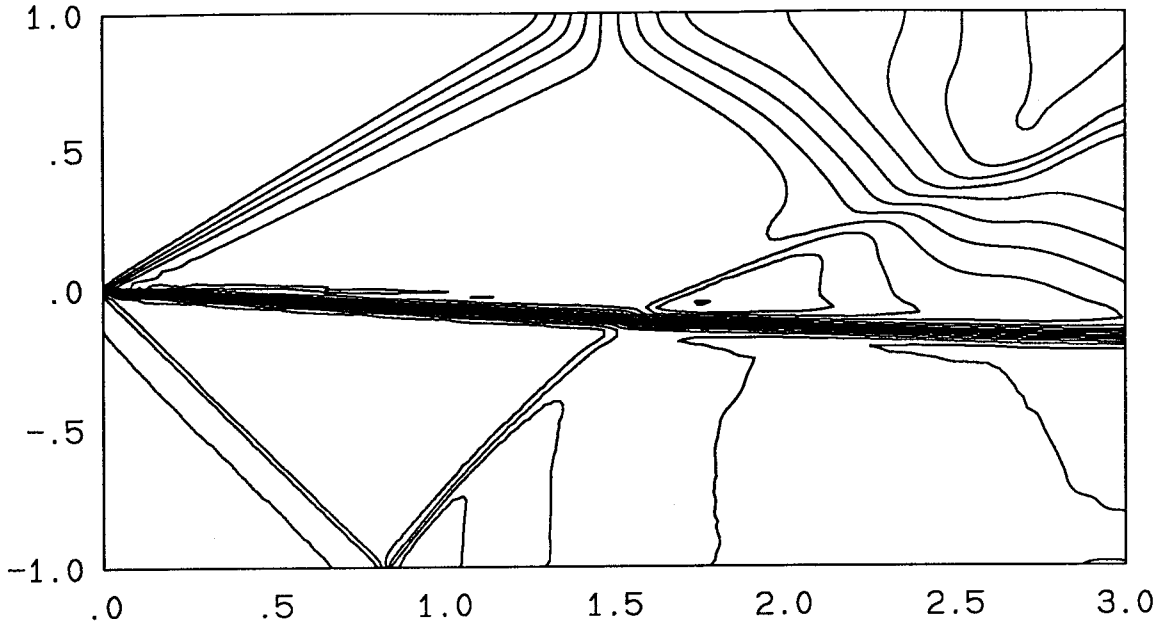

FIG.4.7c Inviscid shear layer. Density contour levels at time $t = 3.0$. There are 20 contour levels in the range $1.00 < \rho < 2.00$. The resolution is 200×100 cells.

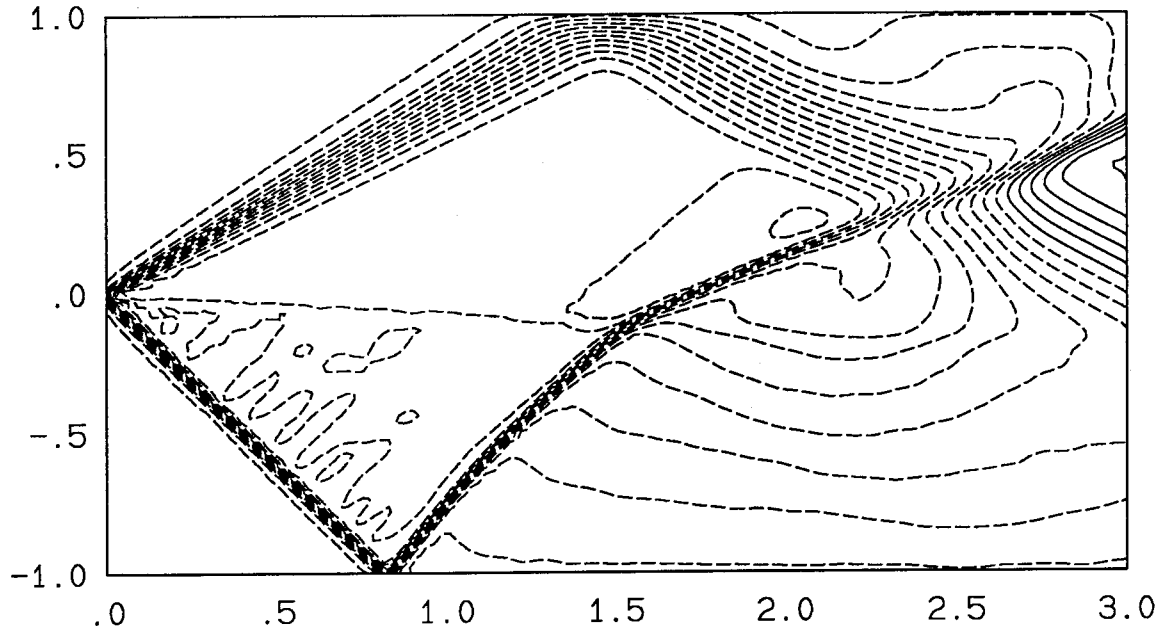

FIG.4.7d Inviscid shear layer. V-velocity contour levels at time $t = 3.0$. There are 20 contour levels in the range $-0.14 < v < 0.063$. The resolution is 200×100 cells.

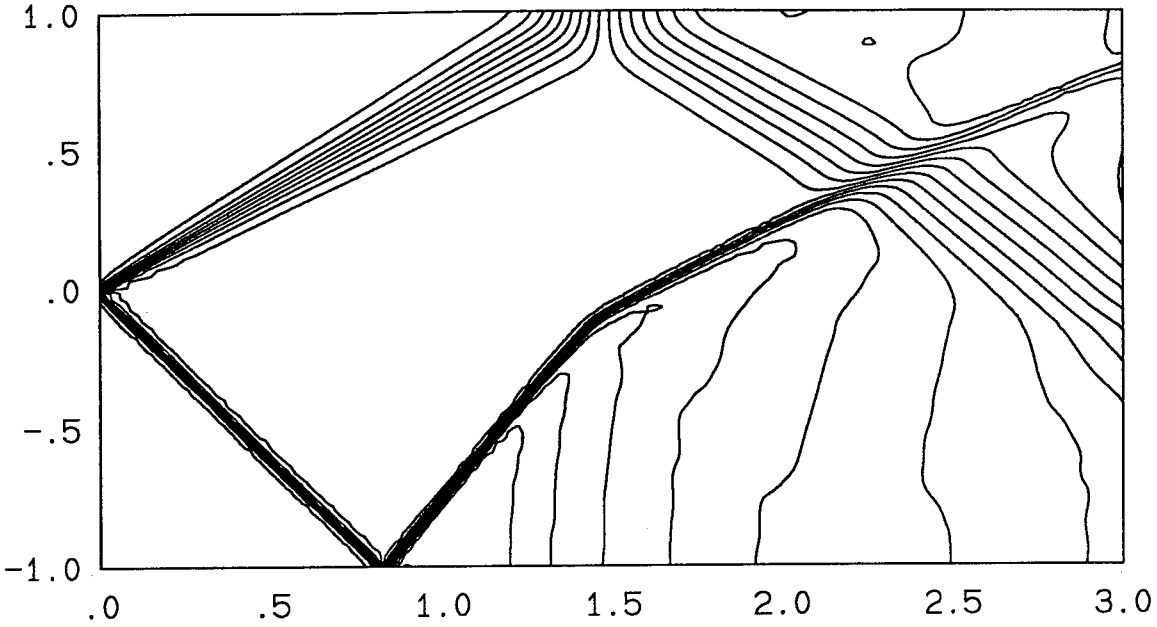

FIG.4.8a Inviscid shear layer. Pressure contour levels at time $t = 4.0$. There are 20 contour levels in the range $0.95 < p < 1.55$. The resolution is 200×100 cells.

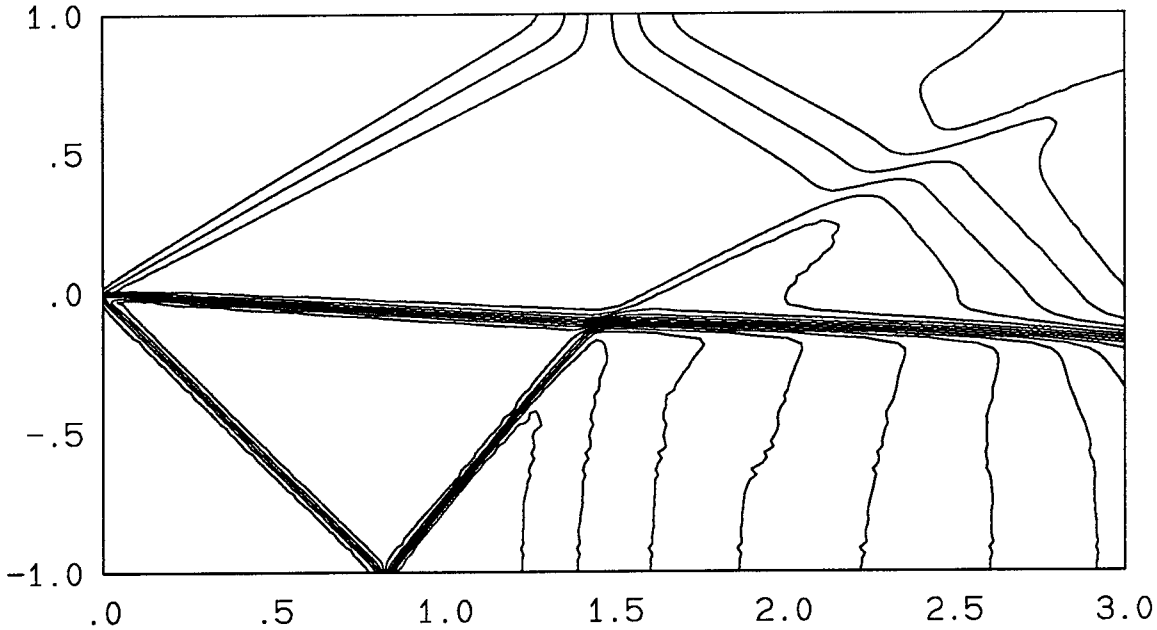

FIG.4.8b Inviscid shear layer. U-velocity contour levels at time $t = 4.0$. There are 20 contour levels in the range $1.38 < u < 1.87$. The resolution is 200×100 cells.

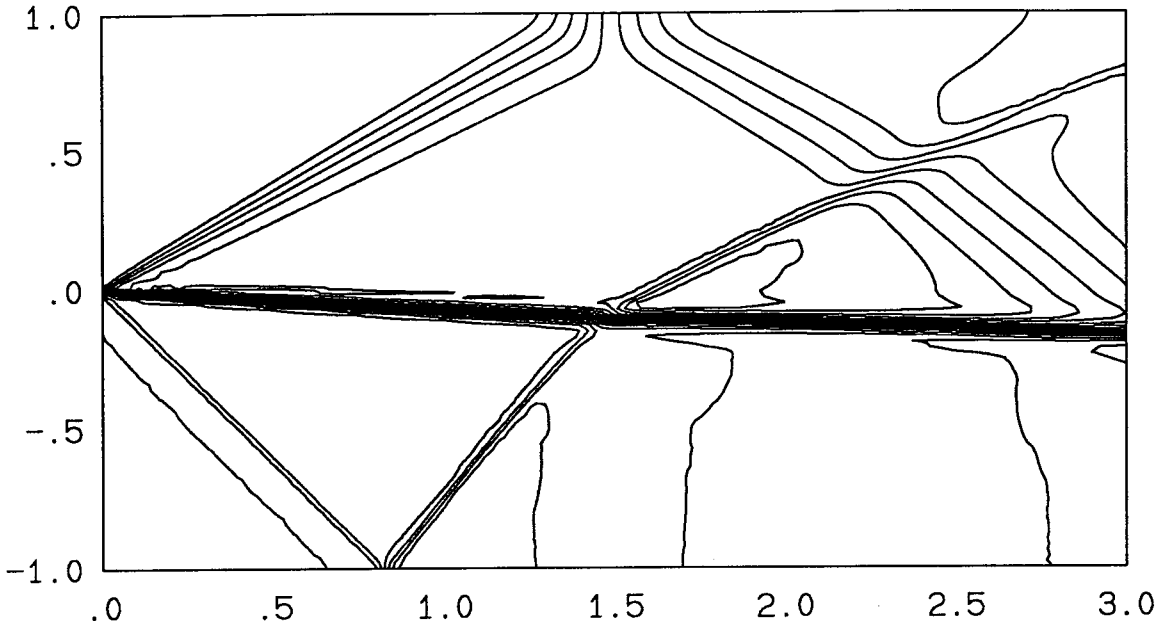

FIG.4.8c Inviscid shear layer. Density contour levels at time $t = 4.0$. There are 20 contour levels in the range $1.00 < \rho < 2.00$. The resolution is 200×100 cells.

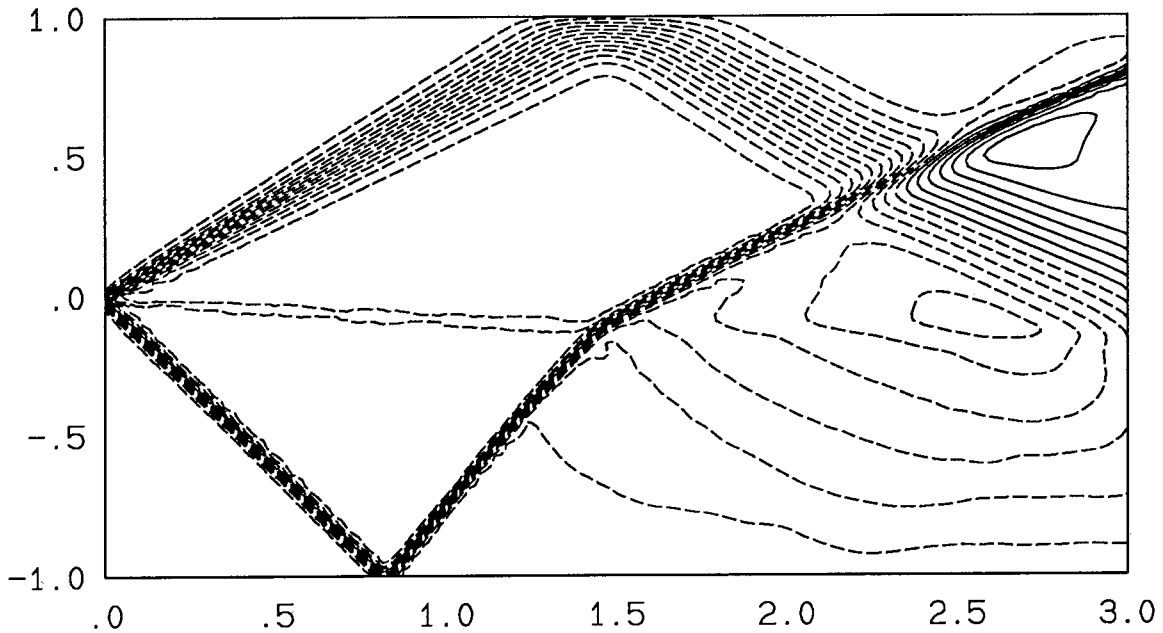

FIG.4.8d Inviscid shear layer. V-velocity contour levels at time $t = 4.0$. There are 20 contour levels in the range $-0.12 < v < 0.06$. The resolution is 200×100 cells.

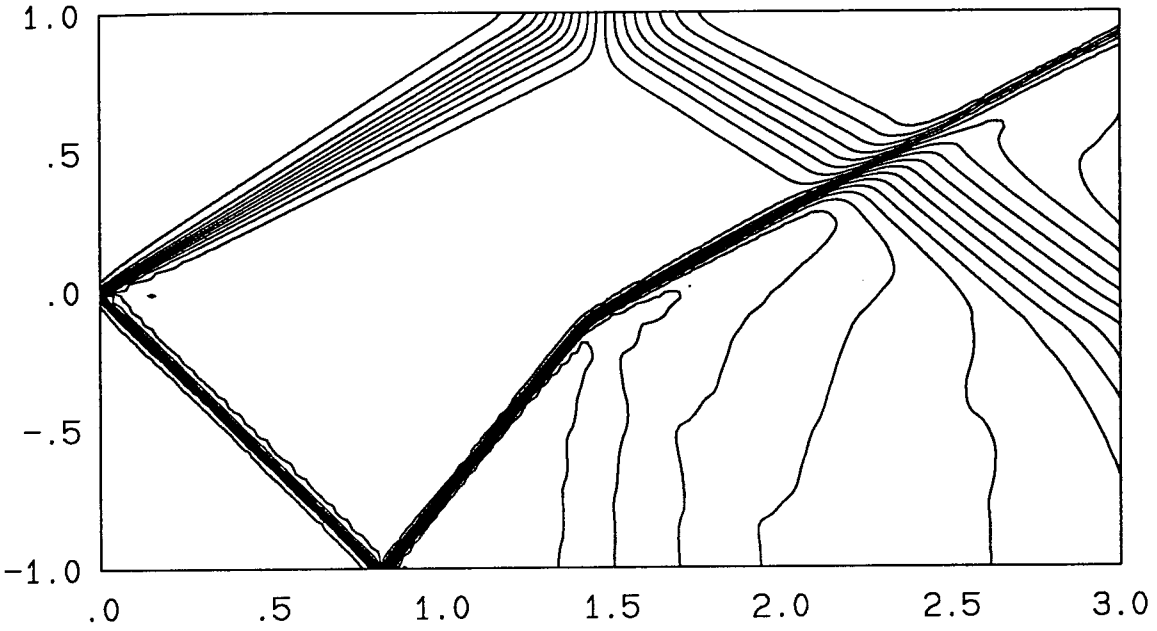

FIG.4.9a Inviscid shear layer. Pressure contour levels at time $t = 5.0$. There are 20 contour levels in the range $0.98 < p < 1.52$. The resolution is 200×100 cells.

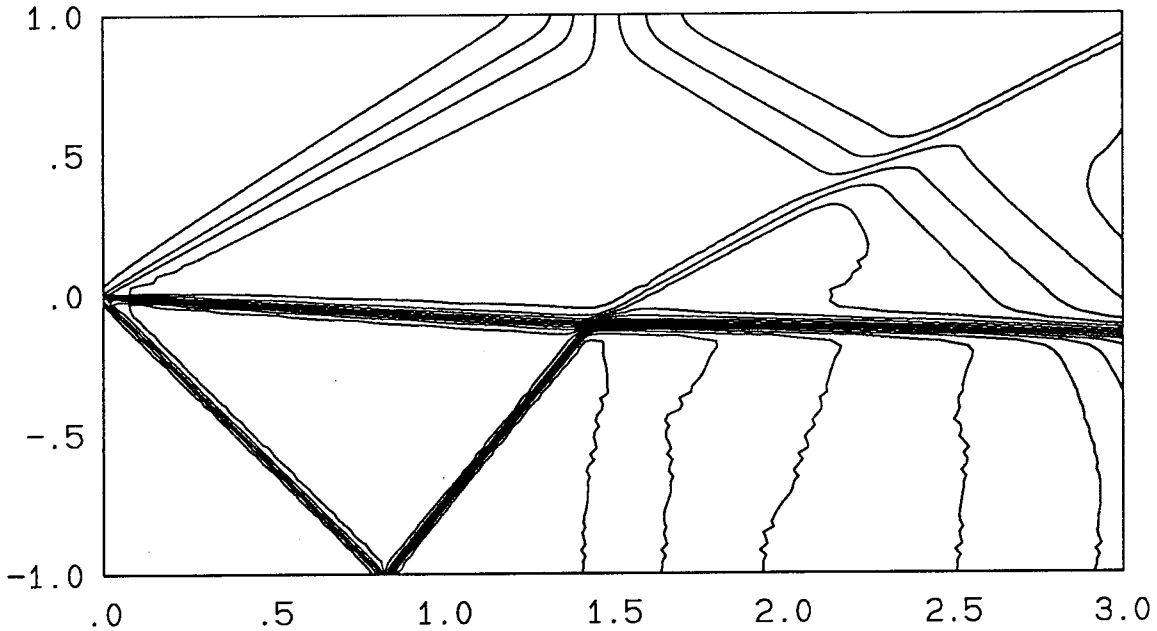

FIG.4.9b Inviscid shear layer. U-velocity contour levels at time $t = 5.0$. There are 20 contour levels in the range $1.38 < u < 1.85$. The resolution is 200×100 cells.

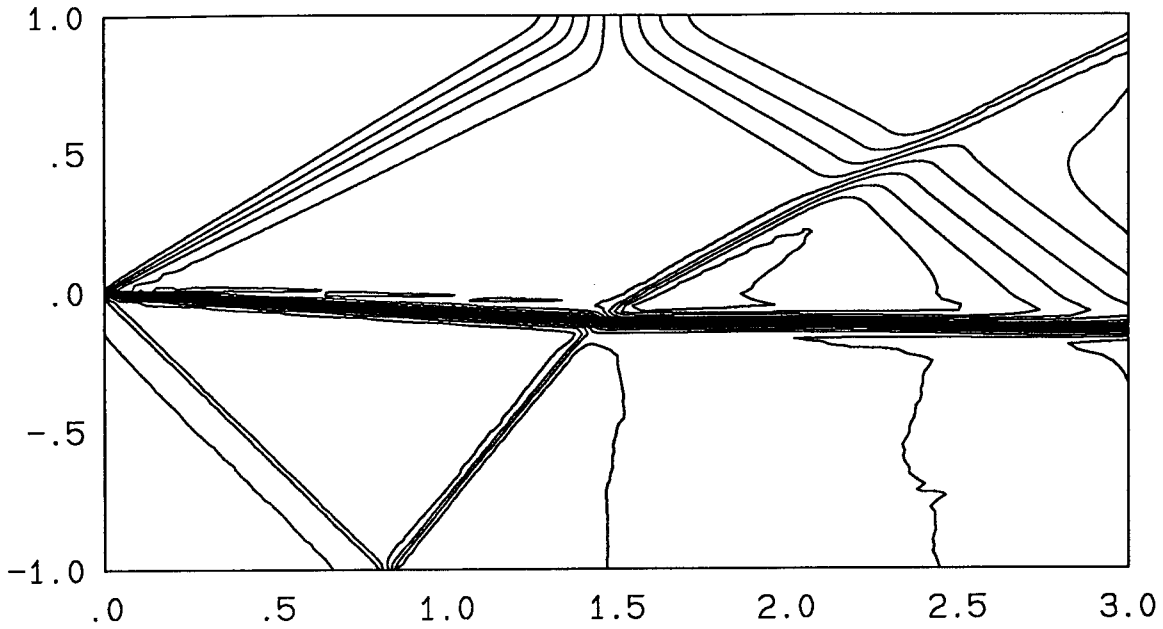

FIG.4.9c Inviscid shear layer. Density contour levels at time $t = 5.0$. There are 20 contour levels in the range $1.00 < \rho < 2.00$. The resolution is 200×100 cells.

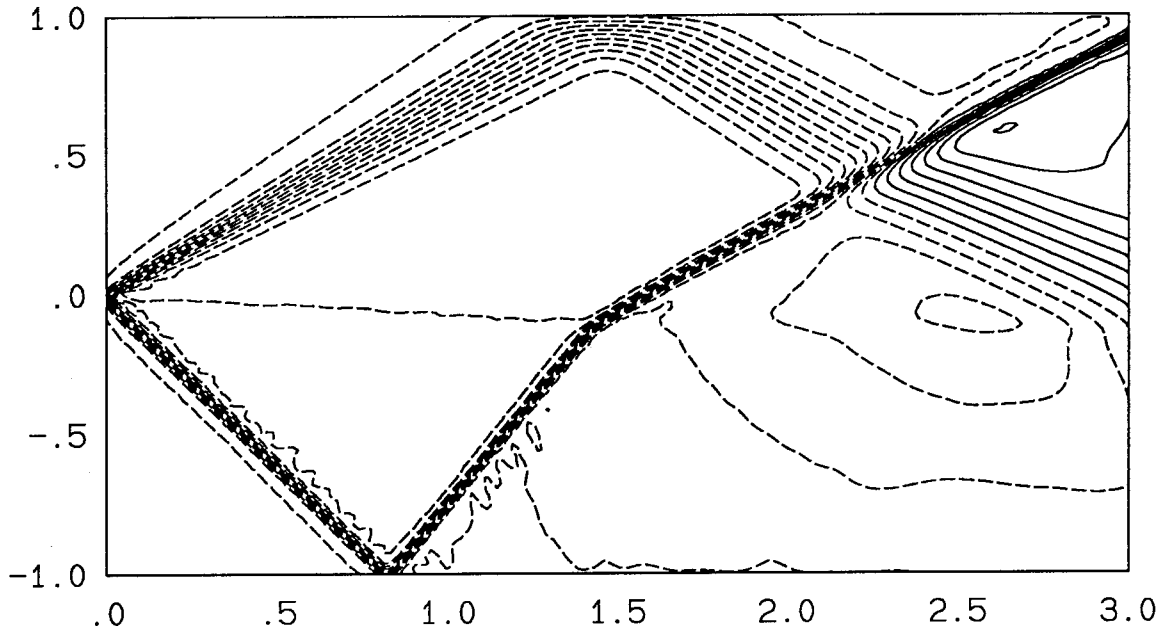

FIG.4.9d Inviscid shear layer. V-velocity contour levels at time $t = 5.0$. There are 20 contour levels in the range $-0.13 < v < 0.094$. The resolution is 200×100 cells.

References

BEN-ARTZI, M. [1989] "The Generalized Riemann Problem for Reactive Flows," *J. Comput. Phys.* **81**, 70–101.

BERGER, M.J. and OLIGER, J. [1984] "Adaptive Mesh Refinement for Hyperbolic Partial Differential Equations," *J. Comput. Phys.* **53**, 484–512.

BUTLER, D.S. [1960] "The Numerical Solution of Hyperbolic Systems of Partial Differential Equations in Three Independent Variables," *Proc. Roy. Soc. A*, **255**, 232–252.

COLELLA, P. and WOODWARD, P.R. [1984] "The Piecewise Parabolic Method (PPM) for Gas Dynamical Simulations," *J. Comput. Phys.* **54**, 174–201.

COLELLA, P. [1990] "Multidimensional Upwind Methods for Hyperbolic Conservation Laws," *J. Comput. Phys.* **87**, 171–200.

COURANT, R. and HILBERT, D. [1963] *Methods of Mathematical Physics, Vol.II* (Interscience, New York).

DECONINCK, H., HIRSCH, CH. and PEUTEMAN, J. [1986] "Characteristic Decomposition Methods for the Multidimensional Euler Equations," 10^{th} International Conference on Numerical Methods in Fluid Dynamics, Beijing, June 1986.

FICKETT, W. and DAVIS, W.C. [1979] *Detonation* (University of California Press, Berkeley).

FRIEDRICHS, K.O. [1954] "Symmetric Hyperbolic Linear Differential Equations," *Comm. Pure Appl. Math.* **7**, 345–392.

FRIEDRICHS, K.O. and LAX, P.D. [1965] "Boundary Value Problems for First Order Operators," *Comm. Pure Appl. Math.* **18**, 355–388.

GLIMM, J. [1965] "Solutions in the Large for Nonlinear Hyperbolic Systems of Equations," *Comm. Pure Appl. Math.* **18**, 697–715.

GODUNOV, S.K. [1959] "A Finite Difference Method for the Numerical Computation of Discontinuous Solutions of the Equations of Fluid Dynamics," *Mat. Sb.* **47**, 271–306.

HARTEN, A. [1983] "High Resolution Schemes for Hyperbolic Conservation Laws," *J. Comput. Phys.* **49**, 357–393.

HARTEN, A. [1984] "On a Class of High Resolution Total-Variation-Stable Finite-Difference Schemes," *SIAM Journal of Numerical Analysis* **21**, 1–23.

HARTEN, A., ENGQUIST, B., OSHER, S. and CHAKRAVARTHY, S.R. [1987] "Uniformly High Order Accurate Essentially Non-oscillatory Schemes, III," *J. Comput. Phys.* **71**, 231–303.

HIRSCH, CH. and LACOR, C. [1989] "Upwind Algorithms Based on a Diagonalization of the Multidimensional Euler Equations," AIAA Paper No. 89-1958, June 13–15 1989, Buffalo, New York.

KATO, T. [1975] "The Cauchy Problem for Quasi-Linear Symmetric Hyperbolic Systems," *Arch. Rational Mech. Analysis.* **58**, 181–205.

LAX, P.D. and WENDROFF, B. [1960] "Systems of Conservation Laws," *Commun. Pure Appl. Math.* **13**, 217–237.

LEE, H.I. and STEWART, D.S. [1990] "Calculation of linear detonation instability: one-dimensional instability of plane detonation," *J. Fluid Mech.* **216**, 103–132.

MACCORMACK, R.W. [1969] "The Effect of Viscosity in Hypervelocity Impact Cratering," AIAA Paper No. 69-354.

MONTAGNÉ, J.-L.,YEE, H.C. and VINOKUR, M. [1989] "Comparative Study of High-Resolution Shock-Capturing Schemes for a Real Gas," *AIAA J.* **27**(10), 1332–1346.

MORETTI, G. [1987] "Computation of Flows with Shocks," *Ann. Rev. Fluid Mech.* **19**, 313–337.

ROE, P.L. [1981] "Approximate Riemann Solvers, Parameter Vectors, and Difference Schemes," *J. Comput. Phys.* **43**, 357–372.

ROE, P.L. [1986] "Discrete Models for the Numerical Analysis of Time-Dependent Multidimensional Gas Dynamics," *J. Comput. Phys.* **63**, 458–476.

SMOLLER, J. [1983] *Shock Waves and Reaction-Diffusion Equations* (Springer-Verlag, New York).

SOD, G.A. [1978] "A Survey of Several Finite Difference Methods for Systems of Nonlinear Hyperbolic Conservation Laws," *J. Comput. Phys.* **27**, 1–31.

STEGER, J.L. and WARMING, R.F. [1981] "Splitting of the Inviscid Gasdynamic Equations with Application to Finite-Difference Methods," *J. Comput. Phys.* **40**, 263–293.

STRANG, G. [1968] "On the Construction and Comparison of Difference Schemes," *SIAM Journal of Numerical Analysis* **5**, 506–517.

VAN LEER, B. [1979] "Towards the Ultimate Conservative Difference Scheme. V. A Second-Order Sequel to Godunov's Method," *J. Comput. Phys.* **32**, 101–136.

VAN LEER, B. [1982] "Flux-Vector Splitting for the Euler Equations," *Lect. Notes Phys.* **170**, 507–512.

VAN LEER, B. [1984] "On the Relation Between the Upwind-Differencing Schemes of Godunov, Engquist-Osher and Roe," *SIAM J. Sci. Stat. Comput.* **5**(1), 1–20.

WOODWARD, P.R. and COLELLA, P. [1984] "The Numerical Simulation of Two-Dimensional Fluid Flow with Strong Shocks," *J. Comput. Phys.* **54**, 115–173.